MUHAMMAD BIN HASSAN

Magnetostratigraphic Analysis of Ferromanganese (Fe-Mn) Deposits

São Paulo

2023

MUHAMMAD BIN HASSAN

Magnetostratigraphic Analysis of Ferromanganese (Fe-Mn) Deposits

(Corrected Version)

A thesis submitted to the Instituto Oceanográfico da Universidade de São Paulo, as part of the requirements for obtaining the title of Doctor of Science, Oceanography Program, focus area of Geological Oceanography.

Advisor: Prof. Dr. Luigi Jovane

São Paulo

2023

HASSAN, Muhammad Bin. **Magnetostratigraphic Analysis of Ferromanganese (Fe-Mn) Deposits.** Thesis (Doctorate) presented to the Instituto Oceanográfico da Universidade de São Paulo to obtain the title of Doctor of Science, Oceanography Program, focus area of Geological Oceanography.

Approved on: ___/___/_____

Examination Committee

Prof. Dr. _____ Institution_____

President Signature_____

Prof. Dr. _____ Institution _____

Grade_____ Signature _____

Prof. Dr. _____ Institution _____

Grade_____ Signature _____

Prof. Dr. _____ Institution _____

Grade_____ Signature _____

ACKNOWLEDGEMENTS

My advisor, Prof. Luigi Jovane, for accepting me as his PhD student and for his continuous moral, scientific and economic support. His encouragement and support during the Covid-19 pandemic crisis was essential to continue this research.

To my host advisor Prof. Andrea Koschinsky for accepting me as a visiting research fellow for a year at the Geochemistry lab of the Department of Physics and Environmental Sciences, Jacobs University (now called Constructor University), in Bremen Germany. Her detailed guidance and support helped me to perform this research in a scientific way.

To all colleagues and friends at the Instituto Oceanográfico da Universidade de São Paulo and at the Department of Physics and Environmental Sciences, Jacobs University for helping me learn novel techniques essential for this research, for joining my stressful moments and for having a lot of fun together.

To the labs and related staff at the University of São Paulo, Jacobs University Bremen, Geological Survey of Germany, and Charles University in Prague, where I performed different lab analyses.

To the collaborators and co-authors who helped me develop this scientific project and related scientific papers.

To my parents and siblings for their continuous support and encouragement to develop this project during my stay far away from home.

This study was financed in part by the Coordenação de Aperfeiçoamento de Pessoal de Nível Superior - Brasil (CAPES) - Finance Code 001. However, the São Paulo Research Foundation (FAPESP) funded a major part of the research under project# 2017/04821-0 and 2021/06941-8.

As you start to walk out on the
way, the way appears.

RUMI

RESUMO

HASSAN, Muhammad Bin. **Análise Magnetoestratigráfica de Depósitos de Ferromanganês (Fe-Mn)**. 2023. 154 f. Tese (Doutorado) – Instituto Oceanográfico, Universidade de São Paulo, São Paulo, 2023.

Os depósitos de ferromanganês (FeMn) são oxihidróxidos de ferro e óxidos de manganês que se precipitam no fundo do mar ao longo de milhões de anos, em uma taxa de crescimento muito lenta. Suas variações químicas, mineralógicas e texturais refletem as condições paleoambientais sob as quais se formaram. Essa pesquisa foi desenvolvida para realizar estudos magnéticos em depósitos de FeMn coletados da elevação do Rio Grande (RGR) no sudoeste do Oceano Atlântico, *Tropic Seamount (TS)* no nordeste do Oceano Atlântico e no Oceano Pacífico. O estudo magnético, microscópico e geoquímico da amostra de nódulo de ferromanganês JC120-104B coletada na zona Clarion-Clipperton (CCZ) indica a presença de magnetita biogênica (magnetofósseis). O aumento das propriedades magnéticas é coerente com o aumento do teor de Mn, que está relacionado às condições favoráveis para a precipitação de Mn, bem como à biomineralização da magnetita na zona de transição óxica-subóxica. As crostas de FeMn se desenvolvem nas montanhas submarinas e ao redor delas, sendo uma fonte de metais essenciais e elementos de terras raras. A ocorrência amorfa (não cristalina) de oxi-hidróxidos de Fe e a ausência de óxidos de Fe nas camadas recentes (hidrogenéticas/não fosfatizadas/inalteradas) das crostas de FeMn, impedem o desenvolvimento de uma magnetização remanente primária. Embora o estudo magnético combinado com a investigação geoquímica seja essencial para entender as mudanças paleoambientais, é difícil obter um modelo magnetostratigráfico robusto para as crostas de FeMn estudadas, devido à ausência e a perda de magnetização primária. Como os nódulos e as crostas de FeMn do Oceano Pacífico contêm magnetita biogênica, produzida por bactérias magnetotáticas (MTB) como portadora de remanência primária, foi realizado um estudo magnético em células quantificadas produzidas por espécies bacterianas distintas. As propriedades magnéticas da magnetita biogênica quantificada, dependem da quantidade de células MTB e não da espécie bacteriana ou do tipo de célula (lisada ou inteira). Este estudo também estima o conteúdo de carbono das células MTB e discute a sua relação com o ciclo do carbono global. Para entender a relação entre a deposição de Fe e Mn, a magnetita biogênica produzida por MTB e as condições ambientais, também foi realizado um estudo em um poço do IODP da Grande Barreira de Corais (GBR), na Austrália. Os dados magnéticos mineralógicos e geoquímicos da Expedição 325 do IODP - poço M0058A, revelam a história de deposição da margem da GBR durante o intervalo de MIS 7 a 5 e MIS 1. Nesse caso, a

deposição de Fe e Mn em sedimentos mistos de carbonato siliciclástico está relacionada à entrada de terrígenos, enquanto a presença de magnetita biogênica está relacionada às condições climáticas áridas. Os períodos áridos no nordeste da Austrália foram estabelecidos após a transição glacial/interglacial e no Holoceno médio, favorecendo a deposição de poeira e promovendo a produtividade primária.

A ocorrência de Fe e Mn em ambientes marinhos distintos corresponde a diferentes implicações magnéticas. A presença de magnetita biogênica em nódulos e crostas de FeMn está ligada às condições de oxigenação, enquanto a magnetita biogênica em sedimentos mistos de carbonato siliciclástico está associada ao aumento da produtividade primária, que é reforçada por condições climáticas áridas.

Palavras-chave: Elevação do Rio Grande. Monte Submarino Trópico. Zona Clarion Clipperton. Depósitos de ferromanganês. Magnetismo de rocha. Paleomagentismo. Magnetofósseis. Sequestro de carbono.

ABSTRACT

HASSAN, Muhammad Bin. **Magnetostratigraphic Analysis of Ferromanganese (Fe-Mn) Deposits.** 2023. 154 f. Thesis (Doctorate) – Instituto Oceanográfico, Universidade de São Paulo, São Paulo, 2023.

Ferromanganese (FeMn) deposits are iron oxyhydroxides and manganese oxides which precipitate on the seafloor over millions of years at a very slow growth rate. Their chemical, mineralogical, and textural variations reflect the paleoenvironmental conditions under which they form. This research was developed to conduct magnetic studies on Fe-Mn deposits recovered from the Rio Grande Rise (RGR) in the southwestern Atlantic Ocean, Tropic Seamount (TS) in the northeastern Atlantic Ocean and the Pacific Ocean. Magnetic, microscopic, and geochemical study of ferromanganese nodule sample JC120-104B collected from Clarion-Clipperton zone (CCZ) indicates the presence of biogenic magnetite (magnetofossils). The nodule sample shows distinctive alternating Mn and Fe-rich layers, the increase in magnetic properties is consistent with the increase in Mn content, which is related to favourable conditions for Mn precipitation as well as magnetite biomineralization in the oxic-suboxic transition zone. FeMn crusts develop on and around seamounts and are a source of essential metals and rare earth elements. The amorphous (non-crystalline) occurrence of Fe oxyhydroxides and the absence of Fe oxides in the recent fresh (hydrogenetic/non-phosphatized/unaltered) layers of FeMn crusts prevent developing a primary remanent magnetization. While magnetic study combined with the geochemical investigation is essential to understand paleoenvironmental changes, a robust magnetostratigraphic model for the studied FeMn crusts is difficult to obtain due to the absence and loss of primary magnetization. Since FeMn nodules and crusts from the Pacific Ocean contain biogenic magnetite produced by magnetotactic bacteria (MTB) as a primary remanence carrier, a magnetic study was conducted on quantified bacterial cells produced by distinct bacterial species. Magnetic properties of quantified bacterial magnetite depend on the quantity of MTB cells rather than on the bacterial species or cell type (lysed or whole). This study also estimates the carbon content of MTB cells and discusses its relationship to the global carbon cycle. In order to understand the relationship between the deposition of Fe and Mn, biogenic magnetite produced by MTB and environmental conditions, a study was conducted on an IODP core from the Great Barrier Reef (GBR), Australia. The magnetic mineralogical and geochemical data from IODP Expedition 325 - Hole M0058A reveals the depositional history of the GBR margin during the interval of MIS 7 to 5 and MIS 1. In this case, the deposition of Fe and Mn in mixed siliciclastic-carbonate sediments

is related to terrigenous input, while the presence of biogenic magnetite is related to the arid climatic conditions. The arid periods over NE Australia were established after the glacial/interglacial transition and at the middle Holocene, favoring dust deposition and promoting primary productivity.

The occurrence of Fe and Mn in distinct marine environments corresponds to different magnetic implications. The presence of biogenic magnetite in FeMn nodules and crusts is linked to the oxygenation conditions while the biogenic magnetite in mixed siliciclastic carbonate sediments is associated with the increase of primary productivity enhanced by arid climatic conditions.

Keywords: Rio Grande Rise. Tropic Seamount. Clarion Clipperton Zone. Ferromanganese deposits. Rock magnetism. Paleomagentism. Magnetofossils. Carbon sequestration.

LIST OF ABBREVIATIONS

AF Alternating Field

AGM Alternating Gradient Magnetometer

ARM Anhysteretic Remanent Magnetization

BIRM Backfield Isothermal Remanent Magnetization

CCZ Clarion-Clipperton Zone

Ce Cerium

CFA Carbonate Flourapatite

ChRM Characteristic Remanent Magnetization

CISP Cannary Island Seamount Province

ERGR Eastern Rio Grade Rise

Fe Iron

FeMn Ferromanganese

FORC First Order Reversal Curve

GBR Great Barrier Reef

HB Hard Biogenic magnetite

H_c Magnetic Coercivity

Ho Holmium

ICP-MS Inductively Coupled Plasma Mass Spectrometry

ICP-OES Inductively Coupled Plasma Optical Emission Spectrometry

IRM Isothermal Remanent Magnetization

IT-1 *Magnetofaba australis*

Mbsf Meters Below Sea Floor

MD Multidomain

MIS Marine Isotope Stages

Mn Manganese

M_{rs} Magnetic Remanence

M_s Saturation Magnetization

MTB Magnetotactic Bacteria

MV-1^T *Magnetovibrio blakemorei*

NACM Northeast Australian Continental Margin

Nd Neodymium

OMZ Oxygen Minimum Zone

ORP Oxidation-reduction potential

OSTZ Oxic-Suboxic Transition Zone

PCA Principal Component Analysis

PSD Pseudosingle Domain

REY Rare Earth Elements and Yttrium

SD Single Domain

SEM Scanning Electron Microscopy

SIRM Saturation Isothermal Remanent Magnetization

SN Shale Normalized

SP Superparamagnetic

TEM Transmission Electron Microscopy

TS Tropic Seamount

VSM Vibrating Sample Magnetometer

WRGR Western Rio Grande rise

SUMMARY

1 THESIS INTRODUCTION

Marine polymetallic nodules, also termed as manganese nodules or ferromanganese nodules, are mineral concretions of manganese and iron oxides that form on the ocean bottom around a nucleus at a very slow growth rate (Cronan, 1977; Hein and Koschinsky, 2014). As a result of a very slow growth rate, polymetallic nodules have a high amount of rare earth elements of economic interest (Cronan, 1978; Hein et al., 2013). Together with the marine cobalt-rich FeMn crusts, the nodules are also termed as marine ferromanganese deposits (Hein and Koschinsky, 2014).

FeMn crusts are composed of Fe oxyhydroxide and Mn oxide precipitating on the seabed and growing over tens of millions of years. A wide variety of elements such as Co, Ti, Mn, Ni, Pt, Zr, Nb, Te, Bi, Mo, W, Th, Ni, Cu, Co, Mn, Mo, and Li have been described as a potential future resource (Hein et al., 2003; 2010; 2013).

Several studies have performed magnetostratigraphic dating of FeMn crusts from the Pacific Ocean and China Sea by using magnetic scanning techniques as well as traditional cryogenic magnetic methods (Joshima and Usui, 1998; Oda et al., 2011; Yuan et al., 2017; Usui et al., 2017; Noguchi et al., 2017a, 2017b; Yi et al., 2020; Oda et al., 2023).

Magnetic studies on FeMn crusts/nodules from the Pacific Ocean and China Sea have suggested that the primary source of remanent magnetization in FeMn crusts is the biogeochemical remanent magnetization caused by the presence of magnetotactic bacteria (Oda et al., 2018; Yuan et al., 2020). Although magnetite biomineralization has been reported for the hydrogenetic Fe-Mn deposits, a major part of the Fe phase is the nano-meter-sized X-ray amorphous Fe hydroxide and poorly crystalline Fe-bearing vernadite (Guan et al., 2017; Bogdanova et al., 2008; Hein and Koschinsky, 2014; Jiang et al., 2021). Moreover, the process of magnetite biomineralization in FeMn crusts is not well-detailed in previous studies. The role of magnetite-producing bacteria in the growth of FeMn crusts is poorly understood. Moreover, magnetite preservation as a remanence carrying magnetic minerals in varying environmental conditions is debatable.

Magnetic minerals are iron-bearing minerals that occur in nature as oxides, hydroxides, and sulphides. These minerals are sensitive to oxidative and reductive environmental conditions during the passage of their existence. (Liu et al., 2012; Roberts, 2015). Their precipitation is chemically controlled by the presence of Fe, pH conditions, and oxidative reductive potential. (Emerson et al., 2012). These characteristics of magnetic minerals generate rock magnetism and palaeomagnetism.

Magnetic studies on FeMn crusts from the Atlantic Ocean are scarce if not existing. In this research, Chapters 1 and 2 explore the magnetic properties related to geochemical and environmental conditions in a nodule sample from the Pacific Ocean, in the fresh hydrogenetic (non-altered) layers and phosphatized (diagenetically altered) layers of FeMn crusts from RGR and TS. This research section focuses on performing rock magnetism and paleomagnetism to understand whether remanence-carrying magnetic minerals are present in the selected FeMn crust samples from the Atlantic Ocean. If so, whether robust magnetic stratigraphy can be implemented, and if not, why. We further discuss the environmental conditions for the preservation of remanence carrying magnetic minerals, especially biogenic magnetite in FeMn crusts from the Atlantic Ocean.

Since the major magnetic component in FeMn crusts and nodules is biogenic magnetite produced by magnetotactic bacteria (MTB) (Joshima and Usui, 1998; Oda et al., 2011; Yuan et al., 2017; Usui et al., 2017; Noguchi et al., 2017a, 2017b; Yi et al., 2020; Oda et al., 2023), it is essential to elaborate the magnetic properties of biogenic magnetite produced by MTB. MTB produce magnetosomes, which are intracellular organelles that contain nanometer-sized, membrane-bound magnetite crystals (Faivre and Schüler, 2008; Frankel, 2009). Within the cell, these crystals are organized into single or multiple chains, allowing MTB to orient themselves along a magnetic field (magnetotaxis) (Yan et al., 2012). In this research (Chapter 3), we study the efficiency of magnetic methods as well as the magnetic response of different (lysed and whole) MTB cells, of distinct species (the cultured *Magnetovibrio blakemorei* strain MV-1^{T} and *Magnetofaba australis* strain IT-1), with concentrations varying from 10^2 to 10^9 per sample. Hence this section defines the detection limit of the commonly used magnetic methods to study the biogenic magnetite based on the number of cells, cell types and bacterial species.

Marine bacterial communities are also known for carbon sequestration (Jiao and Zheng, 2011; Jaya et al., 2019). Many microbes and bacteria have been linked to the dissolved organic carbon flux in marine settings (Sarmento and Gasol, 2012; Ribeiro et al., 2016; Bergo et al., 2017). Iron and carbon cycling are important contributions of MTB, hence magnetofossils (magnetosomal magnetic nanoparticles which are preserved in the sediments after bacterial death) could be used as paleoenvironmental indicators (Kirschvink and Chang, 1984). Previously, Faivre et al. (2007) proposed that carbon plays no role in the formation of magnetosomes. However, Staniland et al. (2007) later concluded that carbon-rich conditions accelerate magnetosome production. The relationship between organic C flux and the abundance of different magnetofossil morphologies, and the relationship between high organic

carbon and biogenic magnetite in Holocene sediments has been previously reported (Yamazaki and Kawahata, 1998; Snowball et al., 1999).

In Chapter 3, we also estimate the carbon content of MTB cells and provide preliminary insights into potential role of MTB in global carbon cycling processes.

Previous studies have demonstrated the increase in Fe and Mn, with the increase in magnetic properties and the presence of biogenic magnetite in different sedimentary environments (Cornaggia et al., 2020; Stolz et al., 1989). Mn incorporation inside the biogenic magnetite crystals further explains the co-occurrence of biogenic magnetite and Mn in marine environments (Keim et al., 2009). However, the co-occurrence of Fe, Mn and biogenic magnetite is distinctive in different marine environments. It is essential to understand the deposition of Fe and Mn in the shallow marine environment where the presence of biogenic magnetite has been previously reported (Herrero-Bervera and Jovane, 2013; Yokoyama et al. 2011; Abrajevitch and Kodama, 2011; McNeill et al., 1993; Barton et al., 1993a; Barton et al., 1993b). For this reason, we choose to study the relationship of Fe, Mn, and biogenic magnetite in one of the most important biogenically dominated shallow marine environments. The Great Barrier Reef (GBR), located on the northeastern margin of Australia, is the world's largest feature made up of living organisms. It is the largest coral reef system in the world, and modern climatic alterations are rapidly changing its ecosystem. To understand the implications of these changes, it is important to reconstruct the geological history of GBR. The fourth and last chapter of this study performs the environmental magnetism and geochemical study of the mixed siliciclastic-carbonate sequence of Hole M0058A, recovered during the International Ocean Discovery Program (IODP) Expedition 325 in the GBR (Webster et al., 2011; Yokoyama et al., 2011, Expedition 325 Scientists, 2011). Radiocarbon dating for the younger part of the core and Oxygen isotope measurements compared to LR04 $\delta^{18}O$ records confirmed the presence of Marine Isotope Stages (MIS) and the maximum age of ca. 220 ka for the core Hole M0058A (Harper et al., 2015). A cyclic pattern is observed within the lithological changes of Hole M0058A. Moreover, a reciprocal sedimentation model of alternating terrigenous siliciclastic sediments and neritic carbonates in response to sea-level rise and fall and interglacial-glacial changes has been well established by previous studies (Harper et al., 2015, Dunbar and Dickens, 2003).

The occurrence of Fe, Mn, and biogenic magnetite in mixed siliciclastic carbonate sediments from the GBR region in northeastern Australia exhibits a different paleoenvironmental scenario linked to the sea level variations, shoreline progradation and retrogradation, surface run-off and arid climatic conditions. In this research section, we investigate the deposition of Fe and Mn

and the occurrence of biogenic magnetite in mixed siliciclastic-carbonate sediments from the northeastern Australian Margin. Furthermore, a detailed environmental interpretation of the magnetic and geochemical results is discussed in Chapter 4.

In this thesis, the presence of Fe and Mn in different marine environments, the presence of biogenic magnetite in FeMn deposits and their relation to in situ environmental conditions and terrigenous input have been studied in detail.

References

Abrajevitch, A., & Kodama, K. (2011). Diagenetic sensitivity of paleoenvironmental proxies: A rock magnetic study of Australian continental margin sediments. *Geochemistry, geophysics, geosystems*, *12*(5). https://doi.org/10.1029/2010GC003481.

Barton, C. E. (1993b). Paleomagnetic and mineral magnetic record of sediments from the Queensland Trough: Results for Leg 133, Hole 823A, edited by JA McKenzie et al. In *Proc. Ocean Drill. Program Sci. Results* (Vol. 133, pp. 563-571). https://doi.org/10.2973/odp.proc.sr.133.262.1993

Barton, C. E., Lackie, M., & Peerdeman, F. M. (1993a). Environmental control of magnetic properties of upper-slope sediments near the Great Barrier Reef: results from Leg 133, Site 820. In *Proceedings of the Ocean Drilling Program, Scientific Results* (pp. 543-562). ODP, Texas A&M University, College Station. https://doi.org/10.2973/odp.proc.sr.133.261.1993.

Bergo, N. M., Signori, C. N., Amado, A. M., Brandini, F. P., & Pellizari, V. H. (2017). The partitioning of Carbon biomass among the pico-and nano-plankton community in the South Brazilian Bight during a strong summer intrusion of South Atlantic central water. *Frontiers in Marine Science*, *4*, 238.

Bogdanova, O. Y., Gorshkov, A. I., Novikov, G. V., & Bogdanov, Y. A. (2008). Mineralogy of morphogenetic types of ferromanganese deposits in the world ocean. Geology of Ore Deposits, 50, 462-469.

Cornaggia, F., Bernardini, S., Giorgioni, M., Silva, G. L., Nagy, A. I. M., & Jovane, L. (2020). Abyssal oceanic circulation and acidification during the Middle Eocene Climatic Optimum (MECO). *Scientific reports*, *10*(1), 6674.

Cronan, D. S. (1977). Deep-sea nodules: distribution and geochemistry. In *Elsevier Oceanography Series* (Vol. 15, pp. 11-44). Elsevier.

Cronan, D. S. (1978). Manganese nodules: controversy upon controversy. *Endeavour*, *2*(2), 80-84.

Dunbar, G. B., & Dickens, G. R. (2003). Late Quaternary shedding of shallow-marine carbonate along a tropical mixed siliciclastic–carbonate shelf: Great Barrier Reef, Australia. *Sedimentology*, *50*(6), 1061-1077.

Emerson, D., Roden, E., & Twining, B. (2012). The microbial ferrous wheel: iron cycling in terrestrial, freshwater, and marine environments. *Frontiers in microbiology*, *3*, 383.

Faivre, D., Böttger, L. H., Matzanke, B. F., & Schüler, D. (2007). Intracellular magnetite biomineralization in bacteria proceeds by a distinct pathway involving membrane-bound ferritin and an iron (II) species. *Angewandte Chemie International Edition*, *46*(44), 8495-8499.

Faivre, D., & Schuler, D. (2008). Magnetotactic bacteria and magnetosomes. *Chemical reviews*, *108*(11), 4875-4898.

Frankel, R. B. (2009). The discovery of magnetotactic/magnetosensitive bacteria. *Chinese Journal of Oceanology and Limnology*, *27*(1), 1.

Guan, Y., Sun, X., Jiang, X., Sa, R., Zhou, L., Huang, Y., ... & Wang, C. (2017). The effect of Fe-Mn minerals and seawater interface and enrichment mechanism of ore-forming elements of polymetallic crusts and nodules from the South China Sea. *Acta Oceanologica Sinica*, *36*, 34-46.

Harper, B. B., Puga-Bernabéu, Á., Droxler, A. W., Webster, J. M., Gischler, E., Tiwari, M., ... & Röhl, U. (2015). Mixed carbonate–siliciclastic sedimentation along the great barrier reef

upper slope: A challenge to the reciprocal sedimentation model. *Journal of Sedimentary Research*, *85*(9), 1019-1036.

Hein, J. R., & Koschinsky, A. (2014). Deep-ocean ferromanganese crusts and nodules.

Hein, J. R., Conrad, T. A., & Staudigel, H. (2010). Seamount mineral deposits: a source of rare metals for high-technology industries. *Oceanography*, *23*(1), 184-189.

Hein, J. R., Koschinsky, A., & Halliday, A. N. (2003). Global occurrence of tellurium-rich ferromanganese crusts and a model for the enrichment of tellurium. Geochimica et Cosmochimica Acta, 67(6), 1117-1127.

Hein, J. R., Mizell, K., Koschinsky, A., & Conrad, T. A. (2013). Deep-ocean mineral deposits as a source of critical metals for high-and green-technology applications: Comparison with land-based resources. Ore Geology Reviews, 51, 1-14.

Herrero-Bervera, E., & Jovane, L. (2013). On the palaeomagnetic and rock magnetic constraints regarding the age of IODP 325 Hole M0058A. *Geological Society, London, Special Publications*, *373*(1), 279-291. https://doi.org/10.1144/SP373.19.

Jaya, P., Nathan, V. K., & Ammini, P. (2019). Characterization of marine bacterial carbonic anhydrase and their CO2 sequestration abilities based on a soil microcosm. *Preparative Biochemistry & Biotechnology*, *49*(9), 891-899.

Jiang, X., Zhao, X., Zhao, X., Chou, Y. M., Hein, J. R., Sun, X., ... & Liu, Q. (2021). A magnetic approach to unravelling the paleoenvironmental significance of nanometer-sized Fe hydroxide in NW Pacific ferromanganese deposits. *Earth and Planetary Science Letters*, *565*, 116945.

Jiao, N., & Zheng, Q. (2011). The microbial carbon pump: from genes to ecosystems. *Applied and Environmental Microbiology*, *77*(21), 7439-7444.

Joshima, M., & Usui, A. (1998). Magnetostratigraphy of hydrogenetic manganese crusts from Northwestern Pacific seamounts. *Marine Geology*, *146*(1-4), 53-62.

Keim, C. N., Lins, U., & Farina, M. (2009). Manganese in biogenic magnetite crystals from magnetotactic bacteria. *FEMS microbiology letters*, *292*(2), 250-253.

Kirschvink, J. L., & Chang, S. B. R. (1984). Ultrafine-grained magnetite in deep-sea sediments: Possible bacterial magnetofossils. *Geology*, *12*(9), 559-562.

Liu, Q., Roberts, A. P., Larrasoana, J. C., Banerjee, S. K., Guyodo, Y., Tauxe, L., & Oldfield, F. (2012). Environmental magnetism: principles and applications. *Reviews of Geophysics*, *50*(4).

McNeill, D. F. (1993a). A review and comparison of carbonate rock magnetization: Leg 133, Queensland Plateau, Australia. In *Proc. Ocean Drilling Program, Scientific Results* (Vol. 133, pp. 749-753). https://doi.org/10.2973/odp.proc.sr.133.284.1993.

McNeill, D. F., Guyomard, T. S., & Hawthorne, T. B. (1993b). Magnetostratigraphy and the nature of magnetic remanence in platform/periplatform carbonates, Queensland Plateau, Australia. In *Proc. Ocean Drilling Program, Scientific Results* (Vol. 133, pp. 573-587). https://doi.org/10.2973/odp.proc.sr.133.263.1993.

Noguchi, A., Oda, H., Yamamoto, Y., Usui, A., Sato, M., & Kawai, J. (2017). Scanning SQUID microscopy of a ferromanganese crust from the northwestern Pacific: Submillimeter scale magnetostratigraphy as a new tool for age determination and mapping of environmental magnetic parameters. *Geophysical Research Letters*, *44*(11), 5360-5367.

Noguchi, A., Yamamoto, Y., Nishi, K., Usui, A., & Oda, H. (2017). Paleomagnetic study of ferromanganese crusts recovered from the northwest Pacific—Testing the applicability of the magnetostratigraphic method to estimate growth rate. *Ore Geology Reviews*, *87*, 16-24.

Oda, H., Katanoda, W., Usui, A., Murayama, M., & Yamamoto, Y. (2023). Rotation of a ferromanganese nodule in the Penrhyn Basin, South Pacific, tracked by the Earth's magnetic field. *Geochemistry, Geophysics, Geosystems*, *24*(3), e2022GC010789.

Oda, H., Nakasato, Y., & Usui, A. (2018). Characterization of marine ferromanganese crust from the Pacific using residues of selective chemical leaching: identification of fossil

magnetotactic bacteria with FE-SEM and rock magnetic methods. *Earth, Planets and Space*, *70*(1), 1-10.

Oda, H., Usui, A., Miyagi, I., Joshima, M., Weiss, B. P., Shantz, C., ... & Baudenbacher, F. J. (2011). Ultrafine-scale magnetostratigraphy of marine ferromanganese crust. *Geology*, *39*(3), 227-230.

Ribeiro, C. G., Dos Santos, A. L., Marie, D., Pellizari, V. H., Brandini, F. P., & Vaulot, D. (2016). Pico and nanoplankton abundance and carbon stocks along the Brazilian Bight. *PeerJ*, *4*, e2587.

Roberts, A. P. (2015). Magnetic mineral diagenesis. *Earth-Science Reviews*, *151*, 1-47.

Sarmento, H., & Gasol, J. M. (2012). Use of phytoplankton-derived dissolved organic carbon by different types of bacterioplankton. *Environmental Microbiology*, *14*(9), 2348-2360.

Snowball, I., Sandgren, P., & Petterson, G. (1999). The mineral magnetic properties of an annually laminated Holocene lake-sediment sequence in northern Sweden. *The Holocene*, *9*(3), 353-362.

Staniland, S., Ward, B., Harrison, A., van der Laan, G., & Telling, N. (2007). Rapid magnetosome formation shown by real-time x-ray magnetic circular dichroism. *Proceedings of the National Academy of Sciences*, *104*(49), 19524-19528.

Stolz, J. F., Chang, S. B. R., & Kirschvink, J. L. (1989). Biogenic magnetite in stromatolites. I. Occurrence in modern sedimentary environments. *Precambrian Research*, *43*(4), 295-304.

Usui, A., Nishi, K., Sato, H., Nakasato, Y., Thornton, B., Kashiwabara, T., ... & Urabe, T. (2017). Continuous growth of hydrogenetic ferromanganese crusts since 17 Myr ago on Takuyo-Daigo Seamount, NW Pacific, at water depths of 800–5500 m. *Ore Geology Reviews*, *87*, 71-87.

Webster, J.M., Yokoyama, Y., Cotterill, C., and the Expedition 325 Scientists (2011). Proc. IODP, 325: Tokyo (Integrated Ocean Drilling Program Management International, Inc.

Yamazaki, T., & Kawahata, H. (1998). Organic carbon flux controls the morphology of magnetofossils in marine sediments. *Geology*, *26*(12), 1064-1066.

Yan, L., Zhang, S., Chen, P., Liu, H., Yin, H., & Li, H. (2012). Magnetotactic bacteria, magnetosomes and their application. *Microbiological research*, *167*(9), 507-519.

Yi, L., Medina-Elizalde, M., Kletetschka, G., Yao, H., Simon, Q., Paterson, G. A., ... & Zhu, R. (2020). The potential of marine ferromanganese nodules from Eastern Pacific as recorders of Earth's magnetic field changes during the past 4.7 Myr: A geochronological study by magnetic scanning and authigenic 10Be/9Be dating. *Journal of Geophysical Research: Solid Earth*, *125*(7), e2019JB018639.

Yokoyam, Y., Webster, J. M., Cotterill, C., Braga, J. C., Jovane, L., Mills, H., Morgan, S., & Suzuki, A. (2011). IODP Expedition 325: Great Barrier Reefs reveals past sea-level, climate and environmental changes since the last ice age. *Scientific Drilling*, *12*, 32-45.

Yuan, W., Zhou, H., Yang, Z., Hein, J. R., & Yang, Q. (2020). Magnetite magnetofossils record biogeochemical remanent magnetization in hydrogenetic ferromanganese crusts. *Geology*, *48*(3), 298-302.

Yuan, W., Zhou, H., Zhao, X., Yang, Z., Yang, Q., & Zhu, B. (2017). Magnetic stratigraphic dating of marine hydrogenetic ferromanganese crusts. *Scientific Reports*, *7*(1), 16748.

2 PRESENCE OF BIOGENIC MAGNETITE IN FERROMANGANESE NODULES (CHAPTER 1)

Manuscript published in *Environmental Microbiology Reports*

Muhammad Bin Hassan[1], Daniel Rodelli[1], Mariana Benites[1], Fernanda Abreu[2], Bramley Murton[3] and Luigi Jovane[1]

[1]Instituto Oceanográfico, Universidade de São Paulo, São Paulo, Brazil

[2]Instituto de Microbiologia Paulo de Góes, Universidade Federal do Rio de Janeiro, Brazil

[3]National Oceanography Center, Southampton, UK

Summary

Transmission electron microscopy (TEM) and rock magnetic study of ferromanganese nodule sample JC120-104B collected from Clarion-Clipperton zone (CCZ) in the eastern Pacific Ocean indicate the presence of biogenic magnetite (magnetofossils). First order reversal curves (FORCs) and decomposition of isothermal remanent magnetization (IRM) curves were used as the main tool for the characterization of magnetic properties of the bulk magnetic minerals present in the sample. TEM was performed for the direct identification of biogenic magnetic minerals (magnetofossils). The nodule sample has distinctive alternating Mn and Fe-rich layers per micro-X-ray fluorescence data. While diagenetic precipitation of Mn is known for the less oxygenated environment, the presence of biogenic magnetite is also common in the environments where the supply of oxygen is limited. Moreover, the increase in magnetic properties is consistent with the increase in Mn content, which is related to favourable conditions for Mn precipitation as well as magnetite biomineralization in oxic suboxic transition zone. Investigations on magnetofossil fingerprints lead to a better understanding of paleoenvironmental conditions involved in the formation and growth of deep-sea ferromanganese nodules.

2.1 Introduction

Magnetotactic bacteria (MTB) have been detected in different water columns and sediments from freshwater, marine and hypersaline environments (Lefèvre and Bazylinski, 2013). MTB are a heterogeneous group of prokaryotes that produce chains of membrane-enclosed single domain (SD) magnetite (Fe_3O_4) or greigite (Fe_3S_4) crystals, magnetosomes (Bazylinski and Frankel, 2004; Lefèvre and Wu, 2013). MTB use magnetosomes to move and align their entire

body along magnetic fields in search of suitable environmental conditions by a process called magnetotaxis (Frankel, 2009). Magnetosomes have characteristic magnetic fingerprints that can be detected as non-interacting SD particles using rock magnetic non-destructive techniques (Moskowitz et al., 1993; Heslop and Roberts, 2012; Jovane et al., 2012).

The presence of MTB in sediments as magnetofossils has been reported as a proxy for the reconstruction of past climate due to their relation with the concentration of organic matter and high-productivity climatic events (Schumann et al., 2008; Savian et al., 2016; Chang et al., 2018). Most MTB are found in coastal environments; however, they have additionally been reported in all types of environments including lakes and wet soils (Bazylinski and Frankel, 2004; Bazylinski and Schübbe, 2007; Lefèvre and Bazylinski, 2013; Dong et al., 2016). Deep-ocean (>5000 m) MTB collected from South Atlantic Ocean sediments were studied by Petermann and Bleil (1993).

The Clarion-Clipperton zone (CCZ) is renowned among researchers due to different polymetallic nodules rich in manganese (Mn), iron (Fe), cobalt (Co), copper (Cu) and nickel (Ni). The contribution of biomineralization to the sediments from CCZ has already been documented (Wang et al., 2009a). Microorganisms associated with the nodules are significantly different than those which are found in the surrounding sediments. Moreover, recent studies have shown that the bacterial communities found in the inner portion of the nodules differ from outer portion of the same nodule (Tully and Heidelberg, 2013). Hydrogenetic ferromanganese crusts recovered from Pacific Ocean also demonstrate the presence of magnetofossils among other micro particles (Oda et al., 2018).

The CCZ is defined as the seabed and subseafloor that occurs between the Clarion and Clipperton Fracture zones in the east Pacific. The CCZ is 4000–4500 m deep and surrounded by volcanic seamounts rising to 2500 m and approximately N-S-oriented horsts and grabens, a few kilometres in length, and 100–300 m in height. The otherwise flat ocean floor is covered by pelagic clay and siliceous ooze (diatoms and radiolaria) sediments, deposited at a rate of 0.35-0.5 cm kyr^{-1} (Mewes et al., 2014).

The carbonate compensation (CCD) in the CCZ is somewhere in the range of 4200 and 4500 m water depth. The equatorial high bio-productivity zone is found south of the CCZ and produces one of the most extensive oxygen minimum zones in the global sea, caused by upwelling in the eastern Pacific (Stramma et al., 2010).

The oxygen minimum zone (OMZ) is wide, with a thickness of 400–1000 m, which is more prominent off-Mexico and extends towards the north and west (Zheng et al., 2000). Sediment deposition is affected by the flow of Antarctic Bottom Water (AABW), which is under 10 cm

s^{-1}, in a primarily north-westward direction and that is highly oxygenated (Johnson, 1972). Dissolved oxygen is detectable in the sediment pore water down to 3 mbsf (Mewes et al., 2014). In this work, we explored the presence of biogenic magnetite in deep ferromanganese nodule sample from CCZ. We show that ferromanganese nodules contain magnetofossil fingerprints. Moreover, the magnetic properties such as magnetic saturation, coercivity and remanence of the Mn-rich layers of the nodule are higher than they are in the Fe-rich layers; the Mn-rich layers are the result of the diagenetic input of metals sourced from the oxic-suboxic transition zone (OSTZ) where they are mobilized by diagenetic processes and then migrate to the nodules at the seabed.

2.2 Methods

The ferromanganese nodule sample JC120-104B (Fig. 2) was collected from 4130 m water depth by Agassiz Trawl method at the latitude 13° 30' 42.012'N, and longitude 116° 35' 10.32'W (Fig. 1). The nodule was initially embedded in a 6:1 solution of Epoxiglass 1204 epoxy resin and Epoxiglass 1604 hardener and kept under vacuum for 6 h in order to ensure resin penetration. The sample was then dried in an oven for 2 days. Once the resin was completely dried, the nodule was cut in half. A second cut was made parallel to the first one, in order to get 5 mm thick slabs. One slab was used to prepare a 100 µm thin section for micro-X-ray fluorescence (µ-XRF) and scanning electron microscopy analyses, which are detailed in the study by Benites et al. (2018). The other slab was kept for rock magnetic studies. A 10 g powdered nodule sample was used to prepare for transmission electron microscopy (TEM).

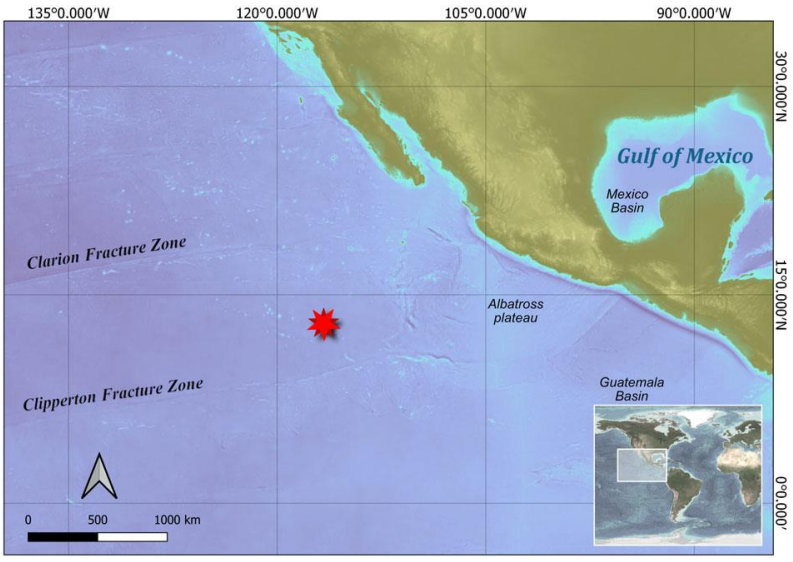

Fig. 1. Map showing CCZ, red star indicates the location of Fe-Mn nodule sample JC120-104B.

2.2.1 Transmission electron microscopy

A 10 g of nodule sample was gently crushed, powdered and passed through the sieve of 150 μm. To extract the magnetic particles from the powdered sample, the sample was mixed with acetate buffer (pH 4.0) according to Strehlau et al. (2014). Samples were maintained under constant agitation at 20ºC overnight. Magnetic concentration using a magnet and washing steps with MilliQ were performed before sample deposition in formvar–carboncoated grids. Samples were observed on an FEI Tecnai Spirit (FEI Company) at 120 kV.

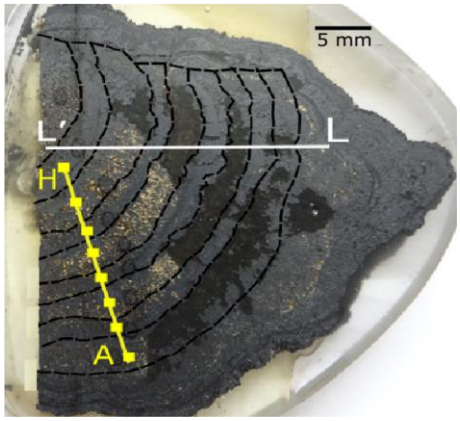

Fig. 2. Ferromanganese nodule sample embedded in the resin. L-L´ line shows the μ-XRF (micro-X Ray Fluorescence) analysis profile, while A–H line shows the location of subsamples (about 2 mm cubes) collected for rock magnetic studies.

2.2.2 Rock magnetic studies

Eight subsamples of about 2 mm cubes were collected from the resin fitted sample. (Fig. 2). To identify magnetic minerals, their domain state(s), and magnetic interactions among magnetic particles, we obtained hysteresis cycles, FORCs, thermomagnetic curves and isothermal remanent magnetization (IRM) acquisition curves at room temperature for each subsample (A-H) using an alternating gradient magnetometer (AGM MicroMag™ 2900) at the Centro Oceanográfico de Registros Estratigráficos (CORE) of the Instituto Oceanográfico of the Universidade de São Paulo (IOUSP).

Hysteresis measurements (Supporting Information) were performed with the maximum applied field of 1 T. Hysteresis parameters such as magnetic saturation (M_s), remanence of saturation (Mrs), and magnetic coercivity (H_c) were calculated after correction for paramagnetic contribution.

FORC diagrams are being widely used as a tool for detecting magnetofossils (Egli, 2004; Jovane et al., 2012; Roberts et al., 2014). FORC diagrams are contour plots of the second derivative of magnetic fields H_u and H_c, which are related to the coercivity (H_c) and

magnetostatic interactions (H_u), measured in a series of partial hysteresis curves (Roberts et al., 2000). The dimension of biogenic magnetite crystals is optimized for SD magnetic behaviour, and the crystals align in chains so that they produce a strong net magnetic anisotropy; therefore, the magnetosome chain behaves like a single long, noninteracting, SD particle (Dunin-Borkowski et al., 1998). For FORC measurements, 297 curves were measured with an averaging time of 150 ms, in the space between H_c = 0–100 mT and Hu = 15 mT (Egli et al., 2010). FORC diagrams were produced with a smoothing factor (SF) of 6 (Roberts et al., 2000) using the software of Heslop and Roberts (2012) (Fig. 6).

The magnetic susceptibility variation as a function of temperature was measured for the two selected subsamples, i.e., Mn rich subsample (B) and Fe-rich subsample (C), with a temperature range from room temperature up to 700ºC (Fig. 5). The measurement was performed using an Agico MKF1-FA Kappabridge located at the CORE of IOUSP and processed using the Sufyte5W software. The data were normalized between 0 and 1 for visual ease for both subsamples. Curie temperatures for the mineral phases were determined using the double tangent method.

We obtained IRM acquisition curves by applying an increasing field until saturation (SIRM) at 1 T. IRM curves were decomposed into different coercivity components using cumulative log-Gaussian (CLG) functions provided by the software of Kruiver et al. (2001) (Fig. 6).

2.3 Results and discussion

The magnetic properties, i.e., magnetic saturation (M_s), magnetic coercivity (H_c), and magnetic remanence (M_r) are plotted with the elemental concentration data (Fig. 3). A clear correspondence between Mn-rich layers and magnetic properties of the nodule sample is observed. The magnetic properties such as magnetic saturation, magnetic coercivity, and magnetic remanence increase with the increase in Mn content.

The thermomagnetic heating curves for both the Mn- and Fe-rich layers indicate the presence of magnetite, as both curves fall at exactly 585°C (Fig. 5), which is the typically Curie temperature for pure magnetite (Lowrie, 1990). The cooling curves show a rapid increase in susceptibility below ~400°C, with a peak value one order of magnitude higher that the value of the heating curve. This can be linked to irreversible mineralogical transformations during the heating process.

Overall, the FORC diagrams (Fig. 6) show a horizontal ridge beginning at 4 mT with the maximum peaks above 50 mT on the H_c axis. The vertical spread along the H_u axis which is

indicative of magnetostatic interactions, is only a few mT for almost all FORCs. The FORC signatures were slightly wider at around 30 mT and narrower at 60 mT. FORC diagrams of magnetofossils from the literature, both cultivated and uncultivated predominantly have a narrow horizontal ridge with the primary peak in the region of 20–40 mT (Yamazaki, 2008; Abrajevitch and Kodama, 2009; Jovane *et al*., 2012; Roberts *et al*., 2011, 2012; Rodelli *et al*., 2018).

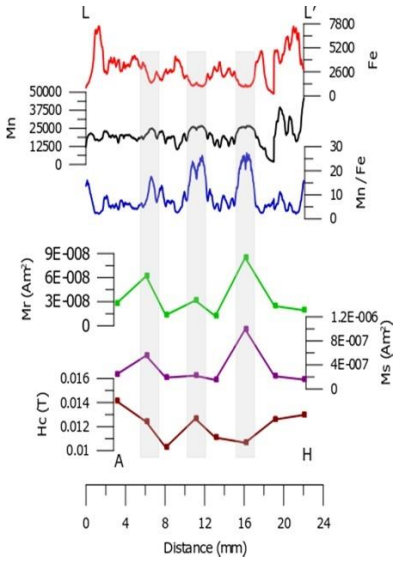

Fig. 3. Geochemical and rock magnetic data; Upper three curves are geochemical data in counts along profile L-L ´ shown in Fig. 2, lower three curves are rock magnetic data, i.e., magnetic coercivity (H_c), magnetic saturation (Ms) and magnetic remanence (Mr) along A to H as shown in Fig. 2.

These specifications indicate that the FORC diagrams of all the eight subsamples of the ferromanganese nodule showed coercivity and interaction ranges just identical to the FORCs of a non-interacting single-domain (SD) magnetite, which has been directly linked with the crystallographic state of the magnetosomes produced by MTB (Harrison and Feinberg, 2008; Roberts *et al*., 2014).

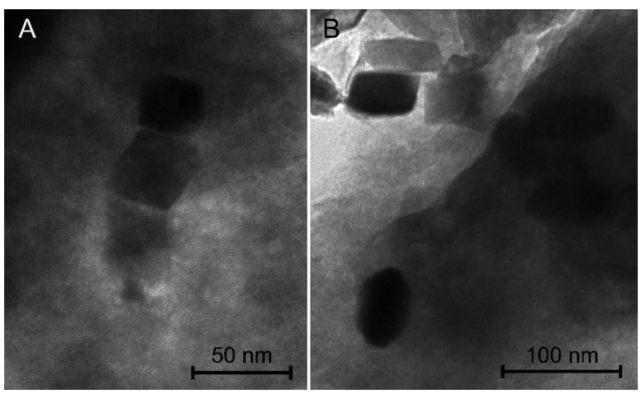

Fig. 4. TEM images of nanoparticles similar in size and shape to magnetosomes. A. Elongated octahedral magnetite crystal (biogenic soft; BS). B. Prismatic magnetite crystal (biogneic hard; BH).

IRM acquisition curves for the samples were fitted for either 5 or 6 coercivity components (Fig. 6). The lowest $B_{1/2}$ values are interpreted as coarse-grained detrital magnetite components (Roberts *et al*., 2011; Savian *et al*., 2014). Two intermediate coercivity components, having $B_{1/2}$ values ranging from 15 to 50 mT and relatively low dispersion values, are dominant in all subsamples (Fig. 6). These different intermediate-coercivity components were interpreted as biogenic soft (BS) and biogenic hard (BH), as described by Egli (2004) and Yamazaki (2008), which probably correspond to different morphologies of biogenic magnetite namely cubic and elongated crystal forms respectively. The high-coercivity components represented only a small fraction of the total IRM, which may be due to maghemite or haematite components. The magnetite crystal structures seen under TEM are similar to cubic as well as elongated biogenic magnetite-magnetosomes (Pósfai *et al*., 2013), considering both shape and size (Fig. 4).

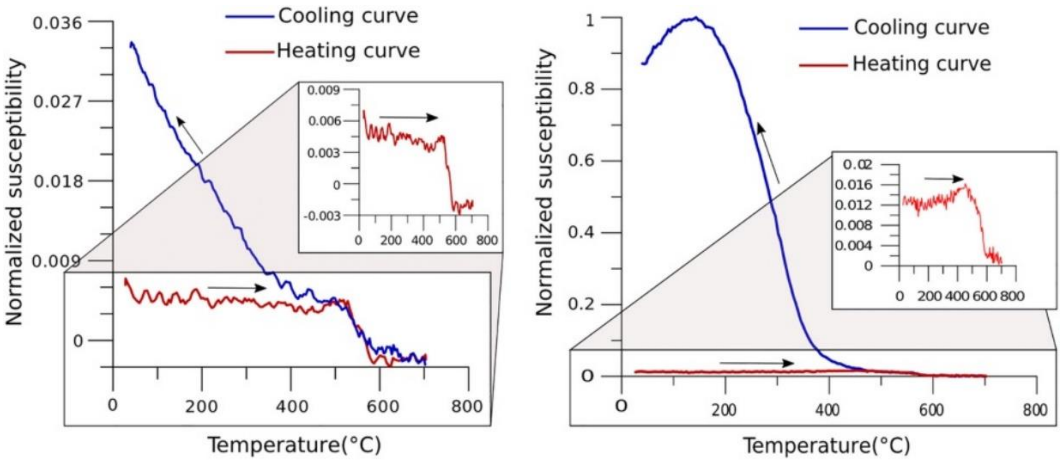

Fig. 5. Thermomagnetic curves: normalized magnetic susceptibility between 0 and 1 vs temperature obtained for; Left: Mn-rich sub-sample 'B', Right: Fe-rich subsample 'C'.

The same nodule sample was studied by Benites *et al*. (2018), where the geochemical data showed that there is no complete depletion of Fe in Mn-rich layers. However, in these layers, Mn/Fe ratio is higher with values >5 and up to 30 in comparison with Fe-rich layers, which show Mn/Fe close to 1 (Benites *et al*., 2018) (Fig. 3).

On the basis of geochemical and morphological data, the sample has been genetically classified as mixed type (hydrogenetic and diagenetic growth) with alternation of distinctive Mn- and Fe-rich layers (Benites *et al*., 2018). Mn-rich layers have been described as of diagenetic origin, which is the result of precipitation of metals, mainly Mn, Ni and Cu, originated from the diagenesis of organic matter in the OSTZ (Halbach *et al*., 1980, 1981). This scenario produces typical diagenetic layers of Mn/Fe values from 5 to 10. However, extremely high Mn/Fe values of 800 have been reported in Mn-rich layers of the mixed-type sample from the eastern CCZ,

where suboxic precipitation has been suggested (Wegorzewski and Kuhn, 2014). The nodule sample (Fig. 2) presented Mn-rich layers with Mn/Fe values of up to 30. We argue that the magnetic properties, such as magnetic saturation, coercivity, and remanence of Mn-rich layers were higher because of biogenic magnetite, which are structurally and chemically pure magnetite nanoparticles (Bazylinski and Moskowitz, 1997; Fischer *et al*., 2011). The formation of Mn-rich layers is favoured by shallow suboxic conditions in marine sediments (Benites *et al*., 2018) and magnetite biomineralization is related to OSTZ (Flies *et al*., 2005; Kopp and Kirschvink, 2008). Since there is no complete depletion of iron in the Mn-rich layers, hence the bioavailability of Fe for magnetite biomineralization is evident. Fe-rich layers are the result of oxic precipitation (Benites *et al*., 2018), which is less favourable for biogenic magnetite hence the magnetic properties (magnetic saturation, coercivity and remanence) are comparatively lower in Fe-rich layers than they are in Mn-rich layers. The presence of biogenic magnetite (magnetofossil) in ferromanganese crusts from the Pacific Ocean is a clear indication for the contribution of magnetite biomineralization in ferromanganese nodules; however, nodules differ from crusts based on the types of genesis as well as environment of growth. Biogenic magnetite can be produced either by intracellular biomineralization (i.e., biologically controlled) or extracellular biomineralization (i.e., biologically induced by different kinds of microbes) (Stolz *et al*., 1990; Vali *et al*., 2004; Bazylinski *et al*. 2007; Abrajevitch *et al*., 2016). Consequently, we do not exclude the possibility of either of the above-mentioned processes.

The CCZ is famous for the abundance of polymetallic ferromanganese nodules. Polymetallic nodules from the Eastern Pacific Ocean, studied by Wang *et al*. (2009b) identified biomineralization and contained different types of microbes (Wang *et al*., 2009b). Dong *et al*. (2016) detected the presence of magnetotactic bacteria in deep-sea sediments from the east Pacific nodule province. Our rock magnetic study and electron microscopy results of the nodule sample identify magnetofossils and their relation with the Mn-rich layers of diagenetic origin from OSTZ.

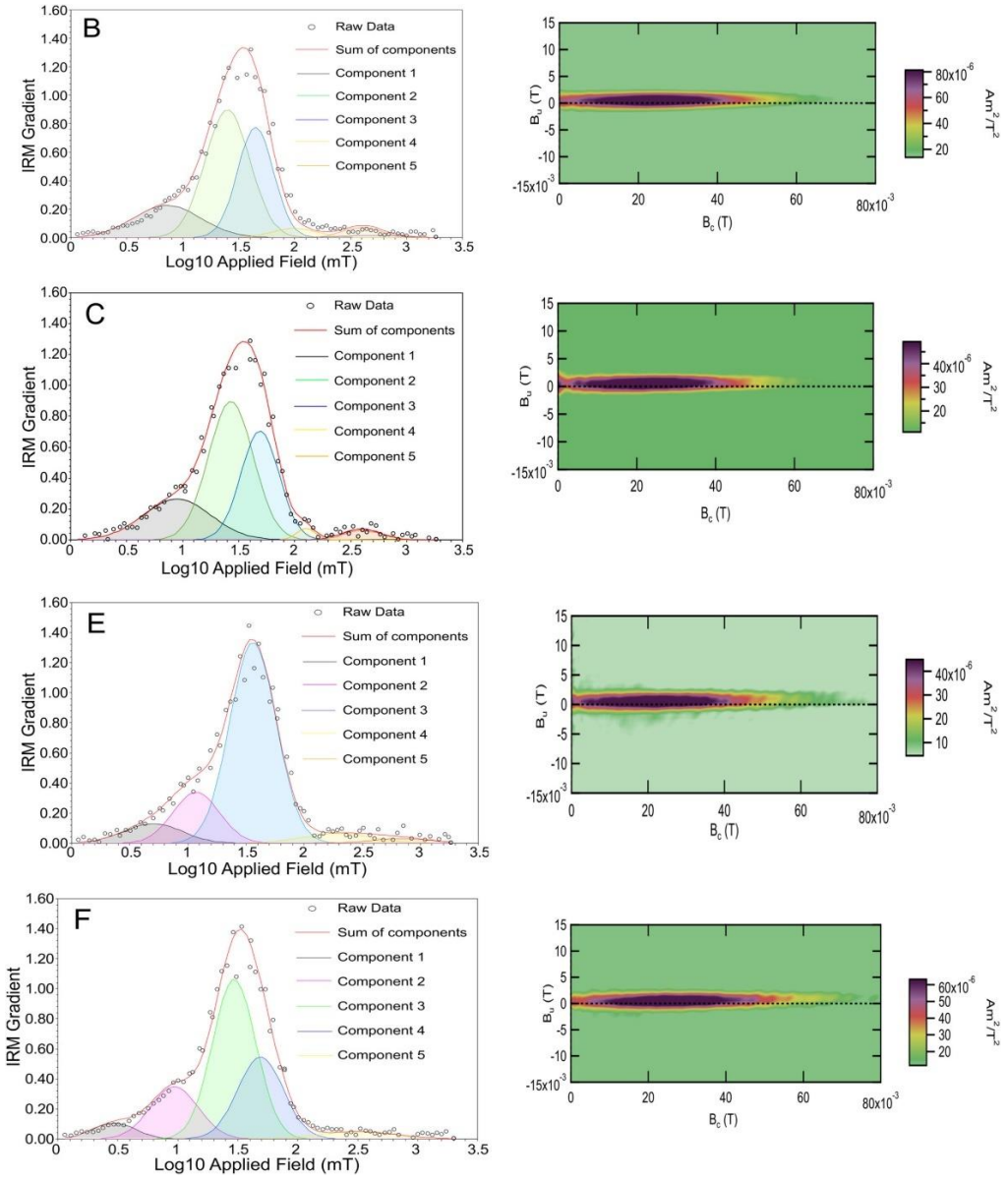

Fig. 6. Decomposition of IRM curves and FORCs; Left; decomposition of IRM curves of subsamples B, C, E and F. Green and blue curves in all samples show biogenic soft (BS) and biogenic hard (BH) components of magnetite. Right; FORCs of the corresponding subsamples.

2.4 Conclusions

Higher magnetic properties are consistent with Mn-rich layers within the nodule sample collected from the CCZ. Magnetic properties increased with the increase in Mn content due to the presence of magnetofossil which is structurally and chemically pure biogenic magnetite. The Mn-rich layers are the outcome of diagenetic precipitation in OSTZ while magnetite biomineralization is also favoured in the areas where oxygen supply is limited. FORC diagrams, Isothermal Remanent Magnetization (IRM) acquisition curves and TEM testify to the identification of biogenic magnetite, which is the main magnetic carrier in the nodule sample.

The presence of magnetofossils in ferromanganese nodules can be very useful tool for future paleomagnetic, paleo-oxygenation and paleoenvironmental studies of the deep-ocean system.

References

Abrajevitch, A., and Kodama, K. (2009) Biochemical vs. detrital mechanism of remanence acquisition in marine carbonates: a lesson from the K–T boundary interval. *Earth Planet Sci Lett* 286: 269– 277. https://doi.org/10.1016/j.epsl.2009.06.035.

Abrajevitch, A., Kondratyeva, L.M., Golubeva, E.M., Kodama, K., and Hori, R.S. (2016) Magnetic properties of iron minerals produced by natural iron-and manganese-reducing groundwater bacteria. *Geophys J Int* 206: 1340– 1351. https://doi.org/10.1093/gji/ggw221.

Bazylinski, D.A., and Frankel, R.B. (2004) Magnetosome formation in prokaryotes. *Nat Rev Microbiol* 2: 217. https://doi.org/10.1038/nrmicro842.

Bazylinski, D.A., and Moskowitz, B.M. (1997) Microbial biomineralization of magnetic iron minerals; microbiology, magnetism and environmental significance. *Rev Mineral Geochem* 35: 181– 223. https://doi.org/10.1515/9781501509247-008.

Bazylinski, D.A., and Schübbe, S. (2007) Controlled biomineralization by and applications of magnetotactic bacteria. *Adv Appl Microbiol* 62: 21– 62 https://doi.org/10.1016/s0065-2164(07)62002-4.

Bazylinski, D.A., Frankel, R.B., and Konhauser, K.O. (2007) Modes of biomineralization of magnetite by microbes. *Geomicrobiol J* 24: 465– 475. https://doi.org/10.1080/01490450701572259.

Benites, M., Millo, C., Hein, J., Nath, B., Murton, B., Galante, D., and Jovane, L. (2018) Integrated geochemical and morphological data provide insights into the genesis of ferromanganese nodules. *Minerals* 8: 488. https://doi.org/10.3390/min8110488.

Chang, L., Harrison, R.J., Zeng, F., Berndt, T.A., Roberts, A.P., Heslop, D., and Zhao, X. (2018) Coupled microbial bloom and oxygenation decline recorded by magnetofossils during the Palaeocene–Eocene thermal maximum. *Nat Commun* 9: 4007. https://doi.org/10.1038/s41467-018-06472-y.

Dong, Y., Li, J., Zhang, W., Zhang, W., Zhao, Y., Xiao, T., *et al*. (2016) The detection of magnetotactic bacteria in deep sea sediments from the East Pacific manganese Nodule Province. *Environ Microbiol Rep* 8: 239– 249. https://doi.org/10.1111/1758-2229.12374.

Dunin-Borkowski, R.E., McCartney, M.R., Frankel, R.B., Bazylinski, D.A., Pósfai, M., and Buseck, P.R. (1998) Magnetic microstructure of magnetotactic bacteria by electron holography. *Science* 282: 1868– 1870. https://doi.org/10.1126/science.282.5395.1868.

Egli, R. (2004) Characterization of individual rock magnetic components by analysis of remanence curves. 3. Bacterial magnetite and natural processes in lakes. *Phys Chem Earth, Parts A/B/C* 29: 869– 884. https://doi.org/10.1016/j.pce.2004.03.010.

Egli, R., Chen, A.P., Winklhofer, M., Kodama, K.P., and Horng, C.S. (2010) Detection of noninteracting single domain particles using first-order reversal curve diagrams. *Geochem Geophys* 11(1): 1– 22. https://doi.org/10.1029/2009gc002916.

Fischer, A., Schmitz, M., Aichmayer, B., Fratzl, P., and Faivre, D. (2011) Structural purity of magnetite nanoparticles in magnetotactic bacteria. *J Roy Soc Interface* 8: 1011– 1018. https://doi.org/10.1098/rsif.2010.0576.

Flies, C.B., Jonkers, H.M., de Beer, D., Bosselmann, K., Böttcher, M.E., and Schüler, D. (2005) Diversity and vertical distribution of magnetotactic bacteria along chemical gradients in freshwater microcosms. *FEMS Microbiol Ecol* 52: 185– 195. https://doi.org/10.1016/j.femsec.2004.11.006.

Frankel, R.B. (2009) The discovery of magnetotactic/magnetosensitive bacteria. *Chinese J Oceanol Limnol* 27: 1– 2. https://doi.org/10.1007/s00343-009-0001-7.

Halbach, P., Marchig, V., and Scherhag, C. (1980) Regional variations in Mn, Ni, Cu, and Co of ferromanganese nodules from a basin in the Southeast Pacific. *Mar Geol* 38: M1– M9 https://doi.org/10.1016/0025-3227(80)90001-8.

Halbach, P., Scherhag, C., Hebisch, U., and Marchig, V. (1981) Geochemical and mineralogical control of different genetic types of deep-sea nodules from the Pacific Ocean. *Miner Deposita* 16: 59– 84. https://doi.org/10.1007/bf00206455.

Harrison, R.J., and Feinberg, J.M. (2008) FORCinel: an improved algorithm for calculating first-order reversal curve distributions using locally weighted regression smoothing. *Geochem Geophys Geosyst* 9(5): 1– 11. https://doi.org/10.1029/2008GC001987

Heslop, D., and Roberts, A.P. (2012) Estimation of significance levels and confidence intervals for first-order reversal curve distributions. *Geochem Geophys Geosyst* 13(5): 1– 12. https://doi.org/10.1029/2012gc004115.

Johnson, D.A. (1972) Ocean-floor erosion in the equatorial pacific. *Geol Soc Am Bull* 83: 3121–3144 https://doi.org/10.1130/0016-7606(1972)83[3121:oeitep]2.0.co;2.

Jovane, L., Florindo, F., Bazylinski, D.A., and Lins, U. (2012) Prismatic magnetite magnetosomes from cultivated M agnetovibrio blakemorei strain MV-1: a magnetic fingerprint in marine sediments? *Environ Microbiol Rep* 4: 664– 668. https://doi.org/10.1111/1758-2229.12000.

Kopp, R.E., and Kirschvink, J.L. (2008) The identification and biogeochemical interpretation of fossil magnetotactic bacteria. *Earth-Sci Rev* 86: 42– 61. https://doi.org/10.1016/j.earscirev.2007.08.001.

Kruiver, P.P., Dekkers, M.J., and Heslop, D. (2001) Quantification of magnetic coercivity components by the analysis of acquisition curves of isothermal remanent magnetisation. *Earth Planet Sci Lett* 189: 269– 276 https://doi.org/10.1016/s0012-821x(01)00367-3.

Lefèvre, C.T., and Bazylinski, D.A. (2013) Ecology, diversity, and evolution of magnetotactic bacteria. *Microbiol Mol Biol Rev* 77: 497– 526. https://doi.org/10.1128/mmbr.00021-13.

Lefèvre, C.T., and Wu, L.F. (2013) Evolution of the bacterial organelle responsible for magnetotaxis. *Trends Microbiol* 21: 534– 543. https://doi.org/10.1016/j.tim.2013.07.005.

Lowrie, W. (1990) Identification of ferromagnetic minerals in a rock by coercivity and unblocking temperature properties. *Geophys Res Lett* 17: 159– 162.

Mewes, K., Mogollón, J.M., Picard, A., Rühlemann, C., Kuhn, T., Nöthen, K., and Kasten, S. (2014) Impact of depositional and biogeochemical processes on small scale variations in nodule abundance in the Clarion-Clipperton fracture zone. *Deep-Sea Res I Oceanogr Res Pap* 91: 125–141. https://doi.org/10.1016/j.dsr.2014.06.001.

Moskowitz, B.M., Frankel, R.B., and Bazylinski, D.A. (1993) Rock magnetic criteria for the detection of biogenic magnetite. *Earth Planet Sci Lett* 120: 283– 300. https://doi.org/10.1016/0012-821x(93)90245-5.

Oda, H., Nakasato, Y., and Usui, A. (2018) Characterization of marine ferromanganese crust from the Pacific using residues of selective chemical leaching: identification of fossil magnetotactic bacteria with FE-SEM and rock magnetic methods. *Earth Planets Space* 70: 165.

Petermann, H., and Bleil, U. (1993) Detection of live magnetotactic bacteria in South Atlantic deep-sea sediments. *Earth Planet Sci Lett* 117: 223– 228. https://doi.org/10.1016/0012-821x(93)90128-v.

Pósfai, M., Lefèvre, C., Trubitsyn, D., Bazylinski, D.A., and Frankel, R. (2013) Phylogenetic significance of composition and crystal morphology of magnetosome minerals. *Front Microbiol* 4: 344.

Roberts, A.P., Chang, L., Heslop, D., Florindo, F., and Larrasoaña, J.C. (2012) Searching for single domain magnetite in the "pseudo-single-domain" sedimentary haystack: implications of biogenic magnetite preservation for sediment magnetism and relative paleointensity determinations. *J Geophys Res Solid Earth* 117(B8): 1– 26. https://doi.org/10.1029/2012jb009412.

Roberts, A.P., Florindo, F., Villa, G., Chang, L., Jovane, L., Bohaty, S.M., *et al*. (2011) Magnetotactic bacterial abundance in pelagic marine environments is limited by organic carbon flux and availability of dissolved iron. *Earth Planet Sci Lett* 310: 441– 452. https://doi.org/10.1016/j.epsl.2011.08.011.

Roberts, A.P., Heslop, D., Zhao, X., and Pike, C.R. (2014) Understanding fine magnetic particle systems through use of first-order reversal curve diagrams. *Rev Geophys* 52: 557– 602. https://doi.org/10.1002/2014rg000462.

Roberts, A.P., Pike, C.R., and Verosub, K.L. (2000) First-order reversal curve diagrams: a new tool for characterizing the magnetic properties of natural samples. *J Geophys Res Solid Earth* 105: 28461– 28475. https://doi.org/10.1029/2000jb900326.

Rodelli, D., Jovane, L., Roberts, A.P., Cypriano, J., Abreu, F., and Lins, U. (2018) Fingerprints of partial oxidation of biogenic magnetite from cultivated and natural marine magnetotactic bacteria using synchrotron radiation. *Environ Microbiol Rep* 10: 337– 343. https://doi.org/10.1111/1758-2229.12644.

Savian, J.F., Jovane, L., Frontalini, F., Trindade, R.I., Coccioni, R., Bohaty, S.M., *et al*. (2014) Enhanced primary productivity and magnetotactic bacterial production in response to middle Eocene warming in the Neo-Tethys Ocean. *Palaeogeogr Palaeoclimatol Palaeoecol* 414: 32–45. https://doi.org/10.1016/j.palaeo.2014.08.009.

Savian, J.F., Jovane, L., Giorgioni, M., Iacoviello, F., Rodelli, D., Roberts, A.P., *et al*. (2016) Environmental magnetic implications of magnetofossil occurrence during the Middle Eocene Climatic Optimum (MECO) in pelagic sediments from the equatorial Indian Ocean. *PalaeogeogrPalaeoclimatol Palaeoecol* 441: 212– 222. https://doi.org/10.1016/j.palaeo.2015.06.029.

Schumann, D., Raub, T.D., Kopp, R.E., Guerquin-Kern, J.L., Wu, T.D., Rouiller, I., *et al*. (2008) Gigantism in unique biogenic magnetite at the Paleocene–Eocene thermal maximum. *Proc Natl Acad Sci* 105: 17648– 17653. https://doi.org/10.1073/pnas.0803634105.

Stolz, J.F., Lovley, D.R., and Haggerty, S.E. (1990) Biogenic magnetite and the magnetization of sediments. *J Geophys Res Solid Earth* 95: 4355– 4361. https://doi.org/10.1029/jb095ib04p04355.

Stramma, L., Johnson, G.C., Firing, E., and Schmidtko, S. (2010) Eastern Pacific oxygen minimum zones: supply paths and multidecadal changes. *J Geophys Res Oceans* 115(C9): 1–12. https://doi.org/10.1029/2009jc005976.

Strehlau, J.H., Hegner, L.A., Strauss, B.E., Feinberg, J.M., and Penn, R.L. (2014) Simple and efficient separation of magnetic minerals from speleothems and other carbonates. *J Sediment Res* 84: 1096– 1106.

Tully, B.J., and Heidelberg, J.F. (2013) Microbial communities associated with ferromanganese nodules and the surrounding sediments. *Front Microbiol* 4: 161. https://doi.org/10.3389/fmicb.2013.00161.

Vali, H., Weiss, B., Li, Y.L., Sears, S.K., Kim, S.S., Kirschvink, J.L., and Zhang, C.L. (2004) Formation of tabular single-domain magnetite induced by Geobacter metallireducens GS-15. *Proc Natl Acad Sci* 101: 16121– 16126. https://doi.org/10.1073/pnas.0404040101.

Wang, X.H., Gan, L., and Müller, W.E. (2009a) Contribution of biomineralization during growth of polymetallic nodules and ferromanganese crusts from the Pacific Ocean. *Front Mater Sci China* 3: 109– 123. https://doi.org/10.1007/s11706-009-0033-0.

Wang, X., Schloßmacher, U., Wiens, M., Schröder, H.C., and Müller, W.E. (2009b) Biogenic origin of polymetallic nodules from the Clarion-Clipperton zone in the eastern Pacific Ocean: electron microscopic and EDX evidence. *Marine Biotechnol* 11: 99. https://doi.org/10.1007/s10126-008-9124-7.

Wegorzewski, A.V., and Kuhn, T. (2014) The influence of suboxic diagenesis on the formation of manganese nodules in the Clarion Clipperton nodule belt of the Pacific Ocean. *Mar Geol* 357: 123– 138. https://doi.org/10.1016/j.margeo.2014.07.004.

Yamazaki, T. (2008) Magnetostatic interactions in deep-sea sediments inferred from first-order reversal curve diagrams: implications for relative paleointensity normalization. *Geochem Geophys Geosyst* 9(2): 1– 12. https://doi.org/10.1029/2007gc001797.

Zheng, Y., Geen, A., Anderson, R.F., Gardner, J.V., and Dean, W.E. (2000) Intensification of the Northeast Pacific oxygen minimum zone during the Bølling-Allerød warm period. *Paleoceanogr Paleoclimatol* 15: 528– 536. https://doi.org/10.1029/1999pa000473.

Supplementary material

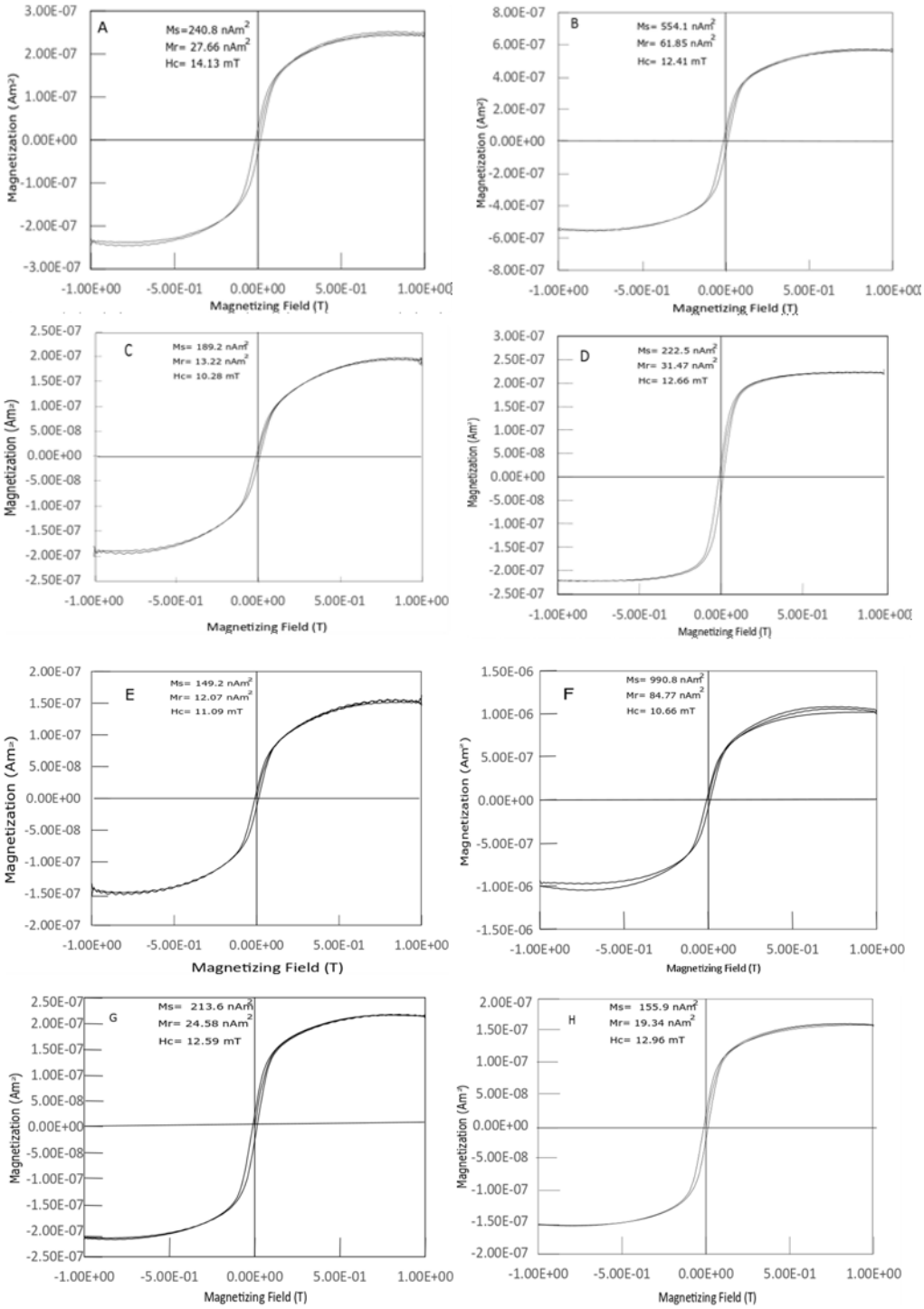

Fig. S1. Hysterisis cycles; Hysterisis cycles for all subsamples i.e, A, B, C, D, E, F G and H.

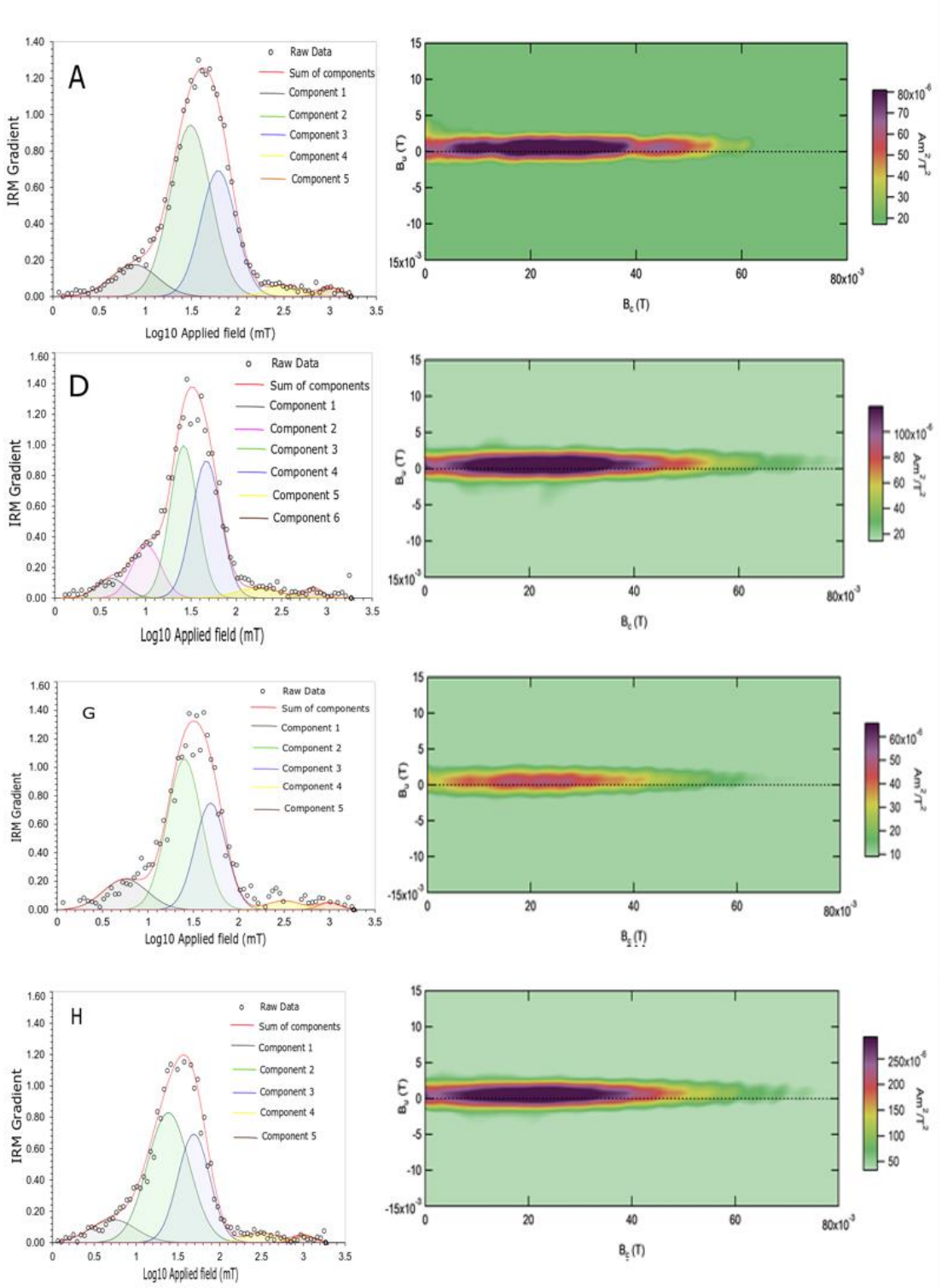

Fig.S2. Decomposition of Isothermal Remanent Magnetization (IRM) curves and First Order Reversal curves (FORCs); Left: IRM acquisition curves for subsamples A, D, G and H. Right: FORCs for the same subsamples.

3 A MAGNETIC AND GEOCHEMICAL APPROACH TO FERROMANGANESE CRUSTS FROM THE ATLANTIC OCEAN (CHAPTER 2)

Manuscript to be submitted to *Geochemistry, Geophysics, Geosystems*

Muhammad Bin Hassan[1,2], Andrea Koschinsky[2,3], Gabriel Lucas Xavier da Silva[4], Rafaela Cardoso Dantas[1,5], Thomas Kuhn[6], Christian Millo[1], Gunther Kletetschka[7,8], Luigi Jovane[1]

[1]Instituto Oceanográfico, Universidade de São Paulo, São Paulo, Brazil
[2]Department of Physics and Earth Sciences, Constructor University, Bremen, Germany
[3]Center for Marine Environmental Sciences (MARUM), University of Bremen, Bremen, Germany
[4]Tokyo Institute of Technology, Japan
[5]Instituto de Geociências - Universidade de São Paulo, São Paulo, Brazil
[6]Federal Institute for Geosciences and Natural Resources (BGR), Hannover, Germany
[7]Institute of Hydrogeology, Engineering Geology and Applied Geophysics, Faculty of Science, Charles University, Prague Czech Republic
[8]Geophysical Institute, University of Alaska - Fairbanks, AK, United States of America

Abstract

Ferromanganese (FeMn) crusts are Fe and Mn oxides that typically form on deep-sea elevations by deposition of colloids from seawater. These mineral deposits are considered a source of critical metals and rare earth elements. Besides their potential economic value, FeMn crusts are extremely relevant in ocean science, since their very slow growth rates result in long-term paleoenvironmental and palaeoceanographic records. In this study, we applied geochemical, mineralogical, and magnetic analyses to unravel paleoenvironmental changes at two locations on opposite sides of the Atlantic Ocean, the Rio Grande Rise (RGR) in the SW Atlantic and the Tropic Seamount (TS) in the NE Atlantic. Our results show that the occurrence of amorphous (non-crystalline) Fe oxyhydroxides and the absence of Fe oxides in hydrogenetic, non-phosphatized FeMn crusts prevented the development of primary remanent magnetization. In contrast, phosphatized FeMn crusts may have contained a remanent magnetic signal. Phosphatization resulted from increased primary productivity and occurred at different stages during the growth of the FeMn crusts, leading to suboxic conditions and partial dissolution of pre-existing, remanence-carrying magnetic minerals. Carbonate Fluorapatite (CFA) accumulation in the phosphatized layers of FeMn crusts replaced Fe and Mn, decreasing their

magnetic content. Thus, magnetic variations do not reflect a primary magnetization but rather result from geochemical alterations. The loss of primary magnetization may hamper the use of FeMn deposits for magnetostratigraphic purposes.

3.1 Introduction

Deep-sea ferromanganese (FeMn) deposits represent the most significant, yet least explored, asset of 'E-tech' elements on our planet (Hein et al., 2003; 2010; 2012). These deposits include manganese-copper-nickel enriched nodules and cobalt-platinum, and heavy Rare Earth Elements (HREE) enriched crusts (Hein et al., 2003). FeMn deposits are mainly composed of Fe-oxyhydroxides and Mn oxides accreting at rates of a few millimetres per million year (mm/My) over tens of millions of years, thereby accumulating significant amounts of trace elements from seawater (e.g., Koschinsky and Hein, 2003).

FeMn crusts typically form on hard-rock substrates, on the flanks and summits of seamounts, ridges, and plateaus where the substrate has been swept clean of sediments for millions of years (Hein et al., 2000). They grow by chemical precipitation from seawater at water depths below the oxygen minimum zone (typically deeper than ~700 m) throughout the ocean basins. The Pacific Ocean contains the largest amount of FeMn crusts because there is the largest number of seamounts. The highest abundance of FeMn crusts is in the central and western equatorial Pacific (from 0˚to 20˚N), in the area referred to as the Pacific Prime Crust Zone (PPCZ). FeMn crusts are also found in the Atlantic and Indian Oceans and in the polar seas, where their mapping is still largely incomplete (Konstantinova et al., 2017). The typical average thickness of FeMn crust varies from 2–4 cm to >12 cm (Usui et al., 2007), with a general correlation between the age of the seamount hosting FeMn crusts and crust thickness (Usui and Someya, 1997).

Atlantic crusts differ in their chemical composition from Pacific crusts, due to a stronger content of terrestrial components in the Atlantic (Koschinsky et al., 1995; Hein et al., 2013).

Given their extremely low growth rate, FeMn crusts conceal clues about the chemistry of the past ocean and are ideal archives for palaeoceanographic research (Koschinsky and Hein, 2017, Josso et al., 2019). Previous studies have shown that the vertical variability of the distribution of trace elements in the FeMn crust provides clues about the temporal variability of ocean circulation patterns, and continental erosion rates (Frank et al., 1999; Bau and Koschinsky, 2006; Yi et al., 2023) and redox state in the global ocean (Hein et al., 2003). Moreover, a variety of elements concentrated in FeMn crusts, such as Co, Ti, Mn, Ni, Pt, Zr, Nb, Te, Bi, W, Th, Ni, Cu, Co, Mn and Mo, are considered critical for the development of carbon-free energy

production (Marino et al., 2018). This aspect is also raising concern about the adverse consequence of future deep-sea mining on marine ecosystems, which makes FeMn deposits particularly interesting to both science and society.

Recently, Josso et al. (2019) and Benites et al. (2020) described the genesis of FeMn crusts at two locations on opposite sides of the Atlantic Ocean, respectively the Tropic Seamount (TS, NE Atlantic) and the Rio Grande Rise (RGR, SW Atlantic). In both locations, FeMn crusts underwent extensive diagenetic changes resulting in the formation of Carbonate Fluorapatite (CFA) under suboxic conditions (Marino et al., 2017; Josso et al., 2019; Benites et al., 2020; Sousa et al., 2021). The oldest layers of FeMn crusts from the RGR underwent phosphatization during the Miocene (Benites et al., 2020), while in the TS crusts phosphatization started 38 My ago (Josso et al., 2019).

Magnetic minerals are iron-bearing minerals that occur in nature as oxides, hydroxides, and sulphides. These minerals are sensitive to oxidative and reductive environmental conditions (Liu et al., 2012; Roberts, 2015). Their precipitation is chemically controlled by the concentration of Fe, pH, and redox potential (Emerson et al., 2012). The process of microbial magnetite mineralization in FeMn crusts is still poorly documented. Magnetic analyses on FeMn crusts and nodules from the Pacific Ocean and the China Sea indicated that the primary source of remanent magnetization can be linked to magnetotactic bacteria (Oda et al., 2018; Hassan et al., 2020; Yuan et al., 2020). Although magnetite biomineralization has been reported for hydrogenetic FeMn deposits, most of the Fe-bearing phase is nanometric, X-ray amorphous Fe hydroxide and poorly crystalline Fe-bearing vernadite (Guan et al., 2017; Bogdanova et al., 2008; Hein and Koschinsky, 2014; Jiang et al., 2021), which can also precipitate abiotically.

Several studies have presented magnetostratigraphic dating of FeMn crusts from the Pacific Ocean and the China Sea based on magnetic scanning techniques, as well as traditional cryogenic magnetic methods (Joshima and Usui, 1998; Oda et al., 2011; Yuan et al., 2017; Usui et al., 2017; Noguchi et al., 2017a, 2017b; Yi et al., 2020; Yi et al., 2023; Oda et al., 2023), whereas magnetic studies on FeMn crusts from the Atlantic Ocean are scarce. In this study, we compare the magnetic properties and geochemical composition of phosphatized and non-phosphatized hydrogenetic FeMn crusts collected in the RGR and in the TS to document the primary source of magnetization and the effect of phosphatization on the magnetic properties of FeMn crusts.

3.2 Study areas

3.2.1 Rio Grande Rise

The Rio Grande Rise (RGR) is located approximately 1,300km east of the Brazilian coastline and is separated by the Vema Channel from São Paulo Plateau (SPP)(Fig.1). The rise is a shallow plateau with a water depth of 800m separated by a rift structure which is over 1,400m deep and 900km long that splits the plateau into two parts, the Western Rio Grande Rise (WRGR) and the Eastern Rio Grande Rise (ERGR) (Camboa and Rabinowitz, 1984 (Fig.1). The Great Rift is 24km wide and has deep troughs with vertical sides like a canyon. The RGR summit is located above the OMZ, which is ventilated by oxygenated Antarctic Intermediate Water (AAIW) and less oxygenated South Atlantic Mode Water (SAMW) (Sarmiento et al., 2004; Ayers and Strutton, 2013).

The basaltic walls are up to 600m in height. The RGR is a large igneous province of the Cretaceous age. Its origin is still controversial and debatable (Barker, 1983; Camboa and Rabinowitz, 1984).

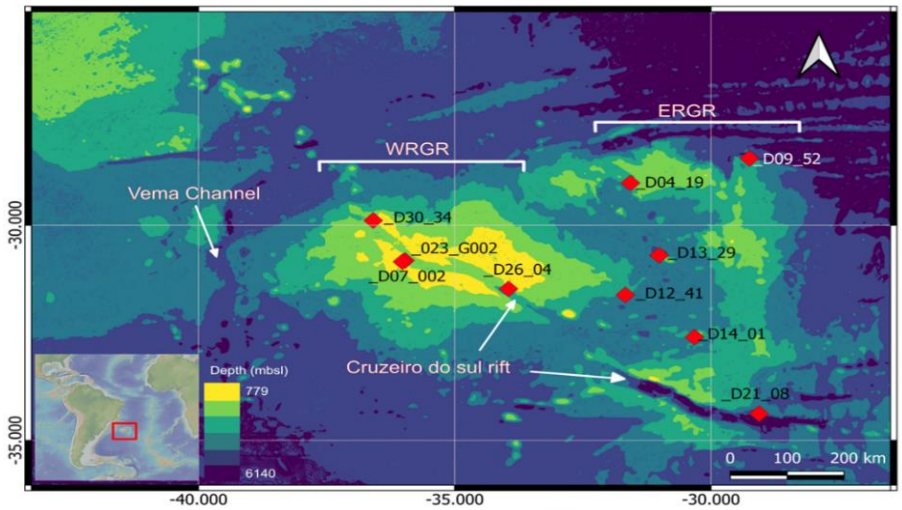

Fig. 1. Bathymetric map of RGR (Source GEBCO) with location of the FeMn crust samples (Table 1)

3.2.2 Tropic Seamount

The Tropic Seamount is a part of the Canary Island Seamount Province (CISP) and is at the southwestern edge of CISP (Marino et al., 2018, 2019). TS has an area of 770 km^2. It is an isolated northeastern Atlantic volcanic edifice. It is located 400 km from West Africa's passive continental margin, halfway between the Canary Islands and the Cape Verde Islands (Fig. 2). The seamount rises to a depth of 950 mbsl from the abyssal plain at 4100 mbsl where it has a flat diamond-shaped top (Fig. 2). The flanks are dominated by gullies and landslide scars separated by four spurs that radiate from the summit, exposing volcanic rocks covered by loose

sediments (Palomino et al., 2016). The CISP region lies below the Oxygen Minimum Zone (OMZ) which extends from 100 to 700 m water depth with lowest oxygen contents between 400 and 500 m (Brandt et al., 2010, 2012).

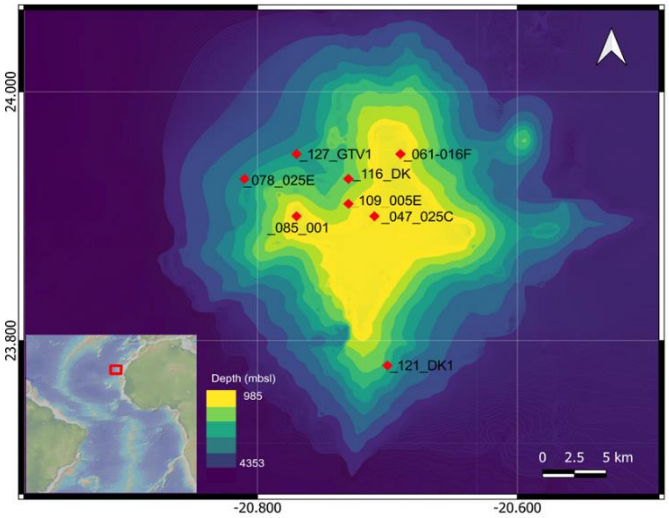

Fig.2: Bathymetric map of TS (Source GEBCO) with location of the FeMn crust samples (Table 1)

The history of investigations on FeMn crusts from TS goes back to the 1990s. Koschinsky et al. (1996) determined an age of 12.3 Ma and an average growth rate of 3 mm/Ma based on $^{10}Be/^{9}Be$ dating of a 38 mm thick crust sample. By contrast, using the Co chronometer model by Manheim and Lane-Bostwick (1988), Marino et al. (2017) and (2018) calculated bulk growth rates of 1.2–1.8 mm / Ma and growth rates of 0.54–0.9 mm / Ma. Recently Josso et al. (2019) presented an age model for FeMn crusts from TS. Their findings from the composite age projections show that there were favorable conditions from at least the Late Cretaceous (75 ± 2 Ma) for the growth of hydrogenetic FeMn deposits on the TS.

3.3 Materials and Methods

The samples used in this study were collected during different oceanographic expeditions. FeMn crust samples from TS were collected using the grab arm of the Remotely Operated Vehicle (ROV) *Isis* of the National Oceanography Centre (Southampton, UK) during expedition JC142 on board HMRS *James Cook* in December 2016 (Josso et al., 2019). FeMn crusts samples from RGR were collected by dredging during expeditions RGR1 and DY094 on board the RV *Alpha Crucis* (Instituto Oceanografico, University of Sao Paulo, Brazil) (Jovane et al., 2019) and HMRS *Discovery* (Benites et al., 2022) in February and October 2018,

respectively. During the DY094 expedition, some FeMn crust samples were collected using the grab arm of the ROV *HyBis*. FeMn crusts from the western region (Fig. 1) of RGR were dredged during the NBP1808 cruise on board the RV *Nathaniel B. Palmer* from October 3rd to December 12th, 2018. The 10 samples from this region that were used in this study were provided by the Marine and Geology Repository, Oregon State University, USA (Davidson et al., 2022).

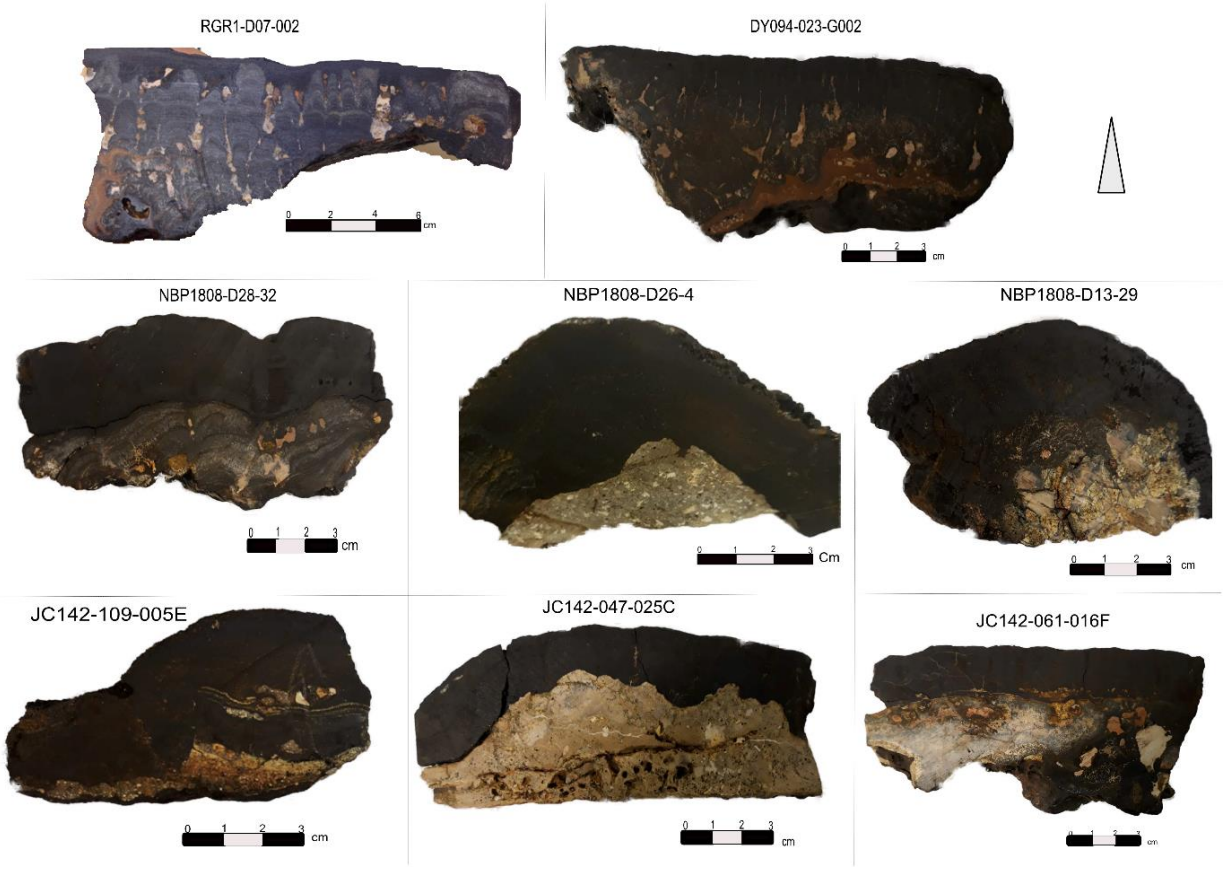

Selected samples (Fig.1 and 2) from the above-mentioned regions are listed in Table 1.

Fig.3: Hand specimens of FeMn crust samples from RGR and TS selected for this study (details in Table 1)

Phosphatized and non-phosphatized hydrogenetic layers of the crust samples were sub-sampled to study the geochemical, mineralogical, and magnetic properties using different analytical techniques, as detailed below.

Table.1: List of FeMn crust samples from RGR and TS; **Bold** shows the samples used for the continuous magnetic measurements.

Sr. number	Sample name	Lat	Long	Depth (m)	Location
1	NBP1808-D21-14	-34.38	-29.06	5218	Rio Grande Rise
2	NBP1808-D4-19	-29.02	-31.57	2735	Rio Grande Rise
3	NBP1808-D21-12	-34.38	-29.06	5218	Rio Grande Rise
4	NBP1808-D14-1	-32.60	-30.32	2634	Rio Grande Rise
5	NBP1808-D21-08	-34.38	-29.06	5218	Rio Grande Rise
6	NBP1808-D12-41	-31.62	-31.67	4076	Rio Grande Rise
7	NBP1808-D13-24	-30.70	-31.01	2772	Rio Grande Rise
8	NBP1808-D9-52	-28.45	-29.25	4592	Rio Grande Rise
9	**DY094-023-G002**	**-30.82**	**-35.97**	**786**	**Rio Grande Rise**
10	NBP1808-13-29	-30.70	-31.01	2772	Rio Grande Rise
11	NBP1808-26-04	-31.48	-33.95	2190	Rio Grande Rise
12	**RGR1-D07-002**	**-30.85**	**-36.02**	**684**	**Rio Grande Rise**
13	NBP1808-D30-34	-29.89	-36.59	2008	Rio Grande Rise
14	S083-116-DK	23.91	-20.73	1484	Tropic Seamount
15	S083-127-GTV1	23.95	-20.77	1088	Tropic Seamount
16	S083-121-DK1	23.78	-20.70	2377	Tropic Seamount
17	JC142-047-025C	23.90	-20.71	999	Tropic Seamount
18	JC142-061-016F	23.95	-20.69	1122	Tropic Seamount
19	JC142-109-005E	42.87	-20.73	3760	Tropic Seamount
20	**JC142-085-001**	**23.90**	**-20.77**	**1130**	**Tropic Seamount**
21	**JC142-078-025E**	**23.93**	**-20.81**	**2803**	**Tropic Seamount**

3.3.1 Petrography, Geochemistry and Mineralogy

3.3.1.1 Scanning Electron Microscopy (SEM)

SEM was performed on grain samples to understand the relationship between the texture, color and morphological features of different crust layers (i.e., fresh hydrogenetic layers and phosphatized layers) with the general grain chemistry.

The thin sections (30 μm) and slides (~1 cm) were also subjected to analyse the morphological characteristics of FeMn crusts under the MLA 650F Quanta FEG SEM (FEI Company). Scanning Electron Microscopy (SEM) coupled with EDS was performed at BGR, the Federal Institute for Geosciences and Natural Resources (BGR), Hannover, Germany. A high vacuum of 25 kV, a Work Distance of 10-14 mm, a spot size of 2.0 to 6.0 μm, and magnifications from 100x to 2500x were used to identify different features on the FeMn crust samples.

3.3.1.2 Inductively Coupled Plasma Mass Spectrometry (ICP-MS) and Inductively Coupled Plasma Optical Emission Spectrometry (ICP-OES)

Major and minor elements were analyzed by using a Spectro Ciros Vision SOP ICP-OES (Inductively coupled plasma atomic emission spectroscopy) and trace elements (including the rare earth elements and high field strength elements such as Zr, Hf, Nb) were measured by Perkin_Elmer NexION 350X quadrupole ICP-MS (Inductively coupled plasma mass spectrometry) in the geochemistry laboratory at Constructor University in Bremen, Germany. All samples were carefully drilled with a micro-drill, powdered in an agate pan mill and dried at 105°C for 24 h. Immediately after drying, 0.05 mg of each sample was digested with HCl, HNO_3 and HF in a ratio of 3:1:1 ml. Samples in the acid mixture are heated to 225°C for 12 hours in closed vessels that were later opened and kept at 180°C for acid evaporation. Digested samples were stored in 0.5 M HNO_3. Samples were diluted for Mn, Fe, Cu, Al, K, Ca, Mg, Na, P, V and Zn measurement using ICP-OES. Determination of Li, Sc, Ti, Co, Ni, Tl, Rb, Sr, Y, Zr, Nb, Mo, Te, Cs, Ba, REE, Hf, Ta, W, Pt, Pb, Th and U was performed in diluted samples using ICP-MS. Certified Reference Materials (CRM) JMn-1 and Fe-Mn1 were used for precision which was better than ±90% for most elements. To understand the oxygenation conditions for crust growth and phosphatization, REY anomalies for the phosphatized and non-phosphatized crusts were separately plotted and normalized by Post-Archean Australian Shale (PAAS).

3.3.1.3 X-ray Diffraction

~1 g of powdered and oven-dried phosphatized and non-phosphatized layers of selected samples from RGR and TS were used to perform X-Ray Diffraction (XRD) measurements. Bulk samples were measured using PANalytical X'Pert PRO MPD diffractometer Cu-kα radiation with 40kV and 40mA at the Federal Institute for Geosciences and Natural Resources (BGR), Hannover, Germany. The diffractometer contains a variable divergence slit and the Scientific X'Celerator detector. Samples were measured over 5º-85º with a step size of 0.0334º 2θ and a measuring time of 200s/step. The results were processed using High Score Plus Software.

3.3.2 Magnetic Measurements

3.3.2.1 Transmission Electron Microscopy and Mössbauer Spectroscopy

The representative crust samples weighing 10 g each were gently crushed, powdered and passed through the sieve of 150 μm. To extract the magnetic particles from the powdered samples, the samples were mixed with acetate buffer (pH 4.0) according to Strehlau et al. (2014). Samples were maintained under constant agitation overnight. Magnetic concentration using a magnet and washing steps with MilliQ were performed before sample deposition in formvar–carbon-coated grids for Transmission Electron Microscopy. Samples were observed on an FEI Tecnai Spirit (FEI Company) at 120 kV at the Instituto de Microbiologia Paulo de Góes, Universidade Federal do Rio de Janeiro.

Mössbauer spectroscopy can distinguish between ferrous and ferric iron. Magnetic particles extracted from the selected samples were also subjected to Mössbauer spectroscopy, which was carried out at the Instituto de Física, Universidade de São Paulo. Mössbauer spectroscopy was performed at room temperature using a commercial spectrometer (Wissel- Mössbauer spectrometer) equipped with a ^{57}Co source, operating in constant acceleration mode with a sampling velocity in the range of ±10 mm/s. The NORMOS software package was used to fit the obtained spectra curve by minimizing the chi-squared parameter (X^2). The spectra were calibrated using metallic iron as the standard.

3.3.2.2 Magnetic Scanning

Magnetic scanning was performed on 1 cm thick slides of 4 selected samples along the growth direction of the crusts by using Hall probe magnetic microscope at the Department of Geophysics at Charles University, Prague, Czech Republic. Among these 4 samples, two samples, one from RGR (RGR1-D07-002) and one from TS (JC142-085-001) were the same samples studied by Benites et al. (2020) and Josso et al. (2019). The vertical component of the magnetic field was measured at a sensor-to-sample distance of 0.1mm with a scanning interval of 80 μm. The scanning was repeated 100 times along the same profile. Another additional parallel profile was also measured to compare the magnetic signals. PCA from both lines was generated and plotted with the arithmetic mean of the magnetic field. The background signal was measured without the sample which was later subtracted from the signal obtained from the crust sample. Specifications of the Hall probe magnetic scanner are detailed in Kletetschka et al. (2013).

3.3.2.3 Rock Magnetism and Paleomagnetism

Rock magnetic measurements [hysteresis cycles, First Order Reversal Curves (FORCs) and thermomagnetic curves] were performed at the CORE Lab of the IO-USP. An Alternating Gradient magnetometer (AGM) Micromag 3900 from Lake Shore was used to measure the hysteresis cycles and FORCs of the subsamples collected along the FeMn crusts. Hysteresis parameters such as magnetic saturation (Ms), remanence of magnetic saturation (Mrs) and magnetic coercivity (Hc) were obtained by applying a maximum field of 1 Tesla. FORCs were produced by applying a maximum field of 1 T, with an average time of 150 ms on 297 curves. The FORC diagrams were processed with the software "Forcot" and varying smoothing factors (SF) were applied to visualize FORC fingerprints for the measured samples (Berndt et al., 2019).

0.5 g of powdered crust subsamples were subjected to identify the magnetic minerals based on Curie temperature. Thermomagnetic curves are used to understand the Curie (or Neel) temperature of the magnetic minerals where magnetic susceptibility is measured at regular intervals by consecutively heating the samples. Magnetic susceptibility *vs* temperature curves were obtained by progressive heating and cooling in the Argon environment. Selected burnt samples were reanalyzed to understand newly formed magnetic minerals in the controlled environment. The Kappabridge MFK1 (AGICO) was used to perform the measurements. Bulk data were processed and plotted by the Cureval software provided by AGICO.

Roughly 2 mm thick slices of four FeMn crusts shown in Table 1 were cut by a cutting blade of thickness less than 0.4 mm along the growth direction of FeMn crusts as described by Yuan et al. (2017). The magnetic susceptibility of the thinly sliced samples was measured. Thinly sliced samples were also subjected to measure Natural Remanent magnetization (NRM). NRM was measured by using a 2G Enterprises Long Core Squid Magnetometer in a shielded room at the Paleomagnetic lab of the Instituto de Astronomia e Geofísica (IAG) of the University of São Paulo. Stepwise Alternating Field (AF) demagnetization of 5, 10, 15, 20, 25, 30, 40, 50, 60, 70, 80, 90 and 100 mT was employed to remove the secondary magnetic components. PuffinPlot software provided by Lurcock and Wilson (2012) was used to display the demagnetization data. PCA (Principal Component Analysis) was performed to recognize the primary magnetic component (Characteristic Remanent Magnetization ChRM) (Kirschvink, 1980). Samples with the Mean Planar Deviation Angle (MAD) greater than 12º were considered unreliable.

3.3 **Results**

3.3.1 ***Petrography, Geochemistry and Mineralogy***

3.4.1.1 Petrography and texture

Both in the RGR and in the TS samples, the hydrogenetic/non-phosphatized layers of the FeMn crust consist of amorphous Fe oxyhydroxide phases. SEM observation of thin sections revealed alternate dendritic and botryoidal textures (Fig. 5 A and B). Non-phosphatized parts of FeMn crusts from TS exhibit parallel botryoidal texture while the crusts from RGR show dendritic texture (Fig. 5). The phosphatized crusts are made up mainly of carbonate fluorapatite (CFA) (Fig. 5 A and B). In crusts from TS the CFA accumulation occurs in fractures perpendicular to the growth direction, whereas in crusts from RGR massive and irregular accumulation of CFA occurs in pore spaces. SEM-EDS mapping of Fe, Mn, P and Ca shows a co-occurrence of the Fe and Mn phases, whereas the abundance of CFA (shown by a high abundance of P and Ca) is negatively correlated with the abundance of Fe and Mn. This suggests that Fe and Mn phases are replaced by CFA in phosphatized crusts from both regions. Massive ironstones are abundant and only in diagenetically altered parts of FeMn crusts from RGR (Benites et al., 2022) (Fig. 5c). Sample RGR1-D07-002 (Fig. 5B (g and h)) shows a Fe-rich matrix containing smooth and rounded particles, likely cosmic spherules. Cosmic spherules have been previously reported in FeMn crusts (Halbach et al., 1989; Oda et al., 2018; Savelyev et al., 2022). Samples from both regions also contain volcanic breccia cemented by CFA in the phosphatized layers of the crusts, which have also been previously reported (Varentsov et al., 1991; Marino et al., 2019; Benites et al., 2022; Staszak et al., 2022).

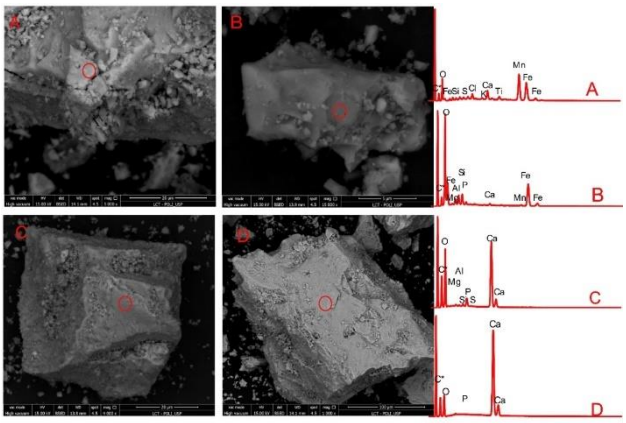

Fig.4: SEM images of powdered samples of FeMn crusts. Circles indicate positions of EDS spectra (on the right). A- FeMn phase from the non-phosphatized RGR crust sample RGR1-D07-002, B- FeMn phase from the non-phosphatized TS crust sample JC142-085-00, C- CFA phase from phosphatized RGR crust sample RGR1-D07-002, D- CFA phase from phosphatized TS crust sample JC142-085-001. Non-phosphatized layers are dominated by Fe and Mn oxides whereas phosphatized layers are rich in Ca and P, indicating the presence of CFA.

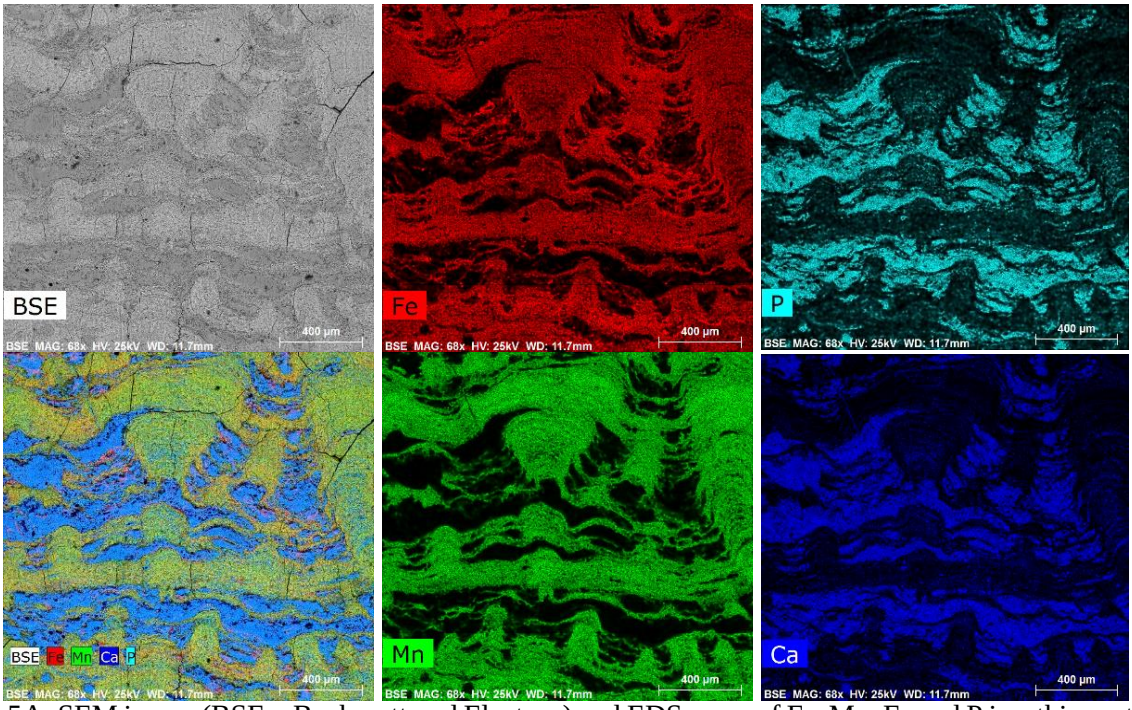

Fig.5A: SEM image (BSE = Backscattered Electron) and EDS maps of Fe, Mn, Fe and P in a thin section of FeMn crust sample DY094-023-G002. Fe and Mn-rich layers are depleted in P and Ca, suggesting the replacement of FeMn layers by CFA.

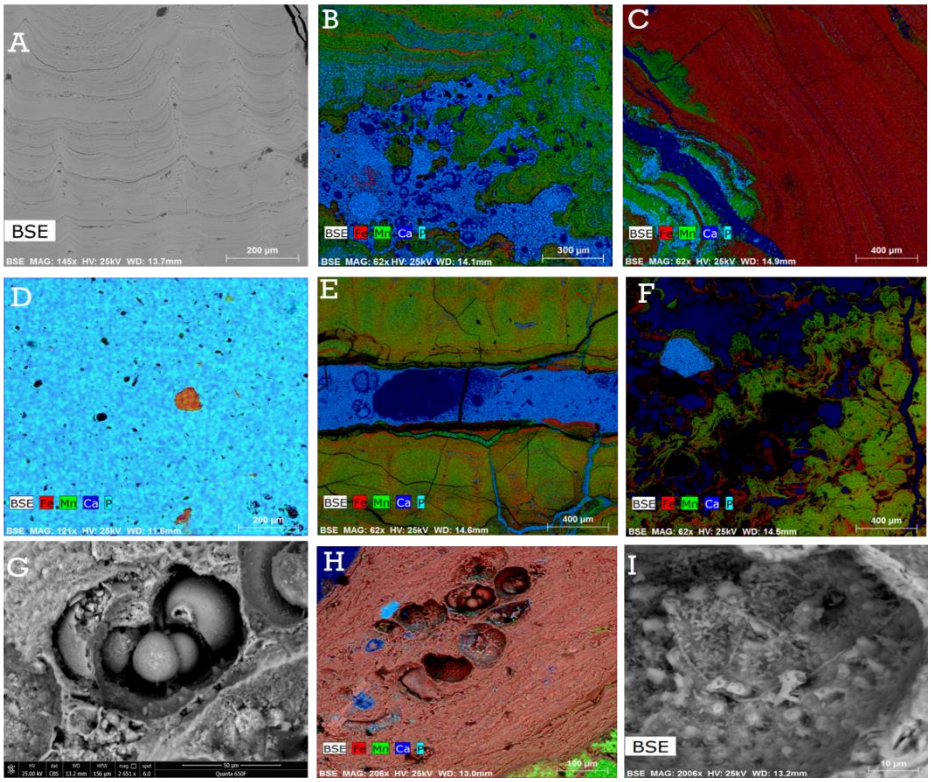

Fig.5B: SEM images of FeMn crusts: A-C: DY094-023-G002 (RGR), A- Backscatter Electron (BSE) image of typical hydrogenetic FeMn layers, B- EDS elemental mapping of the phosphatized crust showing the dendritic texture filled with foraminifera enriched CFA, C- EDS elemental mapping of the phosphatized crust showing massive ironstone texture (dark red); D-F: JC142-085-001 (TS), D- Fe-rich grain being replaced by CFA, E- Fracture filled by CFA, F- CFA filling pore space; G-I: RGR1-D07-002 (RGR), G- BSE image of smooth and circular cosmic spherules inside a Fe-rich matrix, H- EDS elemental mapping of the spherule-rich area, I- Bacterial mats with CFA crystals.

3.4.1.2 Geochemistry

ICP-OES data were used to build ternary and binary diagrams from Bonatti et al. (1972) and Dymond et al. (1984). Both diagrams are based on the concentration of Fe, Mn, Co, Ni, and Cu in each subsample (non-phosphatized or phosphatized). The data plotted in both diagrams suggest that all the studied crusts from both regions formed hydrogenetically (Fig. 6).

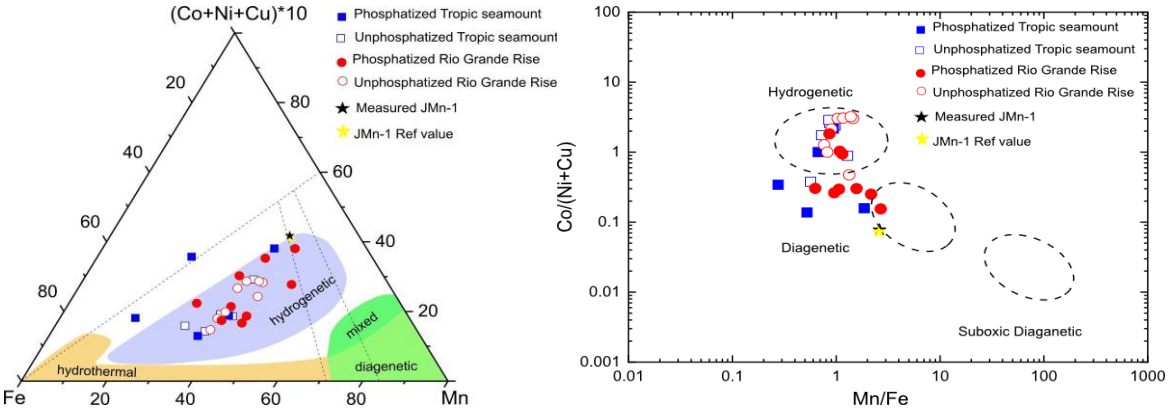

Fig.6: Ternary and binary diagrams: Left - The ternary diagram by Bonatti et al., 1972 and Right - Binary diagram by Dymond et al., 1984. Both diagrams classify the studied samples as hydrogenetic FeMn crusts. JMn-1 indicates the certified reference material (CRM) prepared by the Geological Survey of Japan (GSJ) (Terashima et al., 1995).

ICP-MS data (Fig. 7 and Fig. 8) separate non-phosphatized from phosphatized crusts, as positive cerium and negative yttrium anomalies are diagnostic for non-phosphatized crusts, indicating oxic environment for the growth of the younger layers (Bau et al., 2014). A positive yttrium anomaly is common for phosphatized crusts (Fig. 8); however, the cerium anomalies are negative in some samples and positive in others, indicating a suboxic environment for the phosphatization of the crusts (Bau et al., 2014). REY are enriched in phosphatized crusts from both regions (Fig. 8). Some phosphatized samples have undergone intense phosphatization, especially in brecciated parts of the phosphatized layers showing a very negative cerium anomaly (Fig. 8). Our results are consistent with previous studies (Koschinsky et al., 1997; Kuhn et al., 1998; Bau et al., 2014; Sousa et al., 2021; Benites et al., 2022). Jiang et al. (2020) studied phosphatized FeMn crusts in which different stages of phosphatization corresponded to different intensities of negative cerium anomaly. The binary diagram of Bau et al. (2014) identifies the quadrant of hydrogenetic FeMn crusts based on Ce_{SN}/Ce_{SN}^* vs Nd and Y_{SN}/Ho_{SN}. Most of the non-phosphatized samples used in this study fall into the hydrogenetic field (Fig. 7). Although Bau et al. (2014) pointed out that this classification should not be used for phosphatized crusts, we also plotted the phosphatized samples in the diagram to stress the separation of phosphatized and non-phosphatized crusts (Fig. 7).

Elemental ratios of Fe, Mn, Ca and P in phosphatized and non-phosphatized crusts (Fig. S1) suggest that phosphatization causes the removal of Fe-oxyhydroxides while increasing the abundance of CFA. This process not only removes magnetic components but also increases the diamagnetic dilution of remaining magnetic signals in the phosphatized crusts. Both the geochemical classifications and the REY content show that hydrogenetic and phosphatized crusts are geochemically distinct. Phosphatization occurred in suboxic conditions, which led to replacement of Fe and Mn oxyhydroxide phases.

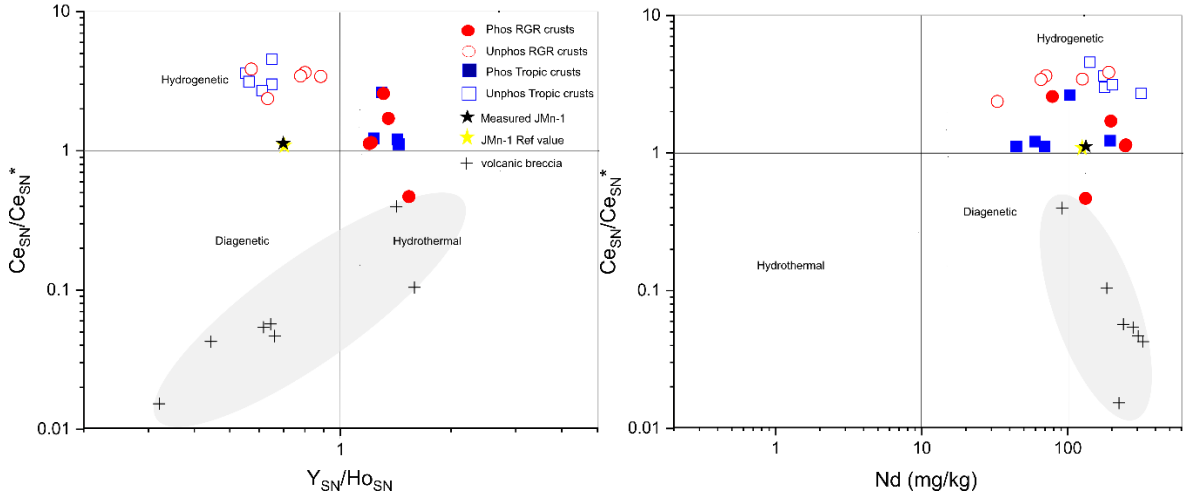

Fig. 7: Binary diagrams from Bau et al. (2014) - Ce_{SN}/Ce_{SN}^* vs Nd and Y_{SN}/Ho_{SN} classify hydrogenetic, hydrothermal and diagenetic FeMn crusts, based on Y, Nd and Ho contents. The shaded area of the binary diagram represents the highly altered brecciated parts (volcanic breccia) of FeMn crusts from both RGR and TS (Ce = Cerium, Nd = Neodymium, Y = Yttrium, Ho= Holmium, SN – Shale-normalized).

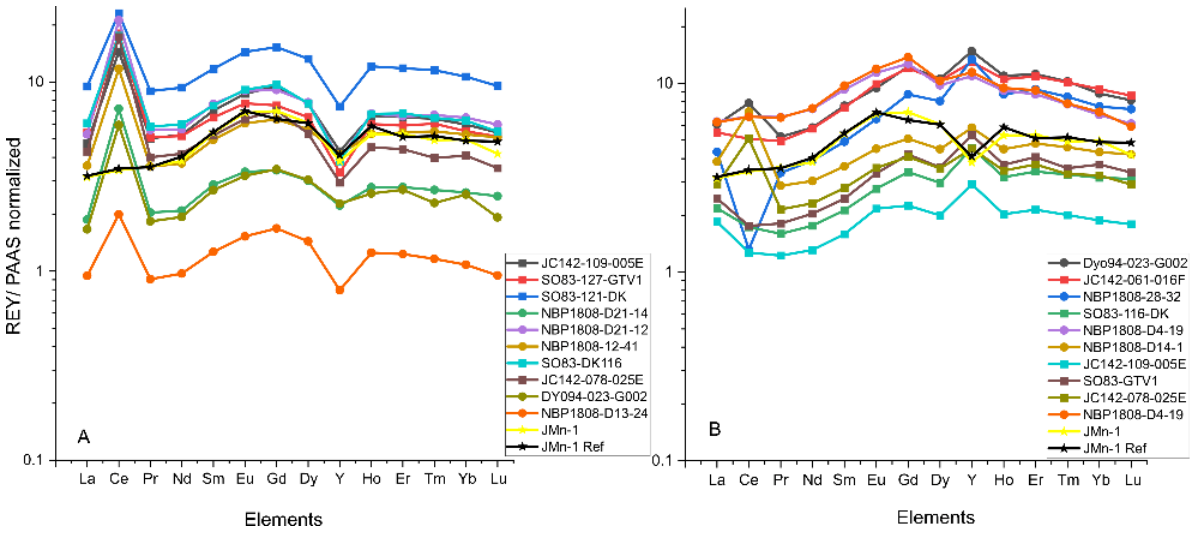

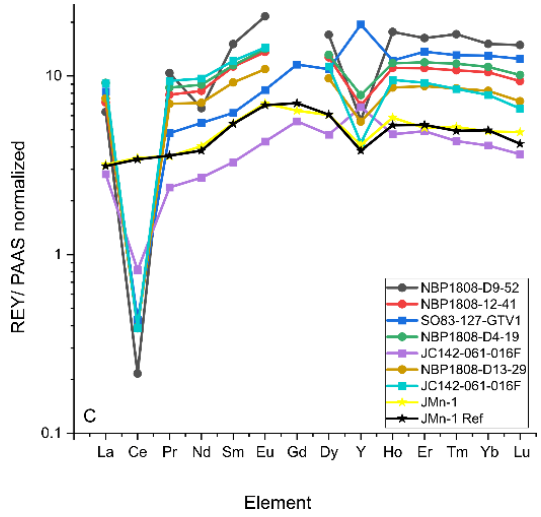

Fig.8: Shale normalized, Rare Earth Elements and Yttrium: A- Hydrogenetic non-phosphatized FeMn crusts showing negative yttrium and positive cerium anomalies, B- Phosphatized crusts showing positive yttrium anomaly and significantly smaller Ce anomalies compared to A, C- Highly altered brecciated parts of FeMn crusts with very negative cerium anomaly. Yellow and black lines in A, B and C show the standard CRM JMn-1.

3.4.1.3 Mineralogy

XRD results show that the hydrogenetic FeMn crusts contain amorphous Fe-oxyhydroxides and Mn-oxides, whereas the crystalline phases are vernadite with traces of quartz and calcite (Fig. 9). The phosphatized crusts exhibit a higher variety and abundance of minerals relative to non-phosphatized crusts, including todorokite, apatite, feldspar, vernadite, calcite and goethite. The different mineral associations in non-phosphatized and phosphatized FeMn crusts suggest formation in different oceanographic conditions. The volcanic breccia cemented by CFA showing distinct Cerium anomalies (Fig. 8) contains minerals which are common in phosphatized crusts, plus the presence of magnetic minerals (i.e., magnetite/hematite) (Fig. 9).

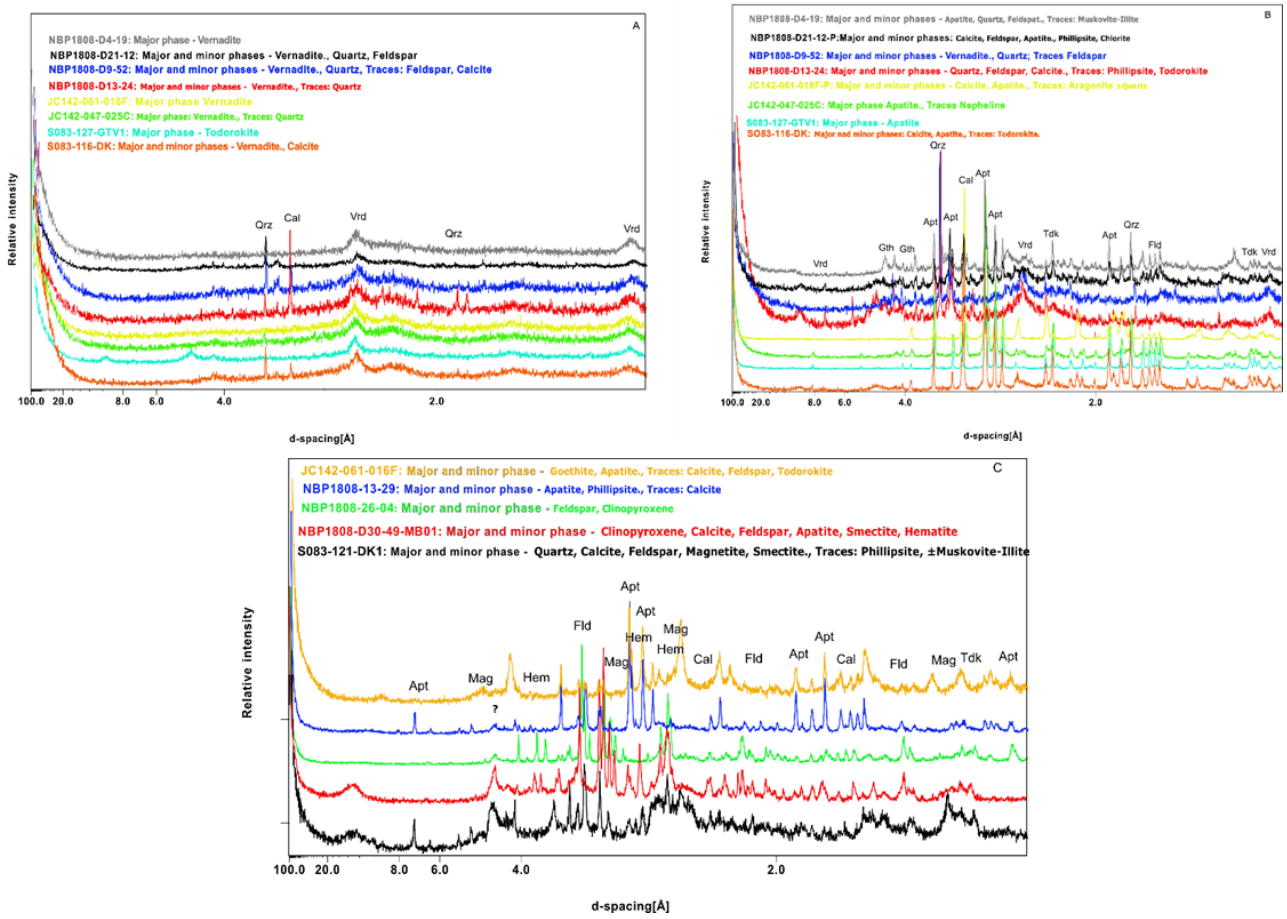

Fig.9: XRD results: A- Hydrogenetic non-phosphatized FeMn crusts showing the presence of vernadite, quartz and calcite, B- Phosphatized crusts showing a variety of minerals including apatite, feldspar, quartz, calcite, todorokite, vernadite and goethite, C- Phosphatized crusts with volcanic breccia containing magnetic minerals.

3.3.2 **Magnetism**

3.4.2.1 Rock magnetism and Paleomagnetism

In general, rock magnetic measurements on non-phosphatized layers of the FeMn crust samples from both regions show the presence of paramagnetic/superparamagnetic fractions implying Fe oxyhydroxides in the non-phosphatized layers are amorphous/poorly crystalline goethite. (Fig.10). FORCs and hysteresis results contain no convincing fingerprints for remanence carrying ferromagnetic minerals in the non-phosphatized layers of FeMn crusts. The phosphatized layers from RGR samples also contain acicular goethite which is the result of bacterial activity and dehydration of previously existing x-ray amorphous Fe oxyhydroxides (diagenesis) (Benites et al., 2022). The hysteresis curves of these subsamples show characteristic features of goethite as the samples containing goethite don't saturate at the

maximum magnetic field provided during measurements. The presence of acicular goethite was also confirmed by thermomagnetic curves (Fig.11) as well as TEM images (Fig.S3). Goethite is also found in some hydrogenetic (non-phosphatized) and phosphatized layers of crust samples from TS. However, it is only present in some intervals along the crusts which are related to the dust input from the African continent and do not play a significant role in the primary remanent magnetization of FeMn crusts (Josso et al., 2019).

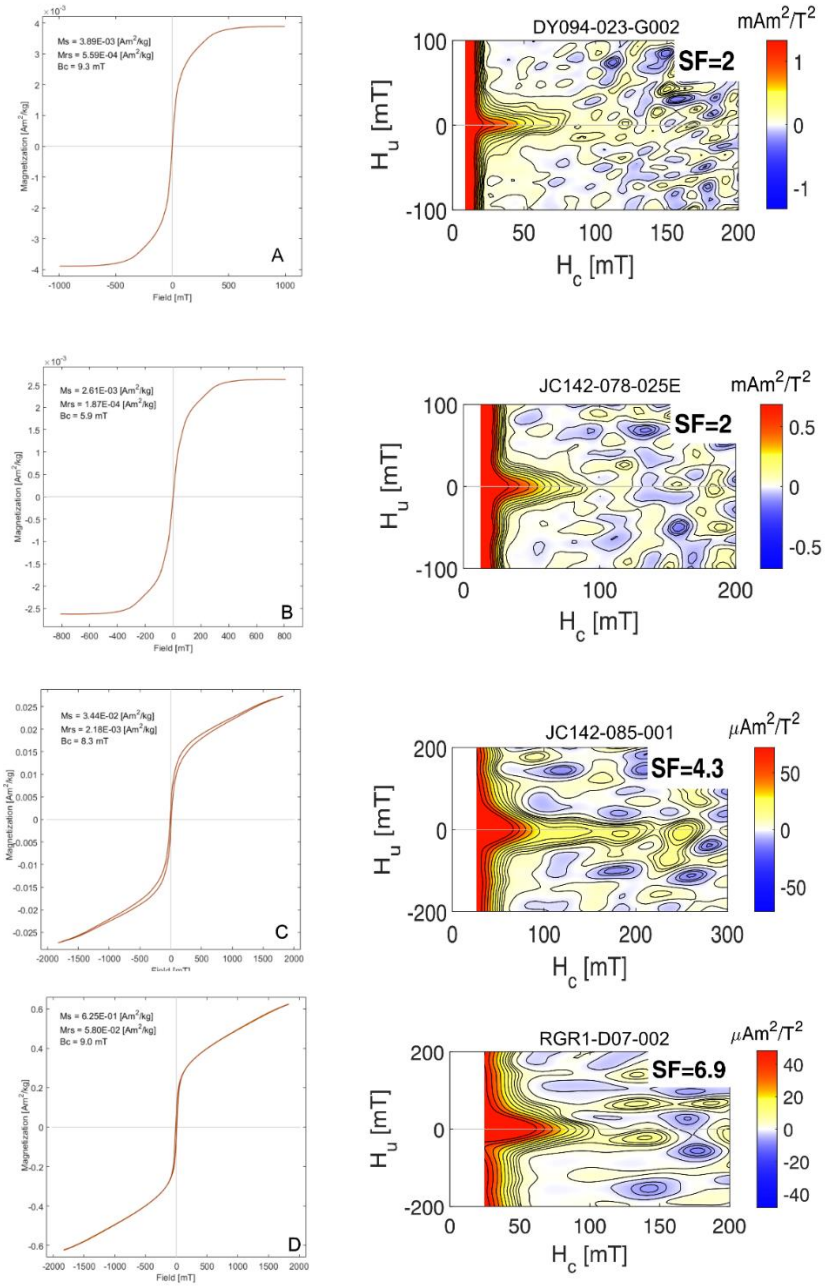

Fig.10A: Hysteresis loops and corresponding First Order Reversal Curves (FORCs): A- Hysteresis loop and FORCs for the non-phosphatized layer of FeMn crust from the RGR, representing paramagnetic/superparamagnetic amorphous Fe oxyhydroxides B- Hysteresis loop and FORCs for the non-phosphatized layer of FeMn crust from the TS, representing paramagnetic/superparamagnetic amorphous Fe oxyhydroxides C- Hysteresis loop and FORCs for the phosphatized layer of FeMn crust

from the RGR, representing poorly crystalline Goethite, D- Hysteresis loop and FORCs for the phosphatized layer of FeMn crust from the TS, representing poorly crystalline goethite.

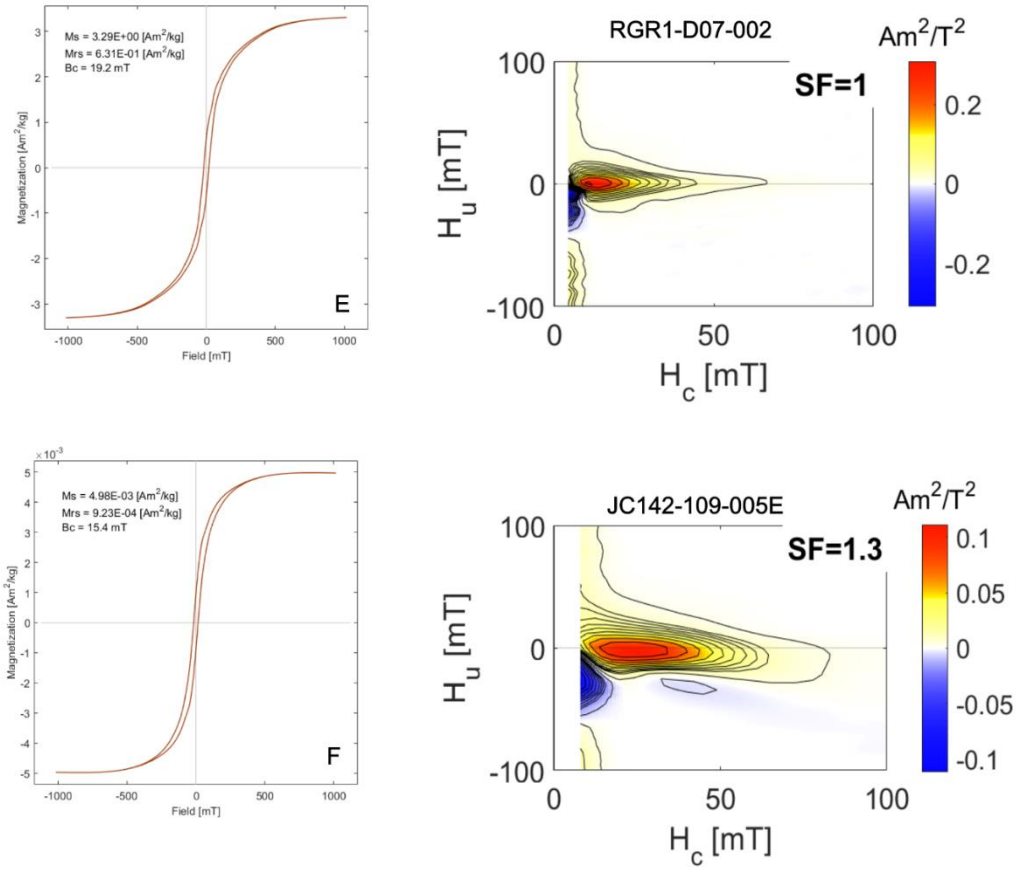

Fig.10B: Hysteresis loops and corresponding First Order Reversal Curves (FORCs): E- Hysteresis loop and FORCs for the phosphatized volcanic breccia of FeMn crust from the RGR, representing low coercive pseudo-single domain ferromagnetic fraction with superparamagnetic components, F- Hysteresis loop and FORCs for the phosphatized volcanic breccia of FeMn crust from the TS, representing low coercive pseudo-single domain ferromagnetic fraction with superparamagnetic components.

Fittings with two doublets from the Mössbauer spectra reveal that there are no magnetic Fe oxides since sextets do not appear (Fig.12). The values of the isomeric shifts relative to metallic Fe are (0.31, 0.48) for RGR1-D07-002 and (0.30, 0.49) for JC142-085-001 and (0.24, 0.42) for JC-142-078-025E. These isomer shift values are all characteristic of Fe^{3+} oxidation states. Mössbauer spectroscopy revealed no Fe^{+2} in the magnetic extract. Our results are consistent with previous studies on FeMn nodules and crusts from the Indian Ocean (Carpenter et al., 1973; Pattan and Mudhokar, 1991; Rusanov et al., 2008; Ganwani et al., 2017).

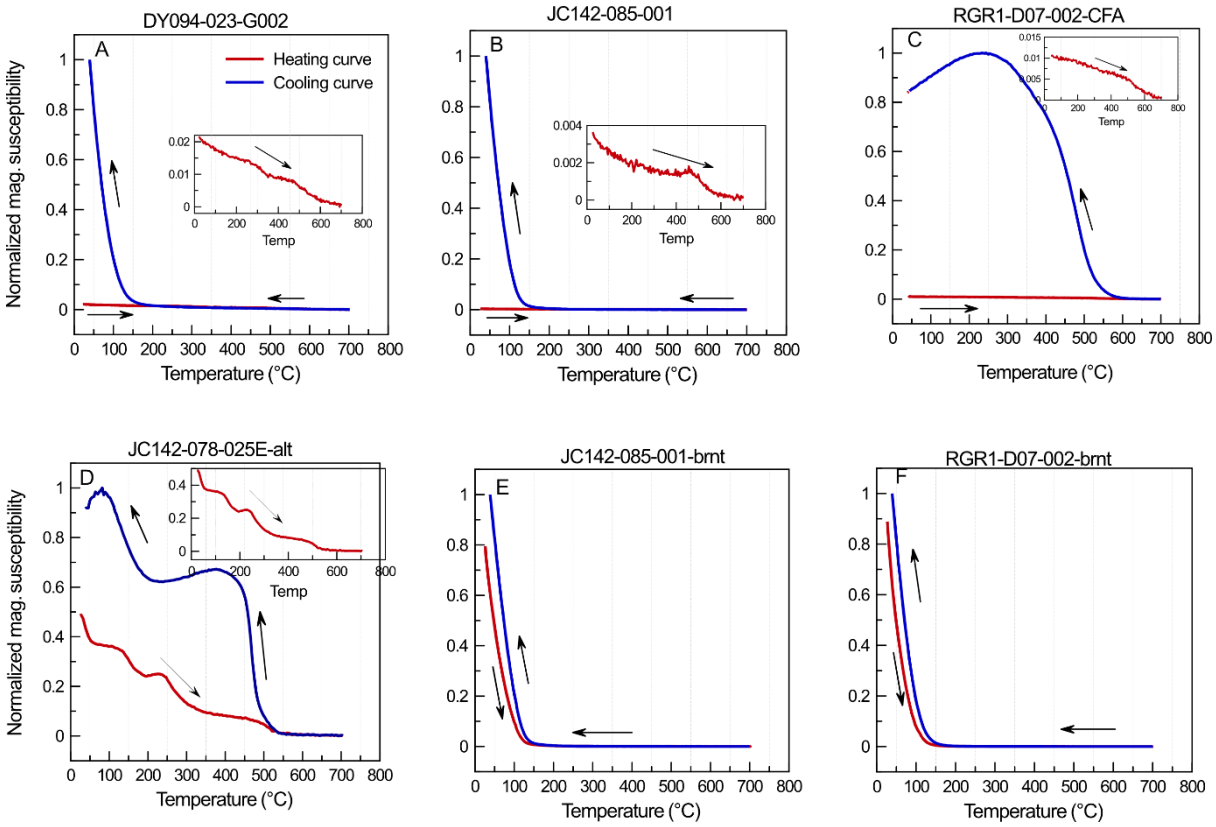

Fig.11: Thermomagnetic curves for: A- Non-phosphatized sample from RGR, B- Non-phosphatized sample from TS, C- Phosphatized sample from RGR, D- Phosphatized sample from TS, E- Remeasurement of already analyzed sample (TS) in the Argon environment, representing goethite with the Curie temperature at 120º C, F- Remeasurement of already analyzed sample (RGR) in the Argon environment, representing goethite with the Curie temperature at 120º C.

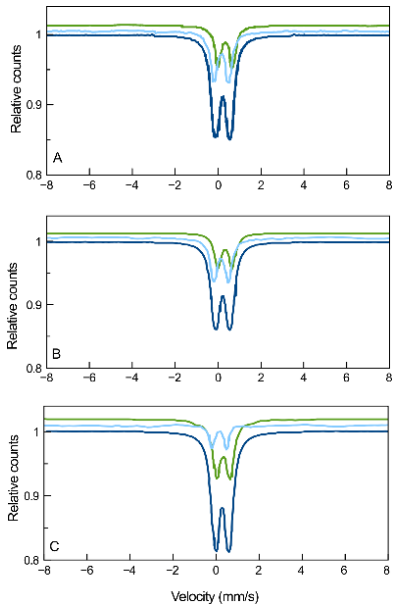

Fig.12: Mössbauer Spectroscopy of magnetic extract: A, - Non-phosphatized sample with amorphous Fe oxyhydroxides from RGR (RGR1-D07-002), representing Fe^{+3} phase B - Non-phosphatized sample with amorphous Fe oxyhydroxides from TS (JC142-085-001), representing Fe^{+3} phase C- Phosphatized sample with abundant poorly crystalline goethite from TS (JC142-085-001), representing Fe^{+3} phase only.

FeMn crust slices used for the stepwise demagnetization showed no signs of smooth demagnetization and hence the results would not show reliable ChRM (Fig.S3). No sample could give MAD 3 angle less than 12º plotted from a Puffin Plot providing vague and ambiguous results.

3.4.2.2 Magnetic Scanning

Hall probe magnetic scanning performed on 4 crust samples (Fig.S4) suggests the FeMn crusts from RGR and TS don't show primary remanence characteristics. The results for both scanning lines after background subtraction are similar, showing the accuracy of the method used. In all samples, the magnetic data obtained from Hall probe scanning is not consistent with the expected variation in magnetic intensity, consequently confirming that the studied FeMn crusts don't show signs of original magnetic remanence. The samples (Fig.S4A (TS) and Fig.S4B (RGR)) are already dated by using radioisotopes (Josso et al., 2019, Benites et al., 2020). Change in magnetic data is caused by the variation in geochemistry and mineralogy as the magnetic changes correlate with the concentration of Fe and P. This implies that the magnetic minerals have suffered diagenetic alteration during phosphatization under sub-oxic conditions, causing the complete disappearance of primary remanent magnetization. Suboxic dissolution of magnetic minerals especially biogenic magnetite has been well explained in previous studies (Karlin, 1990; Roberts, 2015; Maxbauer et al., 2016; Xu et al., 2020; Yamazaki, 2020).

Acicular goethite in some layers of crust samples is a result of continental detritus (Josso et al., 2019) while the crust samples from RGR show the crystallization of goethite in the form of "ironstone" in the diagenetically altered (phosphatized) layer (Benites et al., 2020). According to Benites et al. (2022), goethite started mineralizing from the late Miocene extending to the Quaternary due to the several generations of bacterial mats and Fe dissolution and reprecipitation.

3.4 **Discussion**

Indirect magnetometric methods have been previously used for the characterization of rocks in the RGR (Praxedes et al., 2019; Sergipe et al., 2023). Despite widespread pavements of FeMn crusts have been previously reported in the region (Benites et al., 2020, 2022; Sousa et al., 2021; Jovane et al., 2019), FeMn crusts do not show any significant magnetic anomaly, as their magnetic signals are almost indistinguishable from the background (Praxedes et al., 2019). To

explain the absence of magnetic anomaly, we propose that the absence of remanence-carrying magnetic minerals and the presence of X-ray amorphous, weakly magnetic (paramagnetic and superparamagnetic) Fe-oxyhydroxides provide more convincing arguments than the effects of erosion and the reduced thickness of FeMn crusts, proposed by Praxedes et al. (2019) and Sergipe et al. (2023).

FeMn crusts from TS contain abundant, poorly crystalline, X-ray amorphous Fe oxyhydroxides and intergrown minerals, like vernadite, in hydrogenetic non-phosphatized layers (Marino et al., 2017, 2019; Josso et al., 2019). This implies that, although FeMn crusts are rich in Fe, they do not contain remanence-carrying crystalline magnetic minerals. Only Fe(III) is present in the crusts (Fig. 12), in line with previous studies pointing out that Fe(III) dominates amorphous and poorly crystalline Fe oxides and Fe oxyhydroxides (Carpenter et al., 1973; Murad and Schwertmann, 1988; Pattan and Mudhokar, 1991; Rusanov et al., 2008; Ganwani et al., 2017). Previous magnetostratigraphic studies on FeMn crust from the Pacific Ocean, China Sea and Indian Ocean were based on the concept that primary remanent magnetization arises from biogenic magnetite produced by magnetotactic bacteria or detrital magnetite (Oda et al., 2011, Yuan et al., 2017; Noguchi et al., 2017a, Noguchi et al., 2017b). However, there is still no compelling explanation of the mechanism of magnetite biomineralization or of the preservation of detrital magnetite in hydrogenetic FeMn crusts on a global scale.

Yuan et al. (2020) proposed that the precipitation of hydrogenetic FeMn crusts is an inorganic colloidal process which consumes oxygen and forms a protective layer between the oxygenated deep water and the FeMn phase, promoting suitable conditions for the biomineralization of magnetic minerals. According to these authors, the corrosion and dissolution of fine plankton particles would cause a decrease oxygen concentration, promoting microaerophilic environment suitable for magnetotactic bacteria (Yuan et al., 2020). Our studies show no evidence of magnetotactic bacteria (MTB) in the studied FeMn crust, hence the magnetite biomineralization in FeMn crusts could be a local rather than a regional or global phenomenon of primary biogeochemical remanent magnetization, depending on the local availability of oxygen and organic matter. Moreover, oscillating microenvironmental conditions could lead to magnetite dissolution under suboxic conditions or magnetite oxidation under oxic conditions, raising the question about the stability of biogenic magnetite both in hydrogenetic and in diagenetic (phosphatized) FeMn layers. In other words, if biogenic magnetite was a primary magnetic mineral in FeMn crusts, it would probably be rapidly oxidized to Fe(III) (Stumm and Morgan, 1996; Liu et al., 2012) generating poorly crystalline Fe oxyhydroxides. Biogenic magnetite is stable only under a narrow range of redox and pH conditions (Bazylinski and

Frankel, 2004; Rodelli et al., 2018, 2019; Faivre and Schuler, 2008; Kopp and Kirschvink, 2008). In oxygenated environments, biogenic magnetite is expected to oxidize, whereas in suboxic environments, it is expected to dissolve (Rodelli et al., 2018, 2019; Faivre and Schuler, 2008; Kopp and Kirschvink, 2008; Roberts et al., 2011). Biogenic magnetite is stable in the oxic-suboxic transition zone where oxygen is controlled by MTB (Yamazaki and Ikehara, 2012). Remanence-carrying magnetic minerals have not been found either in the non-phosphatized or in the phosphatized layers of FeMn crusts presented in this study. However, hematite and magnetite are present in some samples containing volcanic breccia (Fig. 9). Our samples do not contain stable ferromagnetic Fe oxides, and, to the best of our knowledge, no studies have described the formation of well-crystallized Fe oxides (other than biogenic magnetite) in FeMn crusts. However, amorphous Fe oxides have been previously reported by Guan et al. (2017). Oxidation of pre-existing minerals should be considered a common phenomenon, because hydrogenetic non-phosphatized crusts normally grow under oxic conditions (e.g., Marino et al., 2017), which is evidenced by the pronounced positive cerium anomaly (Fig. 8). A metal-rich oxygen minimum zone (OMZ) above the top of seamounts can serve as a metal source for the formation of FeMn crusts. However, these metals get oxidized before precipitation on the substrate (Marino et al., 2017). The oxidation of dissolved Fe(II) is the major cause of the absence of crystallized ferrimagnetic minerals. Furthermore, the biogenic oxidation of reduced forms of Fe and Mn by microbial communities has been pointed out as the earliest stage of FeMn formation (Templeton et al., 2009; Jiang et al., 2019).

We propose a model for the formation of well-crystallized Fe oxides, especially biogenic magnetite, in non-phosphatized FeMn crusts, as illustrated in Fig. 13. The formation of FeMn crusts near the oxygen minimum zone can be the cause for the formation of biogenic magnetite. In line with Larrasoana et al. (2014) and Yuan et al. (2020), we propose that remanent magnetization is linked to biogenic magnetite produced by magnetotactic bacteria. Magnetite preservation is favoured in a microaerophilic environment due to the decomposition of organic matter. Biogenic magnetite preservation is favored especially on the top of seamounts directly below the OMZ. Changes in the depth of the OMZ through time, can influence the preservation of remanence-carrying Fe oxides.

The phosphatization of FeMn crusts is linked to oceanic circulation overturning, due to the upwelling of nutrients promoted by increased biological productivity (Halbach and Puteanus, 1984). As a result, a phosphate-rich oxygen minimum zone (OMZ) may extend to the seamount summit where FeMn crusts grow. Phosphate-rich suboxic water causes dissolution and diagenetic alterations of FeMn crusts. Since FeMn crusts are highly porous (Hein et al., 2000),

these diagenetic alterations initiate the impregnation and replacement of FeMn phase by the CFA, initially by precipitating minerals such as todorokite (Fig. 9) (Halbach et al., 1989a, Halbach et al., 1989b, Koschinsky et al., 1997). Major phosphatization events throughout the geological history of FeMn crusts formation in the Atlantic Ocean have been reported in previous studies (Josso et al., 2021; Benites et al., 2022, 2020; Marino et al., 2018; González et al., 2016). In our study, most of the FeMn crusts show phosphatization at their basal layers and show no primary remanent magnetization because these layers have undergone extensive diagenetic alteration (Fig .8, S1 and 8). Phosphate-rich suboxic water increases the replacement and recrystallization of unstable minerals through fractures and pores (Benites et al., 2020; Koschinsky et al., 1997).

In the phosphatized layers of the crust samples from RGR, acicular goethite (Fig.S2) is the ordered phase of dehydration and recrystallization of pre-existing ferrihydrite, mediated by Fe-oxidizing bacteria (Benites et al., 2022). Our magnetic, mineralogical and TEM data confirmed the presence of acicular goethite both in the RGR and on the TS. Goethite is a magnetic mineral with the potential of preserving primary remanent magnetization, however, most crystalline acicular goethite in FeMn crusts (i.e., the ordered and recrystallized form of pre-existing poorly crystalline Fe oxyhydroxides) is the result of diagenesis. Our results from the demagnetization (Fig. S3) of sliced samples do not suggest the existence of primary magnetization recorded by goethite. Magnetic scanning data for the phosphatized layers of sample JC142-085-001 shows that the magnetic changes along the growth of the crust are driven by changes in Fe, Mn, P and Ca contents. Moreover, magnetic scanning data show a consistent magnetic change in erosive surfaces of FeMn crusts (Josso et al., 2019). These magnetic anomalies are not consistent with the expected magnetic response showing primary remanent magnetization. However, the magnetic response is related to the textural and geochemical changes along the crust. Since the phosphatized FeMn crusts are altered FeMn crusts, the magnetic minerals found in phosphatized layers would not reflect the original remanent magnetization.

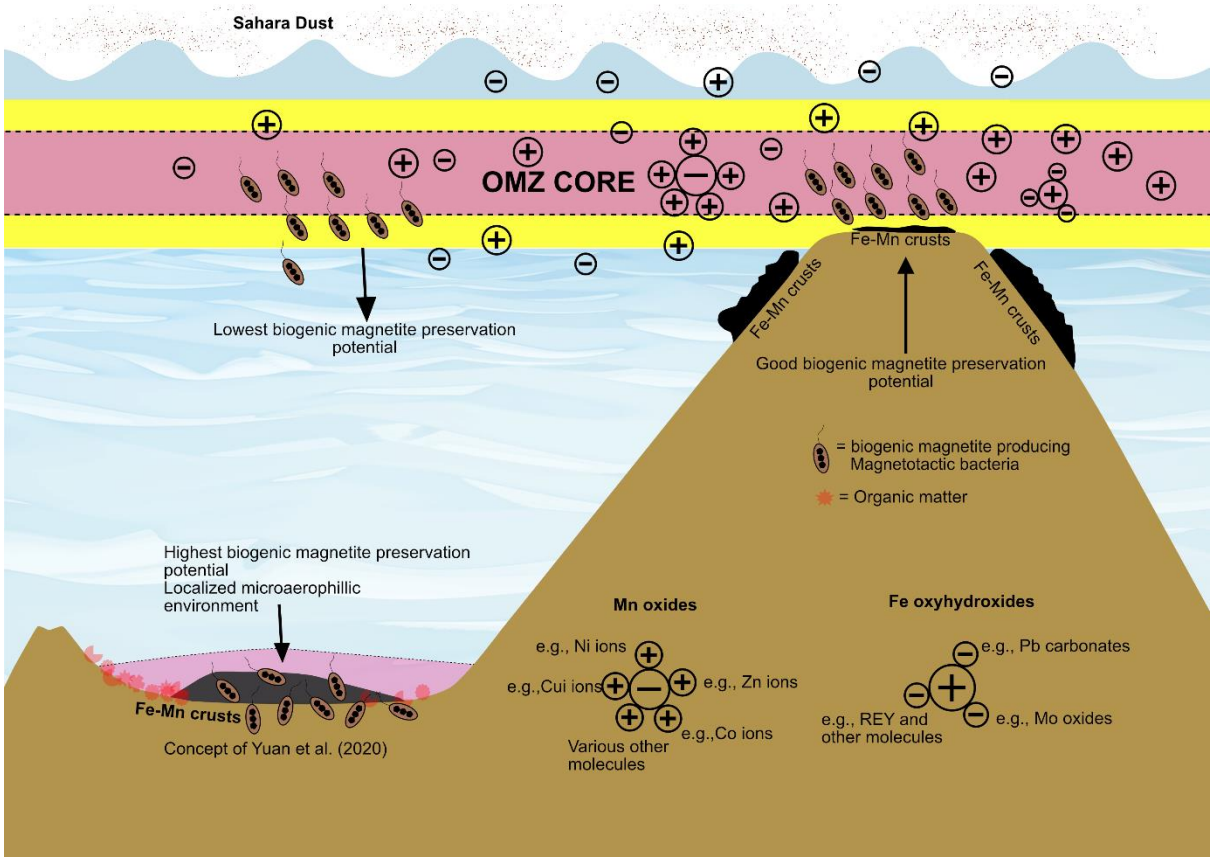

Fig.13: Schematic diagram for the possible preservation of biogenic magnetite produced by magnetotacctic bacteria as a primary magnetic carrier in non-phosphatized FeMn crusts: Modified from Marino et al. (2017), the diagram incorporates the concept of Yuan et al. (2020) about the localized microaerophilic environment due to the corrosion of remains of planktons (organic matter). The concept of highest, good, and lowest biogenic magnetite preservation is from Larrasoana et al. (2014).

3.5 Conclusions

We used geochemical, magnetic, mineralogical, and microscopic methods to understand the magnetic properties of FeMn crusts from RGR and TS. FeMn crusts from RGR and TS typically grow hydrogenetically under oxic conditions, preventing crystallization of primary remanent magnetization carrying magnetic minerals, and potentially causing oxidation of pre-existing magnetic minerals. The non-phosphatized layers in samples from both regions contain paramagnetic/superparamagnetic amorphous Fe oxyhydroxides which are not reliable for carrying primary remanent magnetization. Different phosphatization stages throughout the formation history of FeMn crusts have altered not only the primary geochemical and mineralogical signals but also the magnetic signals. CFA replaces Fe and Mn-phases, promoting magnetic dilution. Moreover, during phosphatization magnetic minerals undergo sub-oxic dissolution, thereby losing their primary magnetic signals. Variability in magnetic parameters

does not correspond to primary magnetization but rather to geochemical alterations. Extending the interpretation of our results to the presence of magnetic minerals as primary remanent magnetization carriers in the Pacific Ocean and China Sea suggest that local environmental condition may be crucial for the preservation of these minerals, while the absence of Fe(II) is a common feature in FeMn crusts worldwide.

References

Ayers, J. M., & Strutton, P. G. (2013). Nutrient variability in subantarctic mode waters forced by the southern annular mode and ENSO. *Geophysical Research Letters*, *40*(13), 3419-3423.

Barker, P. F., Johnson, R., Carlson, R. L., Johnson, D., Cepek, P., Coulbourn, W., ... and Walton, W. (1983). Site-516-Rio-Grande Rise. *Initial Reports of the Deep Sea Drilling Project*, *72*(Dec), 155-338.

Bau, M. S. K. K., Schmidt, K., Koschinsky, A., Hein, J., Kuhn, T., & Usui, A. (2014). Discriminating between different genetic types of marine ferro-manganese crusts and nodules based on rare earth elements and yttrium. *Chemical Geology*, *381*, 1-9.

Bau, M., & Koschinsky, A. (2006). Hafnium and neodymium isotopes in seawater and in ferromanganese crusts: the "element perspective". *Earth and Planetary Science Letters*, *241*(3-4), 952-961.

Bazylinski, D. A., & Frankel, R. B. (2004). Magnetosome formation in prokaryotes. *Nature Reviews Microbiology*, *2*(3), 217-230.

Benites, M., Hein, J. R., Mizell, K., Blackburn, T., & Jovane, L. (2020). Genesis and evolution of ferromanganese crusts from the summit of Rio Grande Rise, Southwest Atlantic Ocean. *Minerals*, *10*(4), 349.

Benites, M., Hein, J. R., Mizell, K., Farley, K. A., Treffkorn, J., & Jovane, L. (2022). Geochemical insights into formation of enigmatic ironstones from Rio Grande rise, South Atlantic Ocean. *Marine Geology*, *444*, 106716.

Berndt, T. A., & Chang, L. (2019). Waiting for Forcot: Accelerating FORC processing 100× using a fast-Fourier-transform algorithm. *Geochemistry, Geophysics, Geosystems*, *20*(12), 6223-6233.

Bogdanova, O. Y., Gorshkov, A. I., Novikov, G. V., & Bogdanov, Y. A. (2008). Mineralogy of morphogenetic types of ferromanganese deposits in the world ocean. *Geology of Ore Deposits*, *50*, 462-469.

Bonatti, E. (1972). Classification and genesis of submarine iron-manganese deposits. *Ferromanganese deposits on the ocean floor*.

Brandt, P., Greatbatch, R. J., Claus, M., Didwischus, S. H., Hormann, V., Funk, A., ... & Körtzinger, A. (2012). Ventilation of the equatorial Atlantic by the equatorial deep jets. *Journal of Geophysical Research: Oceans*, *117*(C12).

Brandt, P., Hormann, V., Körtzinger, A., Visbeck, M., Krahmann, G., Stramma, L., ... & Schmid, C. (2010). Changes in the ventilation of the oxygen minimum zone of the tropical North Atlantic. *Journal of Physical Oceanography*, *40*(8), 1784-1801.

Camboa, L. A. P., & Rabinowitz, P. D. (1984). The evolution of the Rio Grande Rise in the southwest Atlantic Ocean. *Marine Geology*, *58*(1-2), 35-58.

Carpenter, R., & Wakeham, S. (1973). Mössbauer studies of marine and fresh water manganese nodules. *Chemical Geology*, *11*(2), 109-116.

Dymond, J., Lyle, M., Finney, B., Piper, D. Z., Murphy, K., Conard, R., & Pisias, N. (1984). Ferromanganese nodules from MANOP Sites H, S, and R—Control of mineralogical and chemical composition by multiple accretionary processes. *Geochimica et Cosmochimica Acta*, *48*(5), 931-949.

Emerson, D., Roden, E., & Twining, B. (2012). The microbial ferrous wheel: iron cycling in terrestrial, freshwater, and marine environments. *Frontiers in microbiology*, *3*, 383.

Faivre, D., & Schuler, D. (2008). Magnetotactic bacteria and magnetosomes. *Chemical reviews*, *108*(11), 4875-4898.

Frank, M., O'nions, R. K., Hein, J. R., & Banakar, V. K. (1999). 60 Myr records of major elements and Pb–Nd isotopes from hydrogenous ferromanganese crusts: reconstruction of seawater paleochemistry. *Geochimica et Cosmochimica Acta*, *63*(11-12), 1689-1708.

Ganwani, G., Bhatia, B., Jaisankar, S., Pattan, J. N., Dixit, A., & Tripathi, R. P. (2017). MÖssbauer spectroscopy and x-ray diffraction studies of ferromanganese nodules from central Indian ocean basin. *Journal of Applied Geochemistry*, *19*(3), 270-276.

González, F. J., Somoza, L., Hein, J. R., Medialdea, T., León, R., Urgorri, V., ... & Martín-Rubí, J. A. (2016). Phosphorites, Co-rich Mn nodules, and Fe-Mn crusts from Galicia Bank, NE Atlantic: Reflections of Cenozoic tectonics and paleoceanography. *Geochemistry, Geophysics, Geosystems*, *17*(2), 346-374.

Guan, Y., Sun, X., Jiang, X., Sa, R., Zhou, L., Huang, Y., ... & Wang, C. (2017). The effect of Fe-Mn minerals and seawater interface and enrichment mechanism of ore-forming elements of polymetallic crusts and nodules from the South China Sea. *Acta Oceanologica Sinica*, *36*, 34-46.

Halbach, P., & Puteanus, D. (1984). The influence of the carbonate dissolution rate on the growth and composition of Co-rich ferromanganese crusts from Central Pacific seamount areas. *Earth and Planetary Science Letters*, *68*(1), 73-87.

Halbach, P., Kriete, C., Prause, B., & Puteanus, D. (1989). Mechanisms to explain the platinum concentration in ferromanganese seamount crusts. *Chemical Geology*, *76*(1-2), 95-106.

Halbach, P., Sattler, C. D., Teichmann, F., & Wahsner, M. (1989). Cobalt-rich and platinum-bearing manganese crust deposits on seamounts: nature, formation, and metal potential. *Marine Mining*, *8*(1), 23-39.

Hassan, M. B., Rodelli, D., Benites, M., Abreu, F., Murton, B., & Jovane, L. (2020). Presence of biogenic magnetite in ferromanganese nodules. *Environmental microbiology reports*, *12*(3), 288-295.

Hein, J. R., & Koschinsky, A. (2014). Deep-ocean ferromanganese crusts and nodules.

Hein, J. R., Conrad, T. A., & Staudigel, H. (2010). Seamount mineral deposits: a source of rare metals for high-technology industries. *Oceanography*, *23*(1), 184-189.

Hein, J. R., Conrad, T. A., Frank, M., Christl, M., & Sager, W. W. (2012). Copper-nickel-rich, amalgamated ferromanganese crust-nodule deposits from Shatsky Rise, NW Pacific. Geochemistry, Geophysics, Geosystems, 13(10).

Hein, J. R., Koschinsky, A., & Halliday, A. N. (2003). Global occurrence of tellurium-rich ferromanganese crusts and a model for the enrichment of tellurium. Geochimica et Cosmochimica Acta, 67(6), 1117-1127.

Hein, J. R., Koschinsky, A., Bau, M., Manheim, F. T., Kang, J. K., & Roberts, L. (2000). Cobalt-rich ferromanganese crusts in the Pacific. Handbook of marine mineral deposits, 18, 239-273.

Hein, J. R., Mizell, K., Koschinsky, A., & Conrad, T. A. (2013). Deep-ocean mineral deposits as a source of critical metals for high-and green-technology applications: Comparison with land-based resources. Ore Geology Reviews, 51, 1-14.

Jiang, X. D., Sun, X. M., & Guan, Y. (2019). Biogenic mineralization in the ferromanganese nodules and crusts from the South China Sea. *Journal of Asian Earth Sciences*, *171*, 46-59.

Jiang, X. D., Sun, X. M., Chou, Y. M., Hein, J. R., He, G. W., Fu, Y., ... & Ren, J. B. (2020). Geochemistry and origins of carbonate fluorapatite in seamount FeMn crusts from the Pacific Ocean. *Marine Geology*, *423*, 106135.

Jiang, X., Zhao, X., Zhao, X., Chou, Y. M., Hein, J. R., Sun, X., ... & Liu, Q. (2021). A magnetic approach to unravelling the paleoenvironmental significance of nanometer-sized Fe hydroxide in NW Pacific ferromanganese deposits. *Earth and Planetary Science Letters*, *565*, 116945.

Joshima, M., & Usui, A. (1998). Magnetostratigraphy of hydrogenetic manganese crusts from Northwestern Pacific seamounts. *Marine Geology*, *146*(1-4), 53-62.

Josso, P., Lusty, P., Chenery, S., & Murton, B. (2021). Controls on metal enrichment in ferromanganese crusts: Temporal changes in oceanic metal flux or phosphatisation?. *Geochimica et Cosmochimica Acta*, *308*, 60-74.

Josso, P., Parkinson, I., Horstwood, M., Lusty, P., Chenery, S., & Murton, B. (2019). Improving confidence in ferromanganese crust age models: A composite geochemical approach. *Chemical Geology*, *513*, 108-119.

Jovane, L., Hein, J. R., Yeo, I. A., Benites, M., Bergo, N. M., Correa, P. V., ... & Brandini, F. P. (2019). Multidisciplinary scientific cruise to the Rio Grande Rise. *Frontiers in Marine Science*, *6*, 252.

Karlin, R. (1990). Magnetic mineral diagenesis in suboxic sediments at Bettis site W-N, NE Pacific Ocean. *Journal of Geophysical Research: Solid Earth*, *95*(B4), 4421-4436.

Kirschvink, J. (1980). The least-squares line and plane and the analysis of palaeomagnetic data. *Geophysical Journal International*, *62*(3), 699-718.

Kletetschka, G., Schnabl, P., Šifnerová, K., Tasáryová, Z., Manda, Š., & Pruner, P. (2013). Magnetic scanning and interpretation of paleomagnetic data from Prague Synform's volcanics. *Studia Geophysica et Geodaetica*, *57*(1), 103-117.

Konstantinova, N., Cherkashov, G., Hein, J. R., Mirão, J., Dias, L., Madureira, P., ... & Maksimov, F. (2017). Composition and characteristics of the ferromanganese crusts from the western Arctic Ocean. *Ore Geology Reviews*, *87*, 88-99.

Kopp, R. E., & Kirschvink, J. L. (2008). The identification and biogeochemical interpretation of fossil magnetotactic bacteria. *Earth-Science Reviews*, *86*(1-4), 42-61.

Koschinsky, A., & Hein, J. R. (2003). Uptake of elements from seawater by ferromanganese

crusts: solid-phase associations and seawater speciation. *Marine Geology*, *198*(3-4), 331-351.

Koschinsky, A., & Hein, J. R. (2017). Marine ferromanganese encrustations: archives of changing oceans. *Elements: An International Magazine of Mineralogy, Geochemistry, and Petrology*, *13*(3), 177-182.

Koschinsky, A., Halbach, P., Hein, J. R., & Mangini, A. (1996). Ferromanganese crusts as indicators for paleoceanographic events in the NE Atlantic. *Geologische Rundschau*, *85*(3), 567-576.

Koschinsky, A., Stascheit, A., Bau, M., & Halbach, P. (1997). Effects of phosphatization on the geochemical and mineralogical composition of marine ferromanganese crusts. *Geochimica et Cosmochimica Acta*, *61*(19), 4079-4094.

Koschinsky, A., Van Gerven, M., & Halbach, P. (1995). First investigations of massive ferromanganese crusts in the NE Atlantic in comparison with hydrogenetic Pacific occurrences. *Marine georesources & geotechnology*, *13*(4), 375-391.

Kuhn, T., Bau, M., Blum, N., & Halbach, P. (1998). Origin of negative Ce anomalies in mixed hydrothermal–hydrogenetic Fe–Mn crusts from the Central Indian Ridge. *Earth and Planetary Science Letters*, *163*(1-4), 207-220.

Larrasoaña, J. C., Liu, Q., Hu, P., Roberts, A. P., Mata, P., Civis, J., ... & Pérez-Asensio, J. N. (2014). Paleomagnetic and paleoenvironmental implications of magnetofossil occurrences in late Miocene marine sediments from the Guadalquivir Basin, SW Spain. *Frontiers in microbiology*, *5*, 71.

Liu, Q., Roberts, A. P., Larrasoana, J. C., Banerjee, S. K., Guyodo, Y., Tauxe, L., & Oldfield, F. (2012). Environmental magnetism: principles and applications. *Reviews of Geophysics*, *50*(4).
Manheim, F. T., & Lane-Bostwick, C. M. (1988). Cobalt in ferromanganese crusts as a monitor of hydrothermal discharge on the Pacific sea floor. *Nature*, *335*(6185), 59-62.

Marino, E., González, F. J., Kuhn, T., Madureira, P., Wegorzewski, A. V., Mirao, J., ... & Lunar, R. (2019). Hydrogenetic, diagenetic and hydrothermal processes forming ferromanganese

crusts in the Canary Island Seamounts and their influence in the metal recovery rate with hydrometallurgical methods. *Minerals*, *9*(7), 439.

Marino, E., González, F. J., Lunar, R., Reyes, J., Medialdea, T., Castillo-Carrión, M., ... & Somoza, L. (2018). High-resolution analysis of critical minerals and elements in Fe–Mn crusts from the Canary Island Seamount Province (Atlantic Ocean). *Minerals*, *8*(7), 285.

Marino, E., González, F. J., Somoza, L., Lunar, R., Ortega, L., Vázquez, J. T., ... & Bellido, E. (2017). Strategic and rare elements in Cretaceous-Cenozoic cobalt-rich ferromanganese crusts from seamounts in the Canary Island Seamount Province (northeastern tropical Atlantic). *Ore Geology Reviews*, *87*, 41-61.

Maxbauer, D. P., Feinberg, J. M., Fox, D. L., & Clyde, W. C. (2016). Magnetic minerals as recorders of weathering, diagenesis, and paleoclimate: A core–outcrop comparison of Paleocene–Eocene paleosols in the Bighorn Basin, WY, USA. *Earth and Planetary Science Letters*, *452*, 15-26.

Murad, E., & Schwertmann, U. (1988). Iron oxide mineralogy of some deep-sea ferromanganese crusts. *American Mineralogist*, *73*(11-12), 1395-1400.

Noguchi, A., Oda, H., Yamamoto, Y., Usui, A., Sato, M., & Kawai, J. (2017a). Scanning SQUID microscopy of a ferromanganese crust from the northwestern Pacific: Submillimeter scale magnetostratigraphy as a new tool for age determination and mapping of environmental magnetic parameters. *Geophysical Research Letters*, *44*(11), 5360-5367.

Noguchi, A., Yamamoto, Y., Nishi, K., Usui, A., & Oda, H. (2017b). Paleomagnetic study of ferromanganese crusts recovered from the northwest Pacific—Testing the applicability of the magnetostratigraphic method to estimate growth rate. *Ore Geology Reviews*, *87*, 16-24.

Oda, H., Katanoda, W., Usui, A., Murayama, M., & Yamamoto, Y. (2023). Rotation of a ferromanganese nodule in the Penrhyn Basin, South Pacific, tracked by the Earth's magnetic field. *Geochemistry, Geophysics, Geosystems*, *24*(3), e2022GC010789.

Oda, H., Nakasato, Y., & Usui, A. (2018). Characterization of marine ferromanganese crust from the Pacific using residues of selective chemical leaching: identification of fossil magnetotactic bacteria with FE-SEM and rock magnetic methods. *Earth, Planets and Space*, *70*(1), 1-10.

Oda, H., Usui, A., Miyagi, I., Joshima, M., Weiss, B. P., Shantz, C., ... & Baudenbacher, F. J. (2011). Ultrafine-scale magnetostratigraphy of marine ferromanganese crust. *Geology*, *39*(3), 227-230.

Palomino, D., Vázquez, J. T., Somoza, L., León, R., López-González, N., Medialdea, T., ... & Rengel, J. A. (2016). Geomorphological features in the southern Canary Island Volcanic Province: The importance of volcanic processes and massive slope instabilities associated with seamounts. *Geomorphology*, *255*, 125-139

Pattan, J. N., & Mudholkar, A. V. (1991). Mössbauer studies and oxidized manganese ratio in ferromanganese nodules and crusts from the Central Indian Ocean. *Geo-marine letters*, *11*, 51-55.

Praxedes, A. G. P., de Castro, D. L., Torres, L. C., Gambôa, L. A. P., & Hackspacher, P. C. (2019). New insights of the tectonic and sedimentary evolution of the Rio Grande Rise, South Atlantic Ocean. *Marine and Petroleum Geology*, *110*, 335-346.

Roberts, A. P. (2015). Magnetic mineral diagenesis. *Earth-Science Reviews*, *151*, 1-47.

Roberts, A. P., Florindo, F., Villa, G., Chang, L., Jovane, L., Bohaty, S. M., ... & Gerald, J. D. F. (2011). Magnetotactic bacterial abundance in pelagic marine environments is limited by organic carbon flux and availability of dissolved iron. *Earth and Planetary Science Letters*, *310*(3-4), 441-452.

Rodelli, D., Jovane, L., Giorgioni, M., Rego, E. S., Cornaggia, F., Benites, M., ... & Roberts, A. P. (2019). Diagenetic fate of biogenic soft and hard magnetite in chemically stratified sedimentary environments of Mamanguá Ría, Brazil. *Journal of Geophysical Research: Solid Earth*, *124*(3), 2313-2330.

Rodelli, D., Jovane, L., Roberts, A. P., Cypriano, J., Abreu, F., & Lins, U. (2018). Fingerprints of partial oxidation of biogenic magnetite from cultivated and natural marine magnetotactic bacteria using synchrotron radiation. *Environmental microbiology reports*, *10*(3), 337-343.

Rusanov, V., Chakarova, K., & Trautwein, A. X. (2008). On the possibility to use stratabound hydrothermal crusts as indicators for local or global changes in the environment. *Journal of atmospheric and solar-terrestrial physics*, *70*(2-4), 285-292.

Sarmiento, J. L., Gruber, N., Brzezinski, M. A., & Dunne, J. P. (2004). High-latitude controls of thermocline nutrients and low latitude biological productivity. *Nature*, *427*(6969), 56-60.

Savelyev, D. P., Savelyeva, O. L., Moskaleva, S. V., & Rashidov, V. A. (2022). Composition of Cosmic Spherules from Ferromanganese Crusts of the Magellan Seamounts. *Geochemistry International*, *60*(5), 411-420.

Sergipe, P. P., Louro, V., Marangoni, Y. R., de Moura, D. S., & Jovane, L. (2023). A study of volcanic rocks and ferromanganese crusts through marine geophysical methods integration in the north portion of Cruzeiro do Sul Rift in the Rio Grande Rise. *Frontiers in Marine Science*.

Sousa, I. M. C., Santos, R. V., Koschinsky, A., Bau, M., Wegorzewski, A. V., Cavalcanti, J. A. D., & Dantas, E. L. (2021). Mineralogy and chemical composition of ferromanganese crusts from the Cruzeiro do Sul Lineament-Rio Grande Rise, South Atlantic. *Journal of South American Earth Sciences*, 103207.

Staszak, P., Collot, J., Josso, P., Pelleter, E., Etienne, S., Patriat, M., ... & Guyomard, Y. (2022). Origin and Composition of Ferromanganese Deposits of New Caledonia Exclusive Economic Zone. *Minerals*, *12*(2), 255.

Stumm, W., Morgan, J. J., & Drever, J. I. (1996). Aquatic chemistry. *Journal of environmental quality*, *25*(5), 1162.

Templeton, A. S., Knowles, E. J., Eldridge, D. L., Arey, B. W., Dohnalkova, A. C., Webb, S. M., ... & Staudigel, H. (2009). A seafloor microbial biome hosted within incipient ferromanganese crusts. *Nature Geoscience*, *2*(12), 872-876.

Usui, A., & Someya, M. (1997). Distribution and composition of marine hydrogenetic and hydrothermal manganese deposits in the northwest Pacific. *Geological Society, London, Special Publications*, *119*(1), 177-198.

Usui, A., Graham, I. J., Ditchburn, R. G., Zondervan, A., Shibasaki, H., & Hishida, H. (2007). Growth history and formation environments of ferromanganese deposits on the Philippine Sea Plate, northwest Pacific Ocean. *Island Arc*, *16*(3), 420-430.

Usui, A., Nishi, K., Sato, H., Nakasato, Y., Thornton, B., Kashiwabara, T., ... & Urabe, T. (2017). Continuous growth of hydrogenetic ferromanganese crusts since 17 Myr ago on Takuyo-Daigo Seamount, NW Pacific, at water depths of 800–5500 m. *Ore Geology Reviews*, *87*, 71-87.

Varentsov, I. M., Drits, V. A., Gorshkov, A. I., Sivtsov, A. T., & Sakharov, B. A. (1991). Mn-Fe oxyhydroxide crusts from Krylov Seamount (eastern Atlantic): Mineralogy, geochemistry and genesis. *Marine Geology*, *96*(1-2), 53-70.

Xu, X., Qiang, X., Zhao, H., & Fu, C. (2020). Magnetic mineral dissolution recorded in a lacustrine sequence from the Heqing Basin, SW China, and its relationship with changes in the Indian monsoon. *Journal of Asian Earth Sciences*, *188*, 104081.

Yamazaki, T. (2020). Reductive dissolution of biogenic magnetite. *Earth, Planets and Space*, *72*(1), 1-9.

Yamazaki, T., & Ikehara, M. (2012). Origin of magnetic mineral concentration variation in the Southern Ocean. *Paleoceanography*, *27*(2).

Yi, L., Medina-Elizalde, M., Kletetschka, G., Yao, H., Simon, Q., Paterson, G. A., ... & Zhu, R. (2020). The potential of marine ferromanganese nodules from Eastern Pacific as recorders of Earth's magnetic field changes during the past 4.7 Myr: A geochronological study by magnetic scanning and authigenic 10Be/9Be dating. *Journal of Geophysical Research: Solid Earth*, *125*(7), e2019JB018639.

Yi, L., Medina-Elizalde, M., Tan, L., Kemp, D. B., Li, Y., Kletetschka, G., ... & Ogg, J. G. (2023). Plio-Pleistocene deep-sea ventilation in the eastern Pacific and potential linkages with Northern Hemisphere glaciation. *Science Advances*, *9*(8), eadd1467.

Yuan, W., Zhou, H., Yang, Z., Hein, J. R., & Yang, Q. (2020). Magnetite magnetofossils record biogeochemical remanent magnetization in hydrogenetic ferromanganese crusts. *Geology*, *48*(3), 298-302.

Yuan, W., Zhou, H., Zhao, X., Yang, Z., Yang, Q., & Zhu, B. (2017). Magnetic stratigraphic dating of marine hydrogenetic ferromanganese crusts. *Scientific Reports*, *7*(1), 16748.

Supplementary material

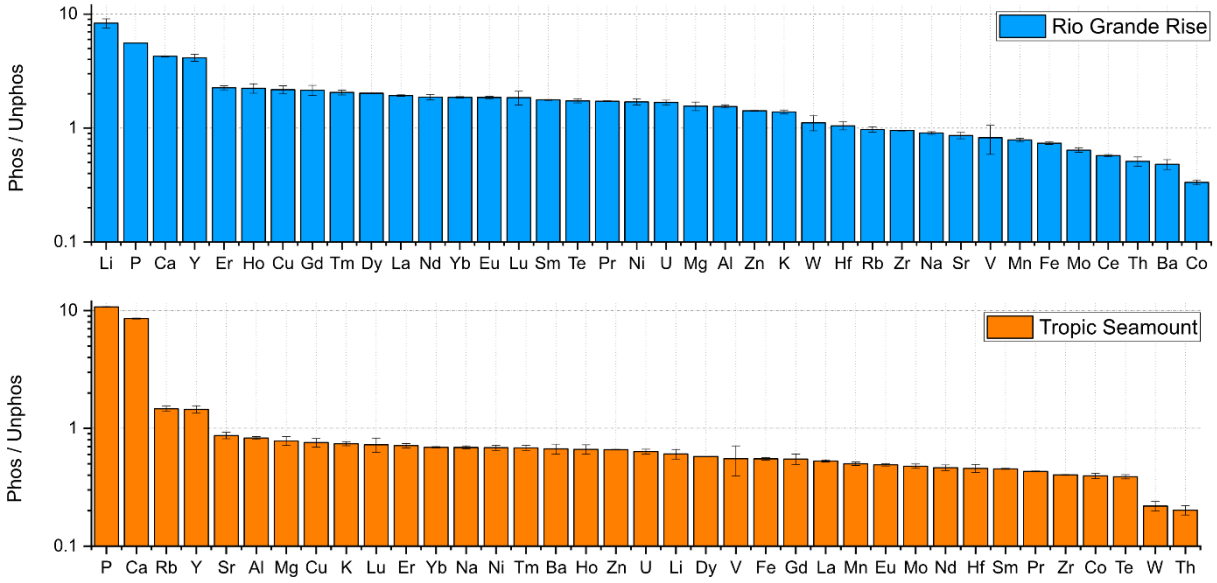

Fig.S1: Phosphatized to non-phosphatized elemental ratio in FeMn crust samples: Blue: For RGR, n =13, Brown for TS, n = 8. The data clearly shows the decrease of the FeMn phase in the phosphatized crusts and an increase of some major (P, Ca) and many trace elements in phosphatized crusts, especially from RGR.

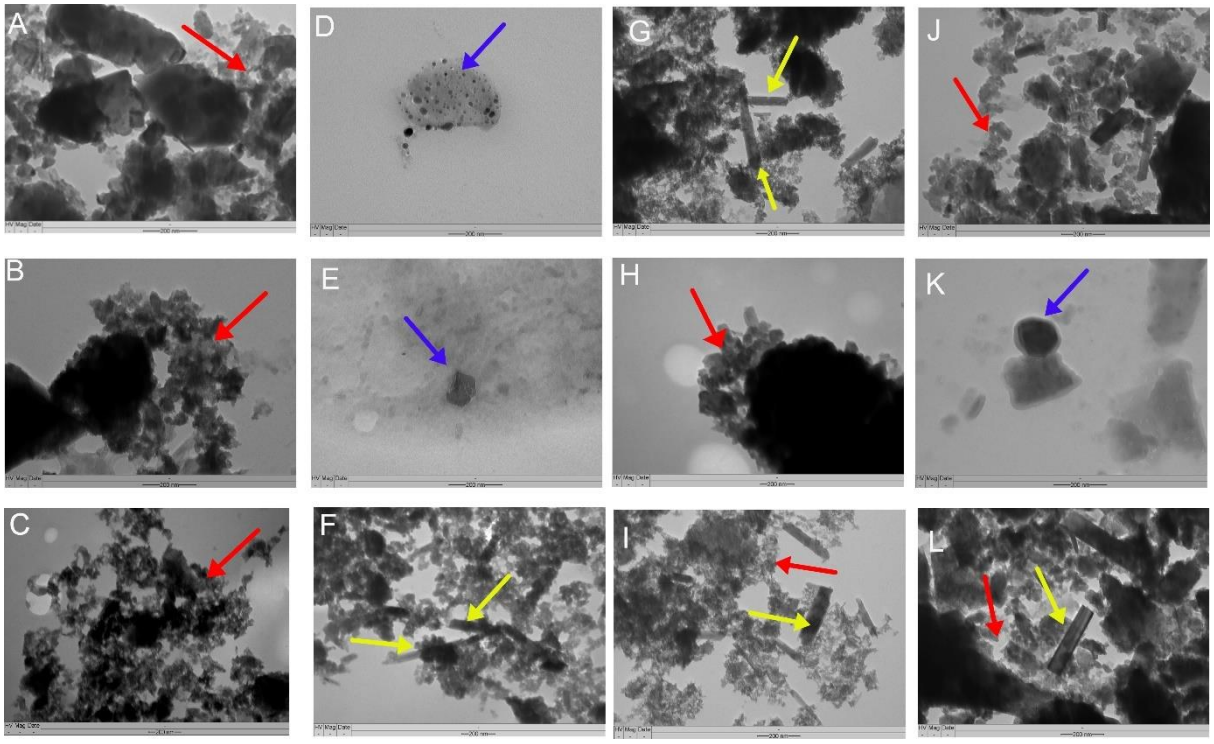

Fig.S2: Transmission Electron Microscopy of magnetic extract: A, B, C- Non-phosphatized sample from RGR (RGR1-D07-002), representing amorphous Fe oxyhydroxide phase (red arrow) D, E, F- Phosphatized sample from RGR, blue arrows indicate magnetite hexagonal crystals facing suboxic dissolution, yellow arrows indicate poorly crystalline goethite crystals, G, H, I- Non-phosphatized sample from TS (JC142-085-001), representing amorphous Fe oxyhydroxide phase (red arrow) J, K, L- Phosphatized sample from TS, blue arrows indicate magnetite hexagonal crystals facing suboxic dissolution, yellow arrows indicate poorly crystalline goethite crystals.

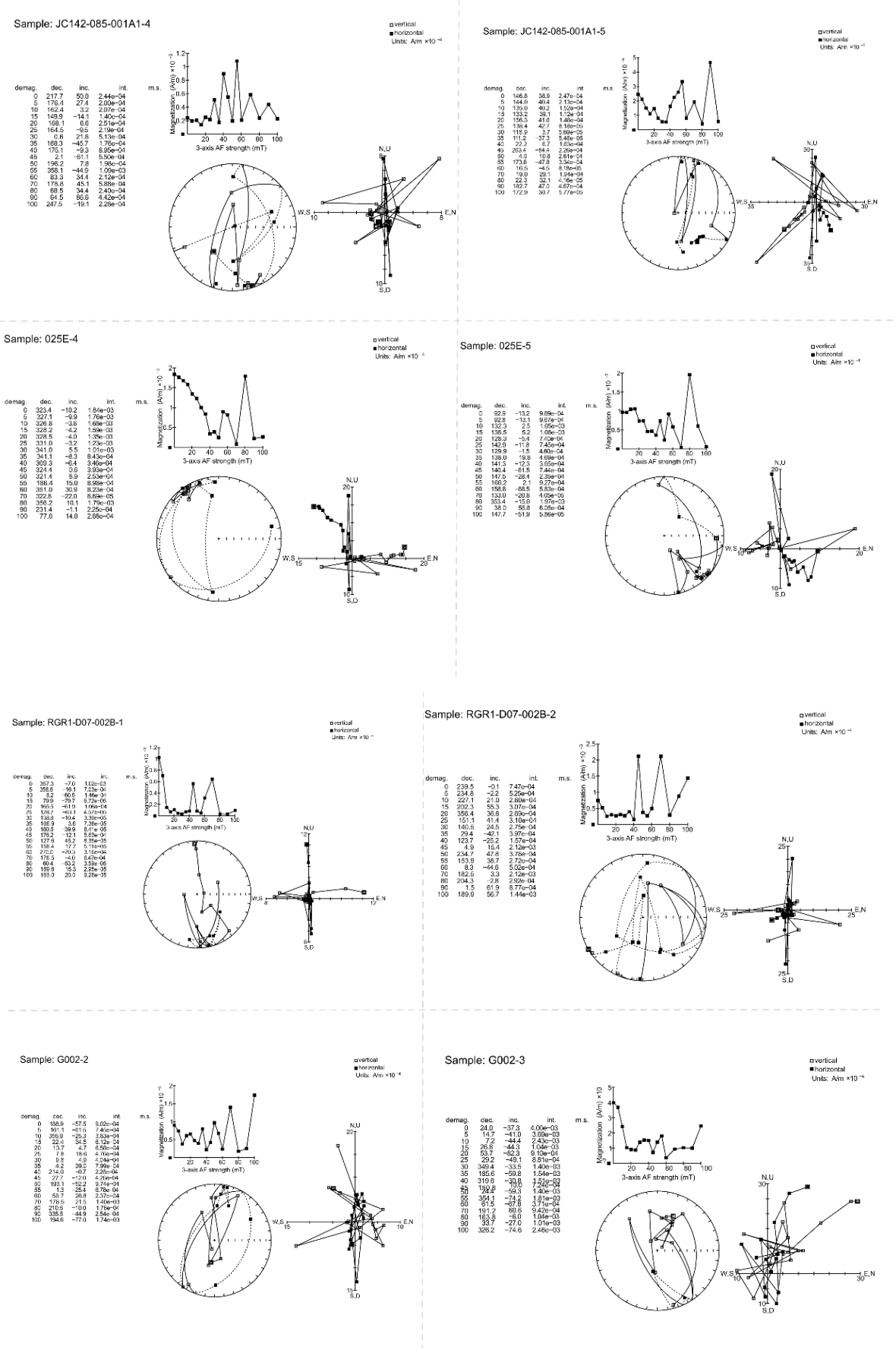

Fig.S3: Demagnetization and *Zijderveld diagrams*: Demagnetization behaviour of selected thinly cut sliced samples from RGR and TS representing vague and unreliable data.

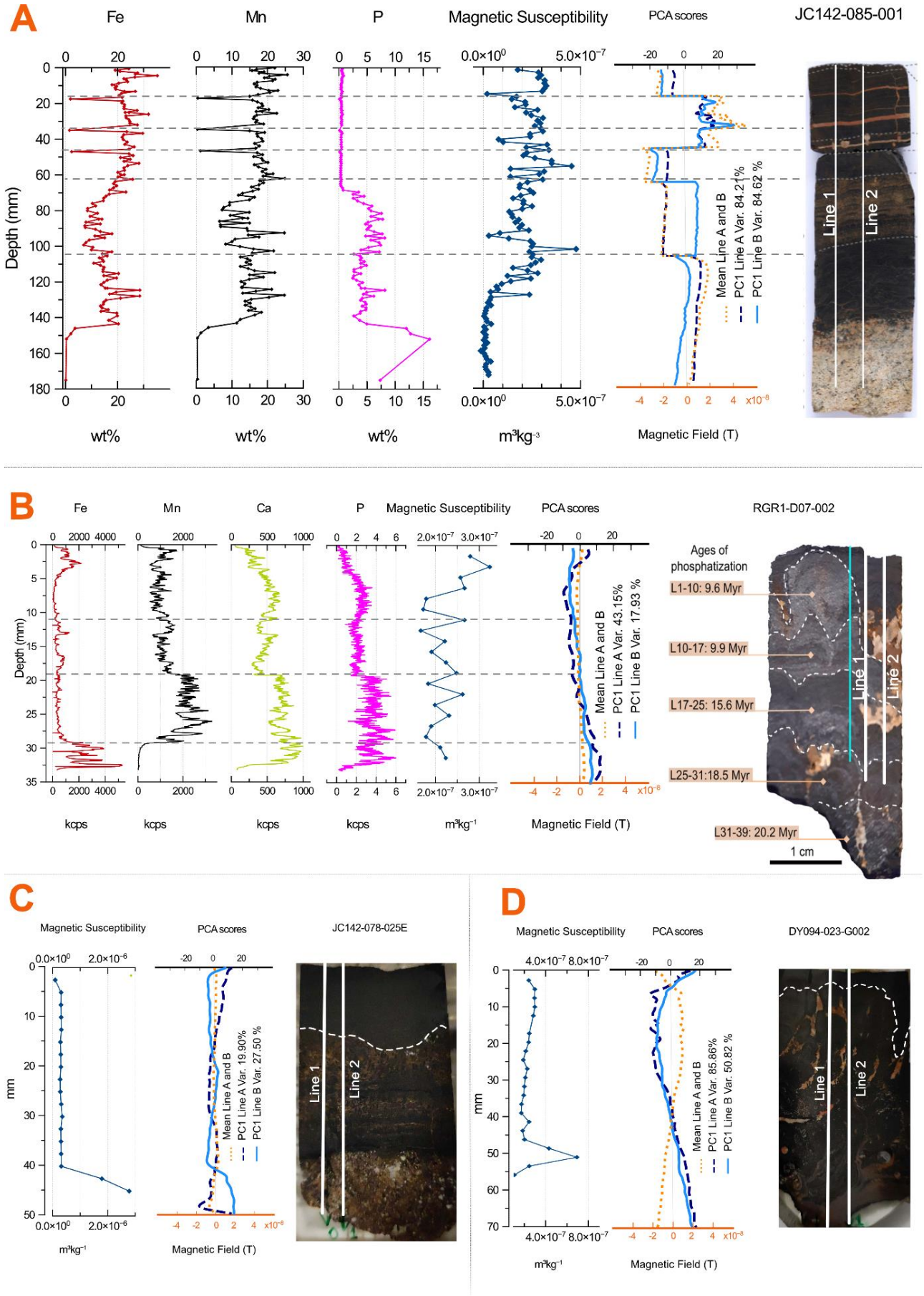

Fig.S4: Geochemical vs magnetic data along the crust samples from RGR and TS: A- Sample JC142-

085-001 from TS, The continuous data for Fe, Mn and P was taken from Josso et al. (2019); the magnetic susceptibility was measured in discrete thin slice samples, PCA score was obtained from the Hall probe magnetic scanning for 2 lines, Line A and B, and the mean of both lines is also shown in yellow dotted line; B- Sample RGR1-D07-002 from RGR, The continuous data for Fe, Mn, Ca and P was taken from Benites et al. (2020); the magnetic susceptibility was measured in discrete thin slice samples, PCA score was obtained from the Hall probe magnetic scanning for 2 lines, Line A and B, and the mean of both lines is also shown in yellow dotted line; C- Sample JC142-078-025E from TS, The magnetic susceptibility was measured in discrete thin slice samples, PCA score was obtained from the Hall probe magnetic scanning for 2 lines, Line A and B, and the mean of both lines is also shown in yellow dotted line; D- Sample DY094-023-G002 from RGR, The magnetic susceptibility was measured in discrete thin slice samples, PCA score was obtained from the Hall probe magnetic scanning for 2 lines, Line A and B, and the mean of both lines is also shown in yellow dotted line.

4 CARBON SEQUESTRATION ASSESSMENT USING VARYING CONCENTRATIONS OF MAGNETOTACTIC BACTERIA (CHAPTER 3)

Manuscript published in *Environmental Advances*

Muhammad Bin Hassan[a,b], Luigi Jovane[a], Anderson de Souza Cabral[c], Fernanda Abreu[c], Natascha Menezes Bergo[a], Vivian Pellizari[a]

[a]Instituto Oceanográfico, Universidade de São Paulo, São Paulo, Brazil

[b]Department of Physics & Earth Sciences, Jacobs University Bremen, Bremen, Germany

[c]Instituto de Microbiologia Paulo de Góes, Universidade Federal do Rio de Janeiro, Brazil

Abstract

Carbon cycling processes on Earth are many and complex, and several continental and oceanic environments remain poorly studied. Consequently, major uncertainties affect carbon-cycling models which limit our ability to understand and predict climate dynamics. The first assessment of carbon sequestration for magnetotactic bacteria (MTB) was carried out in this study. MTB produce magnetosomes which are intracellular organelles containing nanometer-sized, membrane-bound magnetite crystals. These crystals are arranged into single or multiple chains within the cell, which enable MTB to align themselves along a magnetic field (magnetotaxis). MTB are well known in the biological sciences, and their magnetic remains are widely studied in earth sciences as magnetofossils. Rock magnetic techniques provide indirect and non-destructive identification of magnetosomes in a sample. It is very crucial to understand the magnetic response of different types of magnetosomes produced by distinct MTB species with varying concentrations. Magnetic properties of lysed and whole MTB cells, the cultured *Magnetovibrio blakemorei* strain MV-1^T and *Magnetofaba australis* strain IT-1, with concentrations varying from 10^2 to 10^9 per sample are presented here. Magnetic properties of quantified bacterial magnetite depend largely on the quantity of MTB cells rather than on the bacterial species or cell type (lysed or whole). Magnetic values are significantly higher for the samples containing 10^7 cells or higher, FORC diagrams have no measurable magnetic fingerprint for the samples containing less than 10^7 cells. Therefore, unmeasurable magnetic signals may compromise detection of lower magnetic particle concentrations in a sample. This study estimates the carbon content of MTB cells and discusses its relationship to the global carbon cycle.

4.1 Introduction

Earth's carbon cycle is complex and involves multiple factors and processes over various time scales (Raymo and Ruddiman, 1993; Tajika, 1998; Kump and Arthur, 1999; Kolber et al., 2001; Berner, 2003; Key et al., 2004; Hayes and Waldbauer, 2006; Lechtenfeld et al., 2015). Its study is fundamental to understanding natural balances and dynamics. It has drawn more attention over recent decades, especially since the realization that human activities have been transferring large amounts of carbon from the geological to the atmospheric and oceanic reservoirs at a rapid rate. To confidently evaluate the impact of carbon cycle perturbations on natural ecosystems, it is fundamental to understand the complexity of carbon fluxes and constraints of the net carbon balance in natural ecosystems. However, we lack estimates of carbon burial into sediments from bacteria which is related to the difficulty of calculating bacterial abundances in the sediments throughout the geological timescale. MTB are bacteria that produce and preserve magnetite, and can be detected in sediment layers after burial, which provides information on environmental conditions at the time when they were alive. MTB occur widely in different environments (Lefèvre and Bazylinski, 2013; Abreu et al., 2016), so they are important not only in Earth sciences, but also in other fields ranging from physics to medical science (Yan et al., 2012; Dasdag, 2014). MTB produce magnetosomes which are intracellular organelles that contain membrane enclosed nano-sized crystals of magnetic minerals, particularly magnetite (Faivre and Schüler, 2008; Frankel, 2009). These crystals are generally arranged in one or multiple chain-like structures that enable the MTB to align themselves along an external magnetic field. This alignment with the magnetic field and migration propelled by flagella is termed as 'magnetotaxis' (Yan et al., 2012). MTB occurrences are often related to environments with redox gradients in stratified water/sediment columns (Bazylinski and Frankel, 2004; Roberts et al., 2011, 2012; Rodelli et al., 2018, 2019; Yamazaki et al., 2019). Most MTB prefer to live in microaerophilic environments, specifically across the oxic-anoxic transition zone (OATZ) (Frankel and Bazylinski, 2006).

MTB are a diverse group of bacteria with a distinctive morphology of magnetic particles and specific ecology and genetics (Chang et al., 2012; Lin et al., 2017). MTB can be found in lakes, sediments, soils, and marine water (Bazylinski et al., 2007; Dong et al., 2016; Lin et al., 2017). After bacterial death, magnetosomal magnetic particles are preserved as magnetofossils (Kopp and Kirschvink, 2008; Goswami et al., 2022). Magnetofossils have been studied widely in the field of geosciences due to their paleomagnetic and paleoenvironmental implications (Larrasoaña et al., 2014; Savian et al., 2014; 2016; Frontalini et al., 2016; Giorgioni et al., 2019; Coccioni et al., 2019; Hassan et al., 2020). Magnetofossils have also been found in Fe-Mn

nodules, crusts, and corals from the Pacific and Indian Oceans (Lund et al., 2010; Oda et al., 2018; Hassan et al., 2020; Jiang et al., 2020; Yuan et al., 2020). Moreover, magnetofossils in sediments and sedimentary rocks provide information about paleoenvironmental conditions (Yamazaki and Kawahata, 1998; Yamazaki, 2009; Lu et al., 2021). Varying magnetofossil morphologies and abundances can also be due to microenvironmental stratification in sediments (Usui et al., 2017; Rodelli et al., 2019).

The cultivated MTB strains are affiliated to the phylum Proteobacteria, mainly in the Alphaproteobacteria class whose known representatives are *Magnetospirillum magnetotacticum* strain MS-1 (Maratea and Blakemore, 1981), *M. gryphiswaldense* strain MSR-1 (Schleifer et al., 1991), and *M. magneticum* strain AMB-1 (Matsunaga et al., 1991). Recently magnetotactic cocci, previously affiliated as Alphaproteobacteria, such as the three marine cocci, *Magnetococcus marinus* strain MC-1 (Bazylinski et al., 2013a), *Magnetococcus massalia* strain MO-1 (Lefèvre et al., 2009) and *Magnetofaba australis* strain IT-1 (Morillo et al., 2014) were reclassified as *Candidatus Etaproteobacteria* class (Lin et al., 2018). These MTB have versatile metabolism which produce prismatic, cuboctahedral and elongated octahedral magnetic particles (Bazylinski et al., 2013b; Morillo et al., 2014).

Magnetic methods provide rapid, non-destructive techniques for detecting the presence of MTB or magnetofossils (Moskowitz et al., 1993; Weiss et al., 2004; Egli et al., 2010; Roberts et al., 2012; Chang et al., 2014, 2016). Magnetosomal magnetic particles have characteristic magnetic fingerprints that can be detected as non-interacting single-domain (SD) particles using non-destructive magnetic techniques (Moskowitz et al., 1993; Jovane et al., 2012). Many magnetic features of biogenic magnetite have been detected in recent studies (e.g., Heslop et al. 2013, Berndt et al. 2020).

In a bulk sediment sample, magnetofossils are commonly identified using magnetic measurements such as hysteresis loop, isothermal remanent magnetization (IRM) curves and most importantly first-order reversal curve (FORCs) diagrams. FORCs are used commonly to differentiate magnetic minerals from different sources (Chen et al., 2007; Egli et al., 2010; Roberts et al., 2012). For the direct identification of magnetosomal magnetite and the morphology, microscopic studies such as high-resolution transmission electron microscopy (HRTEM) are considered essential (Kopp and Kirschvink, 2008). Data derived from coupled direct and indirect methods are correlated to other geochemical and paleomagnetic data to establish paleoenvironmental interpretations (Chang et al., 2018). Berndt et al. (2020) detailed the relation of magnetosomal magnetite morphologies to their individual magnetic signatures.

Previously, Faivre et al. (2007) suggested that carbon plays no important role in the production of magnetosomes. However, Staniland et al. (2007) later concluded that carbon-rich environments speed up magnetosome synthesis. Gareev et al. (2021) described the magnetic properties of magnetosomes produced by *Magnetospirillum caucaseum* strain SO-1 and a noticeable contrast between the magnetic properties of isolated, non-interacting single-domain particles of magnetite and preserved magnetosome chains. So far, many microorganisms and bacteria have been linked to the dissolved organic carbon flux in marine environments (Sarmento and Gasol, 2012; Ribeiro et al., 2016; Bergo et al., 2017; De Martini et al., 2018).

We hypothesize that varying concentrations of whole and lysed bacterial cells produced by two distinct species would provide clues about the detection limit of rock magnetic methods and the relationship between magnetic properties and number of bacterial cells. Moreover, the calculations for the carbon content stored in bacterial cells would initiate discussions on global carbon cycling processes. There have also been no studies on the detection limit of rock magnetic methods based on the number of MTB or magnetic nanoparticles in sediment/rock samples. The magnetic results for variable concentrations of the cultivated species *Magnetofaba australis* strain IT-1 and *Magnetovibrio blakemorei* strain MV-1^T are reported here. The amount of carbon content stored in MTB cells is also estimated in this study.

4.2 Materials and methods

4.2.1 Sample preparation

Magnetovibrio blakemorei strain MV-1^T and *Magnetofaba australis* strain IT-1 were grown in heterotrophic media as described previously (Silva et al., 2013; ; Morillo et al., 2014). Cells were diluted to final concentrations of 10^9, 10^7, 10^4 and 10^2 cells/sample and transferred to 1.5 mL polypropelene tubes. Samples were also prepared by mixing the following concentrations: 10^9 cells of strain MV-1^T plus 10^7 cells of strain IT-1; 10^4 cells of strain MV-1^T plus 10^4 cells of strain IT-1; and 10^2 cells of strain MV-1^T plus 10^2 cells of strain IT-1 before fixation. For whole cell analysis, cells were directly fixed in 2.5% glutaraldehyde in sodium cacodylate buffer (0.1 M) separately. All samples were centrifuged at 12,000 g for 10 min and the total volume was reduced to 20 mL. To obtain disrupted cells, in which magnetosome chain organization would be lost, *Mv. blakemorei* strain MV-1^T and *Mf. australis* strain IT-1 samples at the same concentrations as mentioned above were submitted to an ultrasonic cell crusher before fixation (VCX 500, Sonics, Newtown, CT, USA) at 40% amplitude, 20 kHz frequency, in 60 cycles of 30 s between intervals of 30 s. Each sample was included in 1%

agarose to avoid losing cells or their content during sample processing. After solidification of the agarose plug, all samples were washed in the same buffer, dehydrated in acetone series (30%, 50%, 70%, 90% and 100%) and embedded in PolyBed 812 resin. Resin blocks of each sample were directly analyzed by magnetic measurements.

Samples were named *Magnetovibrio blakemorei* = MV, *Magnetofaba australis* = IT, L = lysed samples and absence of L indicates a whole sample. A digit between sample names indicates the cell concentration. For example, IT2 is *Magnetofaba australis* with a 10^2 concentration for the whole cell while IT2L is the lysed equivalent of the same sample.

4.2.2 Transmission electron microscopy (TEM)

Ultrathin sections of the resin blocks corresponding to the maximum number of cells were obtained using a Leica EM U6 ultramicrotome (Leica Microsystems, Wetzlar, Germany) and were stained with uranyl acetate and lead citrate. Samples were observed on a FEI Morgagni transmission electron microscope (FEI Company, Hillsboro, USA) operating at 80 kV. Images of *Magnetovibrio blakemorei* strain MV-1^T and *Magnetofaba australis* strain IT-1 were obtained by whole cell observation or by applying osmium tetroxide post-fixation after glutaraldehyde fixation (Abreu et al., 2013), respectively (Fig. 1).

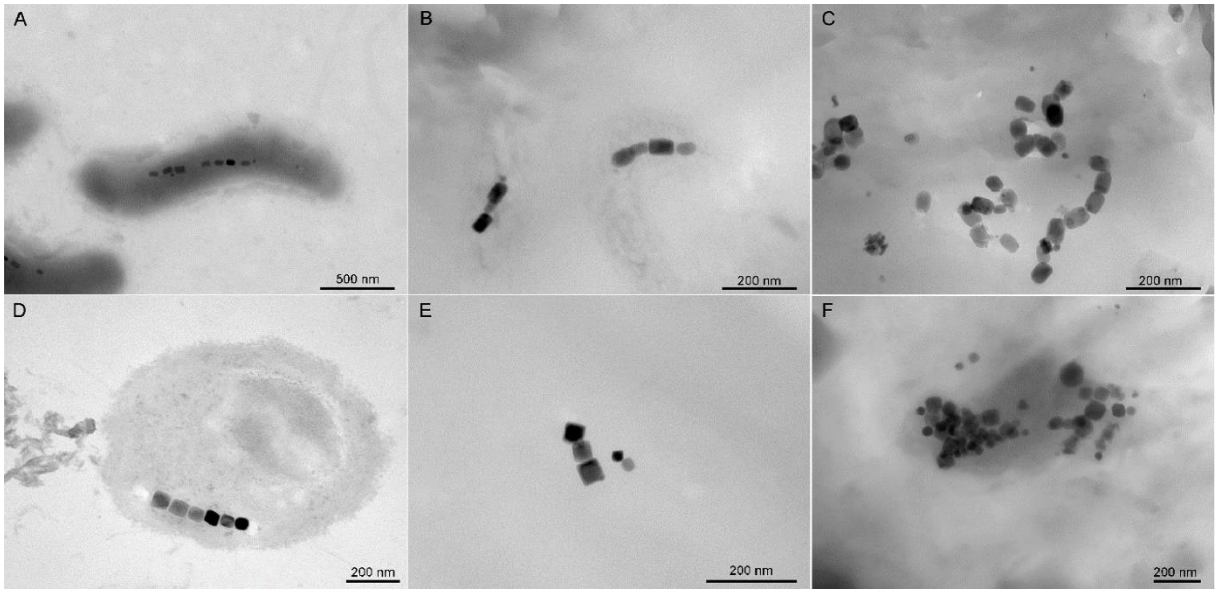

Fig. 1. Transmission electron microscopy images of; **A:** Whole cell preparation of *Magnetovibrio blakemorei* strain MV-1^T showing the cell shape and the magnetosome chain; B: FORC sample corresponding to 10^9 cells of *Mv. blakemorei* strain MV-1^T showing two intact cells; C: FORC sample corresponding to 10^9 cells of *Mv. blakemorei* strain MV-1^T submitted to ultrasonic cell crusher; D: Stained ultrathin section of *Magnetofaba australis* strain IT-1 showing the cell shape and the magnetosome chain; E: FORC sample corresponding to 10^7 cells of *Mf. australis* strain IT-1; F: FORC sample corresponding to 10^7 cells of *Mf. australis* strain IT-1 submitted to ultrasonic cell crusher.

4.2.3 Magnetic methods

All resin samples were subjected to magnetic measurements by using an alternating gradient magnetometer (AGM MicroMagTM 2900) at the Centro Oceanográfico de Registros Estratigráficos (CORE), Instituto Oceanográfico, Universidade de São Paulo (IOUSP). Since this study is focused on magnetic method sensitivity, all measurements were carried out using an alternating gradient magnetometer (AGM).

Hysteresis loops and FORCs were measured at room temperature for each sample. Hysteresis parameters such as the saturation magnetization (M_s), saturation remanent magnetization (M_{rs}), and magnetic coercivity were obtained from hysteresis loops measured at a maximum applied field of 500 mT. Hysteresis loops were processed and plotted using the HystLab software of Paterson et al. (2018). Hysteresis loops were further processed to obtain the remanence hysteresis curves (M_{rh}) which give the reflection symmetry about the vertical axis and induced hysteretic curves (M_{ih}) which give the rotation symmetry about the origin of a hysteresis loop (von Dobeneck, 1996).

FORC diagrams are obtained by measuring a series of partial hysteresis curves, which provide contour plots of the second derivative of magnetic fields B_c and B_u, where B_c is the magnetic coercivity and B_u is the magnetostatic interaction field for uniaxial SD particles (Roberts et al., 2000). The dimension of magnetosomal magnetic crystals is optimized for SD magnetic behaviour. To produce a strong net magnetic anisotropy, the crystals align in a chain that behaves like a single long, non-interacting, SD particle (Dunin-Borkowski et al., 1998).

For FORC measurements, 297 curves were measured with an averaging time of 150 ms, in the space between Bc = 0–100 mT and Bu = 15 mT (Egli et al., 2010). The FORCs were processed using the FORCinel software provided by Harrison and Feinberg (2008). Variforc smoothing parameters were applied to smooth the FORCs signals (Egli, 2013). To represent the interaction field and coercivity distinction, horizontal and vertical profiles were produced. The same FORC diagrams were also produced with the new software “Forcot” and varying smoothing factors (SF) were applied to visualize FORC fingerprints for different samples (Berndt and Chang, 2019). The use of Forcot permits high resolution FORC features in seconds, which is 100 times faster than the FORCinel software.7

4.2.4 Carbon content in magnetotactic bacteria

Cellular carbon contents were estimated based on cell abundance and cell volume considerations for marine bacteria (Lee and Fuhrman, 1987). Cell abundance of *Mv. Blakemorei* strain MV-1^T and *Mf. Australis* strain IT-1 were prepared and analyzed according

to Gasol and Del Giorgio (2000) using a FacsCalibur flow cytometer (BD - Becton, Dickinson and Company, California, USA). Cells were quantified with standard optical configuration (air-cooled argon ion laser emitting at 488 nm, power 15 mW), laser alignment and optical components fixed, 70 µm nozzle, using Milli-Q water (18.2 mΩ) as carrier fluid, and FL1 530±15 nm (green), FL2 585±21 nm (orange) and FL3 670 nm LP (Red) channels with flow rate of 20 µL.min^{-1}. Fluorescent latex beads (Fluoresbrite YG carboxylate 1.0 µm Polysciences) were used as an internal standard for instrument verification. Water samples from the entrance of Guanabara Bay (Rio de Janeiro, RJ, Brazil) were used as a size standard for marine bacteria. MTB cell abundance (cell·L^{-1}) was converted to biomass (µgC·L^{-1}) using a constant cell-to-carbon conversion factor of 20 fg (Lee and Fuhrman, 1987).

Carbon content estimation for both MTB based on the volume-to-carbon relationship was done according to Norland et al. (1987) in which pgC cell^{-1} = 0.12 pg ($^{0.7}$µm^3 cell^{-1}). Carbon mass calculations considered the cell volume described in the literature for both species (Bazylinski et al., 2013b; Morillo et al., 2014). Cell volume (expressed in µm^3) is derived from the two-dimensional parameters (width = L, and length = C) obtained by image analysis, assuming that the cells are straight cylindrical rods with a hemisphere or, for coccoid forms, spheres. The volume of a single cell is calculated according to the geometrical formula described by Krambeck et al. (1981). Carbon biomass was obtained by multiplying the cell abundance by its corresponding cell carbon content derived from the volume obtained (La Ferla et al., 2012).

Individual morphometric analyses from micrographs of IT-1 and MV-1 bacteria were used to calculate the volume of each bacterium and to subsequently determine the specific carbon conversion factor to be used for each bacterium. For sample strain IT-1 and strain MV-1^T it was determined that each cell has 154.2 fg C cell^{-1} and 48.5 fg C cell^{-1}, respectively. Magnetite content estimation was based on the number, size, and shape of magnetite particles in *Mv. Blakemorei* strain MV-1^T and *Mf. Australis* strain IT-1 described for these species (Silva et al., 2013; Bazylinski et al., 2013b; Morillo et al., 2014).

4.3 Results and discussion

Hysteresis parameters obtained from the samples change abruptly e.g., M_s and M_{rs} for the defined sample type. M_{rs} values are low (near or below 0) for all samples except IT7, IT7L, ITMV9, ITMV9L, MV9 and MV9L which have high magnetite contents. M_s values are also high for these samples compared to those with concentrations less than 10^7 cells. Samples with higher values of M_s and M_{rs} are shaded in Fig. 2.

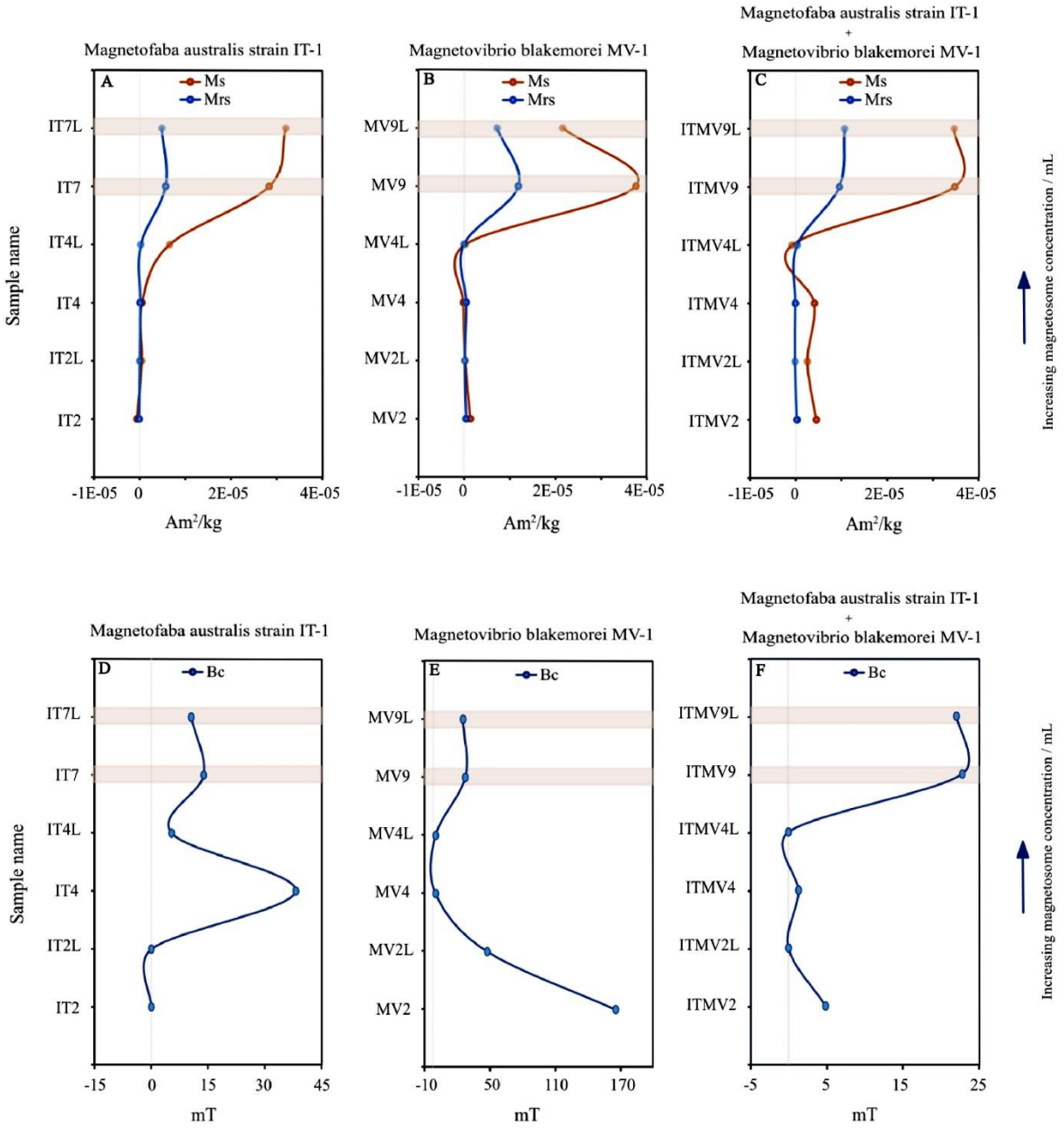

Fig. 2. Magnetic properties extracted from hysteresis cycles. A, B and C: Magnetic saturation (M_s) and Magnetic remanence of saturation (M_{rs}) and D, E and F: magnetic coercivity (B_c) curves for *Magnetofaba australis* strain IT-1, *Mv. blakemorei* strain MV-1^T and both species. Shaded points indicate the samples with the higher and FORC measurable concentrations of magnetic particles (i.e, 10^7/mL and above) as shown in Table. 1.

Table 1. The chart shows sample name, corresponding cell type, concentration of MTB cells/mL, Magnetic saturation (M_s), Magnetic remanence of saturation (M_{rs}) in Am^2/kg and Magnetic Coercivity (B_c) in mT. IT and MV in the sample name stand for *Magnetovibrio blakemorei* and *Magnetofaba Australis* respectively, the digit shows the concentration of cells/mL while the L identifies the lysed samples.

Name	Cell type	Number of cells/mL	Ms (Am^2/Kg)	Mr (Am^2/Kg)	Bc (mT)
IT2	Whole	10E+2	0	0	0
IT2L	Lysed	10E+2	4.78E-07	3.13E-08	0
IT4	Whole	10E+4	5.38E-07	1.30E-07	37.98
IT4L	Lysed	10E+4	6.59E-06	2.78E-07	5.34
IT7	Whole	10E+7	2.84E-05	5.71E-06	13.74
IT7L	Lysed	10E+7	3.20E-05	4.87E-06	10.46
ITMV2	Whole	2(10E+2)	4.48E-06	2.28E-07	4.90
ITMV2L	Lysed	2(10E+2)	2.53E-06	0	0
ITMV4	Whole	2(10E+4)	4.05E-06	0	1.33
ITMV4L	Lysed	2(10E+4)	0	2.81E-07	0
ITMV9	Whole	10E+9	3.48E-05	9.52E-06	22.88
ITMV9L	Lysed	10E+9	3.47E-05	1.07E-05	22.11
MV2	Whole	10E+2	1.36E-06	4.12E-07	165.86
MV2L	Lysed	10E+2	2.28E-07	1.41E-07	47.55
MV4	Whole	10E+4	0	4.28E-07	0
MV4L	Lysed	10E+4	2.85E-07	0	0
MV9	Whole	10E+9	3.76E-05	1.19E-05	27.36
MV9L	Lysed	10E+9	2.16E-05	7.19E-06	25.20

B_c values vary between 0 to 166 mT while samples IT7, IT7L, ITMV9, ITMV9L, MV9 and MV9L have coercivity values between 10.5 and 27.4 mT (Fig. 2). Hysteresis loops for samples IT7, IT7L, ITMV9, ITMV9L, MV9 and MV9L (cell number $\geq 10^7$) have diagnostic features in hysteresis loops while the corresponding M_{rh} and M_{ih} curves also represent the remanence-carrying magnetic nanoparticles in the samples (Fig. 3; A and B), with little to no remanence-carrying magnetic nanoparticles for samples with concentrations less than 10^7 cells (Fig. 3; C and D). FORC diagrams could only detect data for the samples IT7, IT7L, ITMV9, ITMV9L, MV9 and MV9L, while the other samples have no measurable FORC fingerprint. FORC diagrams for samples with mixtures of two species ITMV9 have a broader coercivity distribution as shown in the horizontal profiles (Fig. 4). High-resolution FORC diagrams have a distinctive feature for the lysed samples. Interactions among magnetic nanoparticles increased

at the lower coercivity edges of the FORC diagrams for the lysed cells samples (Li et al., 2013). These high-resolution FORC diagrams (Fig. 5, ITMV9) also contain two peaks for samples with mixtures of IT-1 and MV-1 species, which could represent two slightly different sizes and coercivities produced by the two different MTB species.

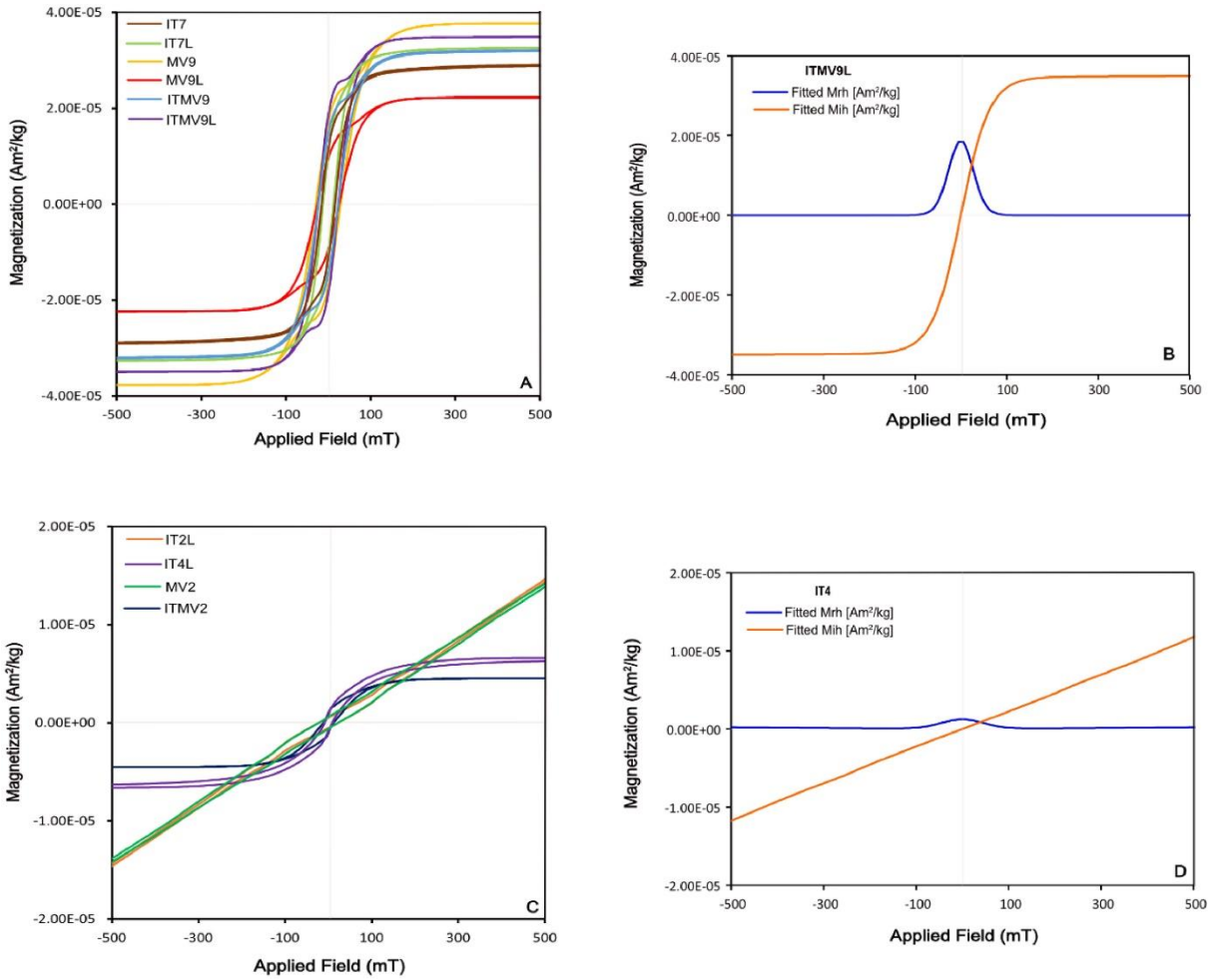

Fig. 3. A; Fitted Hysterisis cycles for the samples with the concentration 10^7/mL or more: **B**; Fitted Mrh and Mih curves for the representative sample ITMV9L: C; Fitted Hysterisis cycles for the representative samples with the concentration less than 10^7/mL as mentioned in the Table. 1: D; Fitted Mrh and Mih curves for the representative sample IT4.

Magnetizations are significantly higher for samples with 10^7 MTB cells or higher. Our data suggest that M_s, M_{rs} and B_c values notably depend on magnetic particle concentration. Although FORC diagrams are a valuable tool for detecting magnetic domain state as well as magnetic interactions among SD particles, they are also sensitive to the total number of magnetic particles within cells. Hence, unmeasurable magnetic signals could undermine detection of lower magnetic particle concentration in a sample.

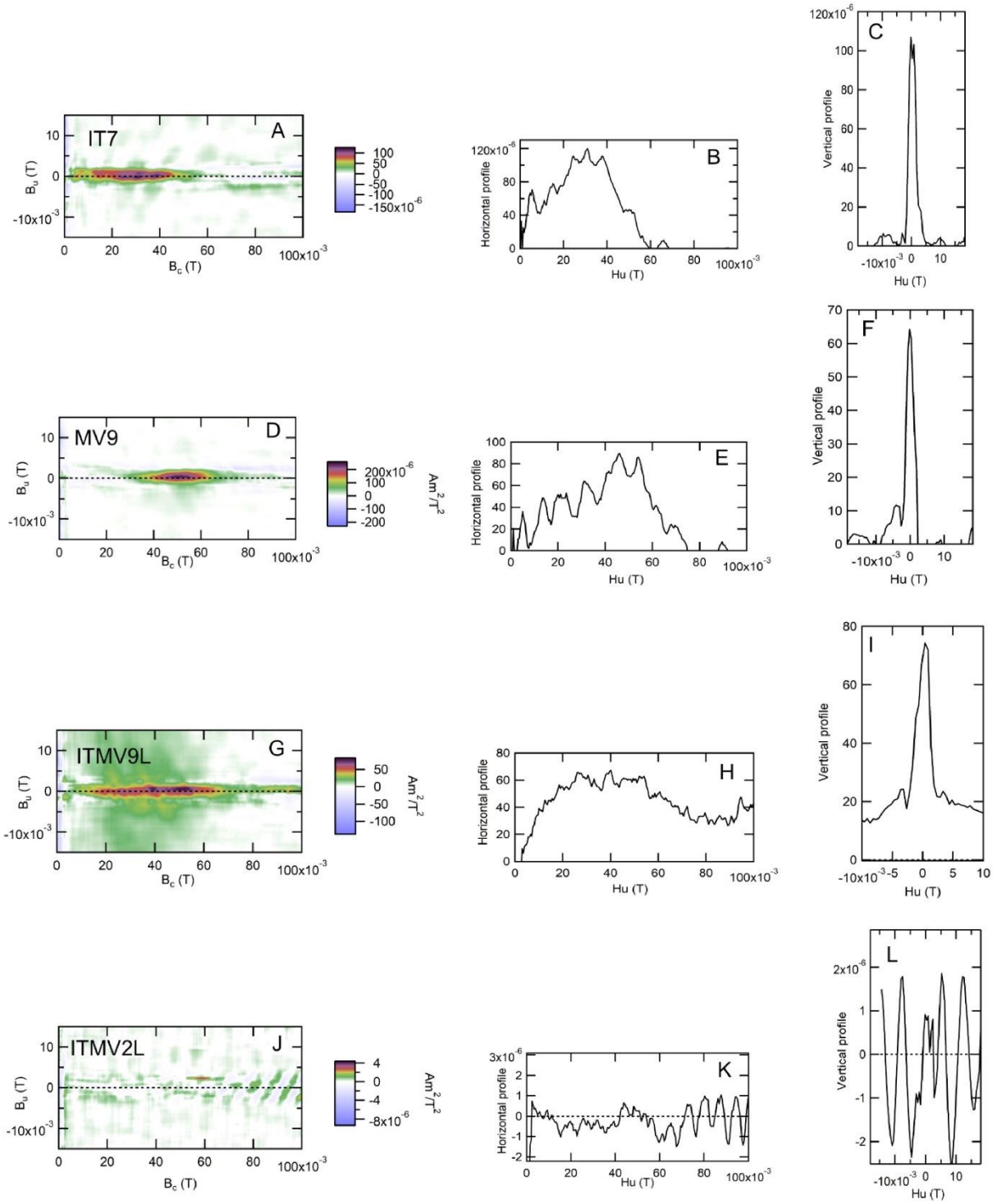

Fig. 4. First Order reversal Curve diagrams (**A-I)** for samples MV9, IT7, ITMV9L (magnetosomal magnetic particle concentration 10^7 and above. i.e, magnetically measurable) and **(J-L)** ITMV2L (magnetic particle concentration = 10^2 i.e, magnetically unmeasurable) with the respective horizontal (in the middle) and vertical profiles (on the left), processed by the FORCinel software.

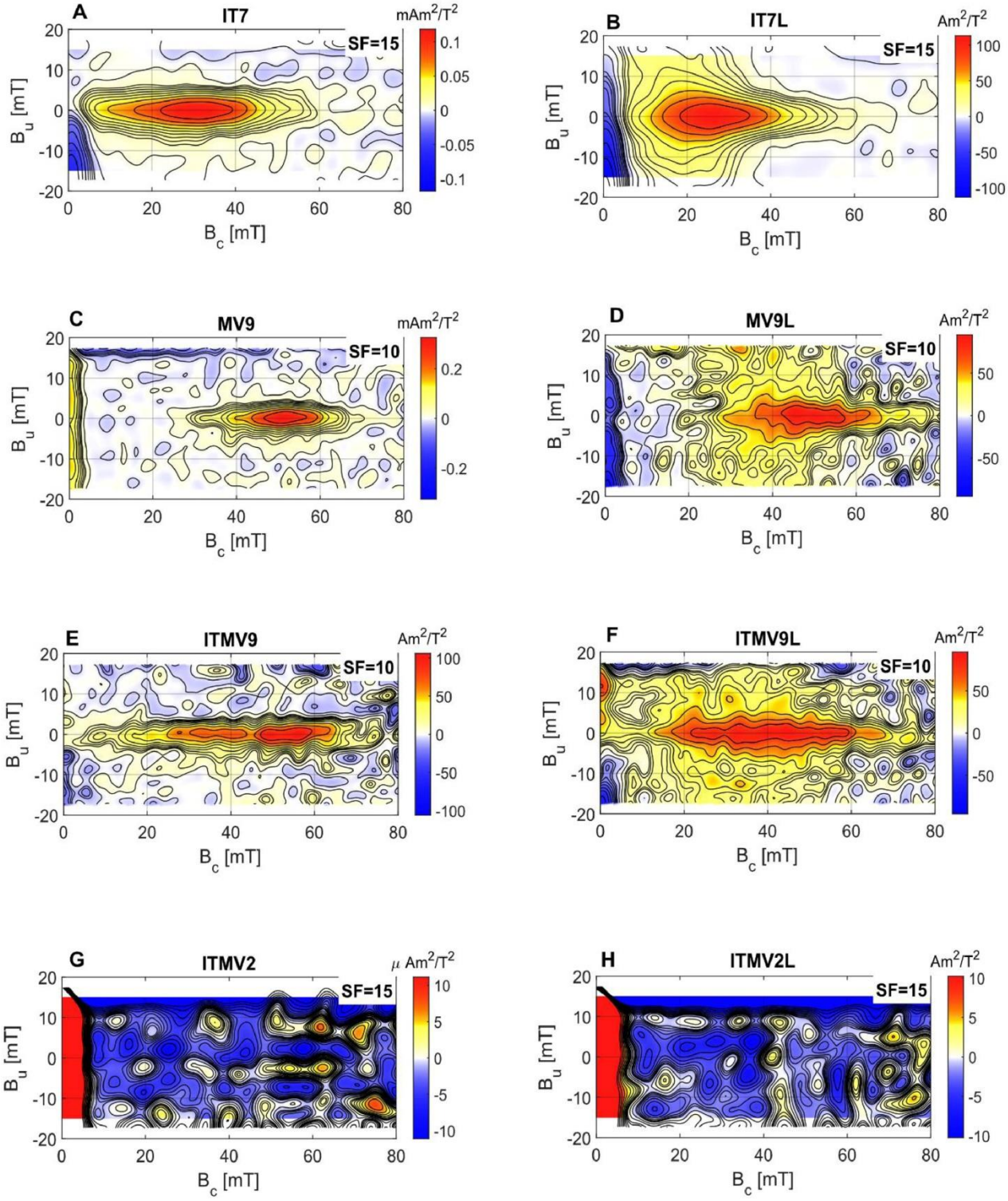

Fig. 5. First Order reversal Curve (FORC) diagrams processed by the Forcot software (A-F) for samples MV9, IT7, ITMV9 (magnetosomal magnetic particle concentration = 10^7 and above. i.e, magnetically measurable) and (G and H) ITMV2 (magnetic particle concentration = 10^2 i.e, magnetically unmeasurable); Left (A, C, E and G**):** Whole cells: Right (B, D, F and H): Lysed cells.

Moreover, Hashim et al. (2012) described the changes in cultivation conditions may change the duration of magnetic particle biomineralization morphology and magnetic properties. An increase in magnetic coercivity could be caused by shape anisotropy while lower coercivities may be the result of the SD state of magnetic particles in cultivated MTB (Hashim et al., 2012). In this study, the coercivity data are compatible (between 10.46 and 27.36 mT) for SD magnetite for all samples containing 10^7 cells or more (Fig. 2). Other samples with less than 10^7 cells also have similar coercivities; however, the trend is not continuous and the FORCs processed in either softwares (Forcot and FORCinel) have no measurable fingerprint (Fig. 4 and 5). Values of coercivities and remanences may also depend on intra-chain spacing between magnetic particles as described by Berndt et al. (2020), which was not assessed here.

Magnetic properties of isolated magnetosomes produced by *Magnetospirillum magneticum* AMB-1 demonstrated an increase in magnetostatic interactions and reduced magnetic properties compared to whole cells with an intact magnetosome chain (Li et al., 2010). Our results are compatible with the results of Li et al. (2010) because the magnetic properties (M_r, M_{rs} and B_c of lysed cells for measurable samples ($\geq 10^7$ cells) are relatively lower than for whole cells (Fig. 2). Magnetostatic interactions increased significantly for the lysed cell equivalents of the measurable samples (Fig. 5). Increase in magnetostatic interactions can be clearly seen in the FORC diagrams produced by the new Forcot software (Berndt and Chang, 2019) (Fig. 5).

The notable presence of gene encoding ribulose-1,5-bisphosphate carboxylase (RuBisCO), an autotrophic carbon fixing enzyme has demonstrated the chemoautotrophic ability as a common trait among MTB (Williams et al., 2006; Bazylinski et al., 2007; Silva et al., 2013).

Quantification of prokaryotic carbon biomass (bacteria and archaea) is important in marine ecology studies that consider the functioning of the food web and biogeochemical cycles in water bodies (Fukuda et al., 1998; Li et al., 2021). In natural aquatic environments, the biomass of prokaryotic communities is mainly investigated by cell counting using epifluorescence microscopy or flow cytometry. A standard conversion factor is usually applied to transform cell number into carbon content to estimate biomass (La Ferla et al., 2012). However, the carbon content of a cell varies with its volume (Fukuda et al., 1998), so use of a constant conversion factor can lead to over or under estimation of the actual permanent stock (La Ferla et al., 2012). Consequently, size determination is necessary to estimate prokaryote biomass more accurately. Cytometric signature analysis of MV-1^T and IT-1 bacteria compared to marine samples from coastal waters (sample from the entrance of Guanabara Bay, Rio de Janeiro, Brazil) indicates that the cultivated MTB studied here were much larger than typical bacteria from coastal

environments (Fig. 6). Note that strains MV-1^T and IT-1 are distributed farther to the right on the SSC axis compared to marine bacteria (Fig. 6).

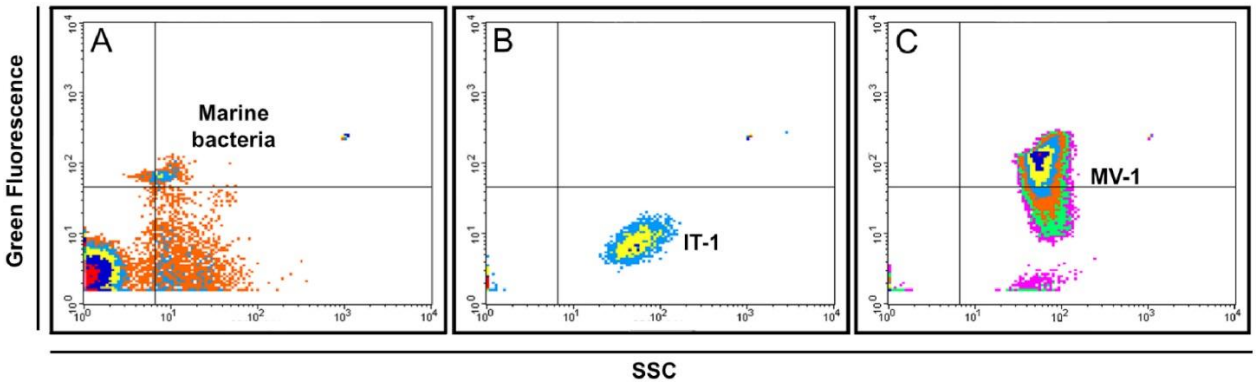

Fig. 6. Comparison of: **A;** marine bacteria, **B;** *Mf. Australis* strain IT-1 and **C;** *Mv. Blakemorei* strain MV-1^T by flow cytometry. The x-axis indicates the 90° lateral scattering of light (SSC) and the y-axis indicates the green fluorescence emitted after labeling with SYBR Green I.

A summary of carbon and magnetite contents in 10^9 cells of the MV-1^T and IT-1 strains are shown in Table 2. Although carbon content values are discrepant when different methods are applied, some authors consider this parameter to be useful for inferring the contribution of bacterial biomass in the natural environment because of the difficulty in measuring natural communities composed of different morphotypes (Calvo-Díaz et al., 2011).

Table 2. Carbon and magnetite content estimation for 10^9 cells of *Magnetovibrio blakemorei* strain MV-1 and *Magnetofaba marinus* strain IT-1.

MTB Species	**Magnetosome morphology/ composition /size**	**Standard Carbon content estimation by flow cytometry (20 fg C per cell)**	**Carbon estimation based on the determination of the cell volume by microscopy**	**Magnetite content (mass) estimation**
Magnetovibrio blakemorei strain MV-1	Truncated hexaoctahedral magnetite (60 × 40nm)	20 mgC	48.5 mgC	3,4 µg (anaerobic growth with N_2O)
Magnetofaba marinus strain IT-1	elongated octahedral magnetite (83 × 74nm)	20 mgC	154.2 mgC	23,5 µg (heterotrophic growth with sodium acetate; microaerophilic conditions)

Even though cytometry allows cell alignment in a sample to the point where each cell passes individually in front of the laser, the cells are inside a carrier fluid and can pass in any orientation with respect to the laser and detector. As a result, relative SSC values should not represent the correct cell size, except when analyzing spherical cells. However, SSC can be used for comparative determination of different cell sizes (Gasol et al., 1997), as we demonstrate here. For now, our results indicate that microscopy is more reliable for measuring bacterial cells and their volume, which combined with accurate counting performed with flow cytometry allows reliable bacterial biomass determination.

Nevertheless, Kirschvink and Chang (1984) proposed that iron and carbon cycling are important contributions of MTB, and that magnetofossils could be used as paleoenvironmental indicators. Yamazaki and Kawahata (1998) further proposed a relationship between organic C flux and the abundance of different magnetofossil morphologies (Yamazaki and Kawahata, 1998). Snowball et al. (1999) also described the relationship between high organic carbon and biogenic magnetite in Holocene sediments. Our data (Table 2, Fig. 1) are consistent with the previous studies as the larger sized cells containing elongated octahedral crystals of IT-I have relatively higher amounts of carbon (154.2 mgC) as compared to the smaller sized cells having hexoctahedral crystals of MV-1 i.e., (48.5 mgC). Although we found little effect of genetic species, magnetic particle size or shape on magnetic properties of the samples, however, either of these factors contribute to the amount of carbon. Positive relationship between the amount of carbon and the above-mentioned factors could explain the C flux control over these factors.

Yamazaki and Kawahata (1998) demonstrated an organic carbon flux control over the morphology of magnetosomal magnetite crystals, which further suggested the application of MTB for paleoenvironmental reconstruction of sedimentary sequences. Pósfai et al. (2013) studied phylogenetic effects in relation to magnetosomal mineral morphology. Among other factors affecting the morphology of magnetosomal crystals are environmental factors. However, genetics seem to exert the dominant influence on crystal habit (cuboctahedral, elongated-prismatic, and elongated-anisotropic) (Pósfai et al., 2013; Liu et al., 2021).

This study provides preliminary insights into potential role of magnetotactic bacteria in global carbon cycling processes, as well as the efficacy of current magnetic methods for detecting different concentrations of nanoparticles. However, we propose further investigations involving a variety of factors such as diverse bacterial species, cell concentrations, magnetic nanoparticle composition (i.e., greigite/magnetite), sizes and shapes. More observations are necessary to

estimate the net carbon balance and its relation to different variables throughout geological history.

4.4 Conclusions

Magnetic methods used for the detection of magnetofossils or biogenic magnetite largely depend on the concentration of magnetic particles rather than magnetite producing MTB (strains MV-1^T or IT-1). Magnetic properties are significantly lower for the samples containing less than 10^7 cells (unmeasurable samples) while the FORC diagrams have no measurable magnetic fingerprint for these samples. Hence, it is concluded that 10^7 cells or more are a measurable threshold for the magnetic nanoparticles produced by MTB strains MV-1^T or IT-1. FORC diagrams are a valuable tool for identifying magnetic domain state as well as interactions among magnetic particles, they are highly sensitive to the total number of magnetic particles within cells. Hence, unmeasurable magnetic signals could undermine detection of lower magnetic particle concentrations in a sample.

IT-I cells containing larger sized, elongated octahedral magnetic crystals have higher amounts of carbon content as compared to the smaller sized, MV-1 cells having hexoctahedral crystals. The system acts in one way as a carbon sink. These observations are necessary to accurately quantify the carbon fluxes related to a complex network of processes and establish the net carbon balance of the environmental system linked to the MTB carbon sink. This study represents pioneering work about carbon-cycling processes which are still not identified in modern and ancient sedimentary systems. More detailed observations are required to characterize carbon cycling, even in relatively simple environmental conditions.

References

Abreu, F., Carolina, A., Araujo, V., Le˜ao, P., Silva, K.T., Carvalho, F.M., Cunha, O.L., Almeida, L.G., Geurink, C., Farina, M., Rodelli, D., Jovane, L., Pellizari, V.H., Vasconcelos, A.T., Bazylinski, D.A., Lins, U., 2016. Culture-independent characterization of novel psychrophilic magnetotactic cocci from Antarctic marine sediments. Environ. Microbiol. 18, 4426–4441. https://doi.org/10.1111/1462-2920.13388.

Abreu, F., Silva, K.T., Le˜ao, P., Guedes, I.A., Keim, C.N., Farina, M., Lins, U., 2013. Cell adhesion, multicellular morphology, and magnetosome distribution in the multicellular

magnetotactic prokaryote candidatus magnetoglobus multicellularis. Microsc. Microanal. 19, 535–543. https://doi.org/10.1017/S1431927613000329.
Bazylinski, D.A., Frankel, R.B., 2004. Magnetosome formation in prokaryotes. Nat. Rev. Microbiol. 2, 217–230. https://doi.org/10.1038/nrmicro842.

Bazylinski, D.A., Frankel, R.B., Konhauser, K.O., 2007. Modes of biomineralization of magnetite by microbes. Geomicrobiol. J. https://doi.org/10.1080/01490450701572259.

Bazylinski, D.A., Williams, T.J., Lef`evre, C.T., Berg, R.J., Zhang, C.L., Bowser, S.S., Dean, A.J., Beveridge, T.J., 2013a. Magnetococcus marinus gen. nov., sp. nov., a marine, magnetotactic bacterium that represents a novel lineage (Magnetococcaceae fam. nov., Magnetococcales ord. nov.) at the base of the Alphaproteobacteria. Int. J. Syst. Evol. Microbiol. 63 https://doi.org/10.1099/ijs.0.038927-0.

Bazylinski, D.A., Williams, T.J., Lef`evre, C.T., Trubitsyn, D., Fang, J., Beveridge, T.J., Moskowitz, B.M., Ward, B., Schübbe, S., Dubbels, B.L., Simpson, B., 2013b. Magnetovibrio Blakemore gen. nov., sp. nov., a magnetotactic bacterium (Alphaproteobacteria: Rhodospirillaceae) isolated from a salt marsh. Int. J. Syst. Evol. Microbiol. 63 https://doi.org/10.1099/ijs.0.044453-0.

Bergo, N.M., Signori, C.N., Amado, A.M., Brandini, F.P., Pellizari, V.H., 2017. The partitioning of carbon biomass among the pico-and nano-plankton community in the South Brazilian bight during a strong summer intrusion of south atlantic central water. Front. Mar. Sci. 4 https://doi.org/10.3389/fmars.2017.00238.

Berndt, T.A., Chang, L., 2019. Waiting for forcot: accelerating FORC processing 100× using a fast-fourier-transform algorithm. Geochem. Geophys. Geosyst. 20 https:// doi.org/10.1029/2019GC008380.

Berndt, T.A., Chang, L., Pei, Z., 2020. Mind the gap: Towards a biogenic magnetite palaeoenvironmental proxy through an extensive finite-element micromagnetic simulation. Earth Planet. Sci. Lett. 532 https://doi.org/10.1016/j.epsl.2019.116010.

Berner, R.A., 2003. The long-term carbon cycle, fossil fuels and atmospheric composition. Nature. https://doi.org/10.1038/nature02131.

Calvo-Díaz, A., Díaz-P´erez, L., Su´arez, L.´A., Mor´an, X.A.G., Teira, E., Mara˜n´on, E., 2011. Decrease in the autotrophic-to-heterotrophic biomass ratio of picoplankton in oligotrophic marine waters due to bottle enclosure. Appl. Environ. Microbiol. 77, 5739–5746. https://doi.org/10.1128/AEM.00066-11.

Chang, L., Harrison, R.J., Zeng, F., Berndt, T.A., Roberts, A.P., Heslop, D., Zhao, X., 2018. Coupled microbial bloom and oxygenation decline recorded by magnetofossils during the palaeocene–eocene thermal maximum. Nat. Commun. 9 https://doi.org/10.1038/s41467-01806472-y.

Chang, L., Heslop, D., Roberts, A.P., Rey, D., Mohamed, K.J., 2016. Discrimination of biogenic and detrital magnetite through a double Verwey transition temperature. J. Geophys. Res. Solid Earth 121. https://doi.org/10.1002/2015JB012485.

Chang, L., Roberts, A.P., Williams, W., Fitz Gerald, J.D., Larrasoa˜na, J.C., Jovane, L., Muxworthy, A.R., 2012. Giant magnetofossils and hyperthermal events. Earth Planet. Sci. Lett. 351–352, 258–269. https://doi.org/10.1016/J.EPSL.2012.07.031.

Chang, L., Roberts, A.P., Winklhofer, M., Heslop, D., Dekkers, M.J., Krijgsman, W., Gerald, J.D.F., Smith, P., 2014. Magnetic detection and characterization of biogenic magnetic minerals: a comparison of ferromagnetic resonance and first-order reversal curve diagrams. J. Geophys. Res. Solid Earth 119. https://doi.org/10.1002/2014JB011213.

Chen, A.P., Egli, R., Moskowitz, B.M., 2007. First-order reversal curve (FORC) diagrams of natural and cultured biogenic magnetic particles. J. Geophys. Res. Solid Earth 112. https://doi.org/10.1029/2006JB004575.

Coccioni, R., Frontalini, F., Catanzariti, R., Jovane, L., Rodelli, D., Rodrigues, I.M.M., Savian, J.F., Giorgioni, M., Galbrun, B., 2019. Paleoenvironmental signature of the selandian-thanetian transition event (STTE) and early late paleocene event (ELPE) in the contessa road section

(western neo-tethys). Palaeogeogr. Palaeoclimatol. Palaeoecol. 523 https://doi.org/10.1016/j.palaeo.2019.03.023.

Dasdag, S., 2014. Magnetotactic bacteria and their application in medicine. J. Phys. Chem. Biophys. 2 https://doi.org/10.4172/2161-0398.1000141.

De Martini, F., Neuer, S., Hamill, D., Robidart, J., Lomas, M.W., 2018. Clade and strain specific contributions of Synechococcus and Prochlorococcus to carbon export in the Sargasso Sea. Limnol. Oceanogr. 63 https://doi.org/10.1002/lno.10765.

Dong, Y., Li, J., Zhang, W., Zhang, W., Zhao, Y., Xiao, T., Wu, L.F., Pan, H., 2016. The detection of magnetotactic bacteria in deep sea sediments from the east pacific manganese nodule province. Environ. Microbiol. Rep. 8, 239–249. https://doi.org/10.1111/1758-2229.12374.

Dunin-Borkowski, R.E., McCartney, M.R., Frankel, R.B., Bazylinski, D.A., P´osfai, M., Buseck, P.R., 1998. Magnetic microstructure of magnetotactic bacteria by electron holography. Science (80), 282. https://doi.org/10.1126/science.282.5395.1868.

Egli, R., 2013. VARIFORC: an optimized protocol for calculating non-regular first-order reversal curve (FORC) diagrams. Glob. Planet. Change 110, 302–320. https://doi.org/10.1016/J.GLOPLACHA.2013.08.003.

Egli, R., Chen, A.P., Winklhofer, M., Kodama, K.P., Horng, C.-S., 2010. Detection of noninteracting single domain particles using first-order reversal curve diagrams. Geochem. Geophys. Geosyst. 11 https://doi.org/10.1029/2009gc002916.

Faivre, D., B¨ottger, L.H., Matzanke, B.F., Schüler, D., 2007. Intracellular magnetite biomineralization in bacteria proceeds by a distinct pathway involving membrane- bound ferritin and an iron(II) species. Angew. Chem. Int. Ed. 46 https://doi.org/10.1002/anie.200700927.

Faivre, D., Schüler, D., 2008. Magnetotactic bacteria and magnetosomes. Chem. Rev. 108, 4875–4898. https://doi.org/10.1021/CR078258W.

Frankel, R.B., Bazylinski, D.A., 2006. How magnetotactic bacteria make magnetosomes queue up. Trends Microbiol. 14, 329–331. https://doi.org/10.1016/J.TIM.2006.06.004.
Frankel, R.B., Frankel, B.R., 2009. The discovery of magnetotactic/magnetosensitive bacteria. ChJOL 27, 1–2. https://doi.org/10.1007/S00343-009-0001-7.

Frontalini, F., Coccioni, R., Catanzariti, R., Jovane, L., Savian, J.F., Sprovieri, M., 2016. The eocene thermal maximum 3: reading the environmental perturbations at Gubbio (Italy). Spec. Pap. Geol. Soc. Am. 524, 161–175. https://doi.org/10.1130/2016.2524(11.

Fukuda, R., Ogawa, H., Nagata, T., Koike, I., 1998. Direct determination of carbon and nitrogen contents of natural bacterial assemblages in marine environments. Appl. Environ. Microbiol. 64, 3352–3358. https://doi.org/10.1128/AEM.64.9.3352-3358.1998.

Gareev, K.G., Grouzdev, D.S., Kharitonskii, P.V., Kirilenko, D.A., Kosterov, A., Koziaeva, V.V., Levitskii, V.S., Multhoff, G., Nepomnyashchaya, E.K., Nikitin, A.V., Nikitina, A., Sergienko, E.S., Sukharzhevskii, S.M., Terukov, E.I., Trushlyakova, V.V., Shevtsov, M., 2021. Magnetic properties of bacterial magnetosomes produced by magnetospirillum caucaseum so 1. Microorganisms 9. https://doi.org/10.3390/microorganisms9091854.

Gasol, J.M., Del Giorgio, P.A., 2000. Using flow cytometry for counting natural planktonic bacteria and understanding the structure of planktonic bacterial communities. Sci. Mar. https://doi.org/10.3989/scimar.2000.64n2197.

Gasol, J.M., Del Giorgio, P.A., Duarte, C.M., 1997. Biomass distribution in marine planktonic communities. Limnol. Oceanogr. 42, 1353–1363. https://doi.org/10.4319/LO.1997.42.6.1353.

Giorgioni, M., Jovane, L., Rego, E.S., Rodelli, D., Frontalini, F., Coccioni, R., Catanzariti, R., Özcan, E., 2019. Carbon cycle instability and orbital forcing during the middle eocene climatic optimum. Sci. Rep. 9 https://doi.org/10.1038/s41598-019-45763-2.

Goswami, P., He, K., Li, J., Pan, Y., Roberts, A.P., Lin, W., 2022. Magnetotactic bacteria and magnetofossils: ecology, evolution and environmental implications. https://doi.org/10.1038/s41522-02200304-0.

Harrison, R.J., Feinberg, J.M., 2008. FORCinel: an improved algorithm for calculating first order reversal curve distributions using locally weighted regression smoothing. Geochem. Geophys. Geosyst. 9 https://doi.org/10.1029/2008GC001987.

Hashim, A., Molˇcan, M., Kovaˇc, J., Varchulov´a, Z., Gojzewski, H., Makowski, M., Kopˇcansky, P., Tomori, Z., Timko, M., 2012. The influence of morphology on magnetic properties of magnetosomes. Acta Phys. Pol. A 121, 1250–1252. https://doi.org/10.12693/APHYSPOLA.121.1250.

Hassan, M.B, Rodelli, D., Benites, M., Abreu, F., Murton, B., Jovane, L., 2020. Presence of biogenic magnetite in ferromanganese nodules. Wiley Online Libr. 12, 288–295. https://doi.org/10.1111/1758-2229.12831.

Hayes, J.M., Waldbauer, J.R., 2006. The carbon cycle and associated redox processes through time. Philos. Trans. R. Soc. B Biol. Sci. 361, 931–950. https://doi.org/10.1098/RSTB.2006.1840.

Heslop, D., Roberts, A.P., Chang, L., Davies, M., Abrajevitch, A., De Deckker, P., 2013. Quantifying magnetite magnetofossil contributions to sedimentary magnetizations. Earth Planet. Sci. Lett. 382, 58–65. https://doi.org/10.1016/J.EPSL.2013.09.011.

Jiang, X.D., Zhao, X., Chou, Y.M., Liu, Q.S., Roberts, A.P., Ren, J.B., Sun, X.M., Li, J.H., Tang, X., Zhao, X.Y., Wang, C.C., 2020. Characterization and quantification of magnetofossils within abyssal manganese nodules from the western pacific ocean and implications for nodule formation. Geochem. Geophys. Geosyst. 21 https://doi.org/10.1029/2019GC008811.

Jovane, L., Florindo, F., Bazylinski, D.A., Lins, U., 2012. Prismatic magnetite magnetosomes from cultivated Magnetovibrio blakemorei strain MV-1: A magnetic fingerprint in marine sediments? Environ. Microbiol. Rep. 4, 664–668. https://doi.org/10.1111/1758-2229.12000.

Key, R.M., Kozyr, A., Sabine, C.L., Lee, K., Wanninkhof, R., Bullister, J.L., Feely, R.A., Millero, F.J., Mordy, C., Peng, T.H., 2004. A global ocean carbon climatology: results from

global data analysis project (GLODAP). Glob. Biogeochem. Cycles 18. https://doi.org/10.1029/2004GB002247.

Kirschvink, J.L., Chang, S.R., 1984. Ultrafine-grained magnetite in deep-sea sediments: possible bacterial magnetofossils. Geology 12. https://doi.org/10.1130/0091-7613(1984)12<559:UMIDSP>2.0.CO;2.

Kolber, Z.S., Plumley, F.G., Lang, A.S., Beatty, J.T., Blankenship, R.E., VanDover, C.L., Vetriani, C., Koblizek, M., Rathgeber, C., Falkowski, P.G., 2001. Contribution of aerobic photoheterotrophic bacteria to the carbon cycle in the ocean. Science 292 (80). https://doi.org/10.1126/science.1059707.

Kopp, R.E., Kirschvink, J.L., 2008. The identification and biogeochemical interpretation of fossil magnetotactic bacteria. Earth-Sci. Rev. 86 https://doi.org/10.1016/j. earscirev.2007.08.001.

Krambeck, C., Krambeck, H.J., Overbeck, J., 1981. Microcomputer-assisted biomass determination of plankton bacteria on scanning electron micrographs. Appl. Environ. Microbiol. 42, 142–149. https://doi.org/10.1128/aem.42.1.142-149.1981.

Kump, L.R., Arthur, M.A., 1999. Interpreting carbon-isotope excursions: carbonates and organic matter. Chem. Geol. 161 https://doi.org/10.1016/S0009-2541(99)00086-8.

la Ferla, R., Maimone, G., Azzaro, M., Conversano, F., Brunet, C., Cabral, A.S., Paranhos, R., 2012. Vertical distribution of the prokaryotic cell size in the Mediterranean Sea. Helgol. Mar. Res. 66 https://doi.org/10.1007/s10152-012-0297-0.

Larrasoa˜na, J.C., Liu, Q., Hu, P., Roberts, A.P., Mata, P., Civis, J., Sierro, F.J., P´erez- Asensio, J.N., 2014. Paleomagnetic and paleoenvironmental implications of magnetofossil occurrences in late Miocene marine sediments from the Guadalquivir Basin. SW Spain. Front. Microbiol. 5 https://doi.org/10.3389/fmicb.2014.00071.

Lechtenfeld, O.J., Hertkorn, N., Shen, Y., Witt, M., Benner, R., 2015. Marine sequestration of carbon in bacterial metabolites. Nat. Commun. 6 https://doi.org/10.1038/ncomms7711.

Lee, S., Fuhrman, J.A., 1987. Relationships between biovolume and biomass of naturally derived marine bacterioplankton. Appl. Environ. Microbiol. 53 https://doi.org/10.1128/aem.53.6.1298-1303.1987.

Lef`evre, C.T., Bazylinski, D.A., 2013. Ecology, diversity, and evolution of magnetotactic bacteria. Microbiol. Mol. Biol. Rev. 77, 497–526. https://doi.org/10.1128/mmbr.00021-13.

Lef`evre, C.T., Bernadac, A., Yu-Zhang, K., Pradel, N., Wu, L.F., 2009. Isolation and characterization of a magnetotactic bacterial culture from the Mediterranean Sea. Environ. Microbiol. 11 https://doi.org/10.1111/j.1462-2920.2009.01887.x.

Li, J., Ge, K., Pan, Y., Williams, W., Liu, Q., Qin, H., 2013. A strong angular dependence of magnetic properties of magnetosome chains: Implications for rock magnetism and paleomagnetism. Geochem. Geophys. Geosyst. 14 https://doi.org/10.1002/ggge.20228.

Li, J., Liu, P., Tamaxia, A., Zhang, H., Liu, Y., Wang, J., Menguy, N., Zhao, X., Roberts, A. P., Pan, Y., 2021. Diverse intracellular inclusion types within magnetotactic bacteria: implications for biogeochemical cycling in aquatic environments. J. Geophys. Res. Biogeosci. 126 (7), e2021JG006310 https://doi.org/10.1029/2021JG006310.

Li, J.H., Pan, Y.X., Liu, Q.S., Qin, H.F., Deng, C.L., Che, R.C., Yang, X.A., 2010. A comparative study of magnetic properties between whole cells and isolated magnetosomes of Magnetospirillum magneticum AMB-1. Chin. Sci. Bull. 55 https://doi.org/10.1007/s11434009-0333-x.

Lin, W., Pan, Y., Bazylinski, D.A., 2017. Diversity and ecology of and biomineralization by magnetotactic bacteria. Environ. Microbiol. Rep. https://doi.org/10.1111/1758- 2229.12550.

Lin, W., Zhang, W., Zhao, X., Roberts, A.P., Paterson, G.A., Bazylinski, D.A., Pan, Y., 2018. Genomic expansion of magnetotactic bacteria reveals an early common origin of magnetotaxis with lineage-specific evolution. ISME J. 12 https://doi.org/10.1038/s41396-018-0098-9.

Liu, P., Liu, Y., Zhao, X., Roberts, A.P., Zhang, H., Zheng, Y., Wang, F., Wang, L., Menguy, N., Pan, Y., Li, J., 2021. Diverse phylogeny and morphology of magnetite biomineralized by magnetotactic cocci. Environ. Microbiol. 23 https://doi.org/10.1111/1462-2920.15254.

Lu, Y., Wang, D., Jiang, X., Lin, Z., Yang, Y., Liu, Q., Liu, Q., Lu, Y., Wang, D., Lin, X., Yang, Z., Liu, &., Lu, A.L., 2021. Paleoenvironmental significance of magnetofossils in pelagic sediments in the equatorial pacific ocean before and after the eocene/ oligocene boundary. Wiley Online Libr. 126 https://doi.org/10.1029/2021JB022221.

Lund, S., Platzman, E., Thouveny, N., Camoin, G., Corsetti, F. and Berelson, W., 2010. Biological control of paleomagnetic remanence acquisition in carbonate framework rocks of the Tahiti coral reef. *Earth and Planetary Science Letters*, *298*(1-2), pp.14-22. https://doi.org/10.1016/j.epsl.2010.07.010

Maratea, D., Blakemore, R.P., 1981. Aquaspirillum magnetotacticum sp. nov., a magnetic spirillum. Int. J. Syst. Bacteriol. 31, 452–455. https://doi.org/10.1099/00207713- 31-4-452.

Matsunaga, T., Sakaguchi, T., Tadakoro, F., 1991. Magnetite formation by a magnetic bacterium capable of growing aerobically. Appl. Microbiol. Biotechnol. 35, 651–655. https://doi.org/10.1007/BF00169632.

Morillo, V., Abreu, F., Araujo, A.C., De Almeida, L.G.P., Enrich-Prast, A., Farina, M., De Vasconcelos, A.T.R., Bazylinski, D.A., Lins, U., 2014. Isolation, cultivation and genomic analysis of magnetosome biomineralization genes of a new genus of South- seeking magnetotactic cocci within the Alphaproteobacteria. Front. Microbiol. 5 https://doi.org/10.3389/fmicb.2014.00072.

Moskowitz, B.M., Frankel, R.B., Bazylinski, D.A., 1993. Rock magnetic criteria for the detection of biogenic magnetite. Earth Planet. Sci. Lett. 120, 283–300. https://doi.org/10.1016/0012-821X(93)90245-5.

Norland, S., Heldal, M., Tumyr, O., 1987. On the relation between dry matter and volume of bacteria. Microb. Ecol. 13 https://doi.org/10.1007/BF02011246.

Oda, H., Nakasato, Y., Usui, A., 2018. Characterization of marine ferromanganese crust from the pacific using residues of selective chemical leaching : identification of fossil magnetotactic bacteria with FE - SEM and rock magnetic methods. Earth Planets 1–10. https://doi.org/10.1186/s40623-018-0924-3.

Paterson, G.A., Zhao, X., Jackson, M., Heslop, D., 2018. Measuring, processing, and analyzing hysteresis data. Geochem. Geophys. Geosyst. 19, 1925–1945. https://doi.org/10.1029/2018GC007620.

P´osfai, M., Lef`evre, C.T., Trubitsyn, D., Bazylinski, D.A., Frankel, R.B., 2013. Phylogenetic significance of composition and crystal morphology of magnetosome minerals. Front. Microbiol. 4 https://doi.org/10.3389/FMICB.2013.00344/FULL.

Raymo, M.E., Ruddiman, W., 1993. Cooling in the late Cenozoic. Nature. https://doi.org/10.1038/361124a0.

Ribeiro, C.G., dos Santos, A.L., Marie, D., Pellizari, V.H., Brandini, F.P., Vaulot, D., 2016. Pico and nanoplankton abundance and carbon stocks along the Brazilian Bight. PeerJ 2016. https://doi.org/10.7717/peerj.2587.

Roberts, A., 2000. First-order reversal curve diagrams: a new tool for characterizing the magnetic properties of natural samples. Wiley Online Libr. 105, 461–489. https://doi.org/10.1029/2000JB900326.

Roberts, A.P., Chang, L., Heslop, D., Florindo, F., Larrasoa˜na, J.C., Roberts, C.:, Chang, L., Heslop, D., Florindo, F., Larrasoa˜na, J.C., 2012. Searching for single domain magnetite in the “pseudo-single-domain” sedimentary haystack: Implications of biogenic magnetite preservation for sediment magnetism. Wiley Online Libr. 117, 8104. https://doi.org/10.1029/2012JB009412.

Roberts, A.P., Florindo, F., Villa, G., Chang, L., Jovane, L., Bohaty, S.M., Larrasoa˜na, J.C., Heslop, D., Fitz Gerald, J.D., 2011. Magnetotactic bacterial abundance in pelagic marine environments is limited by organic carbon flux and availability of dissolved iron. Earth Planet. Sci. Lett. 310, 441–452. https://doi.org/10.1016/j.epsl.2011.08.011.

Rodelli, D., Jovane, L., Giorgioni, M., Rego, E.S., Cornaggia, F., Benites, M., Cedraz, P., Berbel, G.B.B., Braga, E.S., Ustra, A., Abreu, F., Roberts, A.P., 2019. Diagenetic fate of biogenic soft and hard magnetite in chemically stratified sedimentary environments of mamangu´a ría. Brazil. J. Geophys. Res. Solid Earth 124. https://doi.org/10.1029/2018JB016576.

Rodelli, D., Jovane, L., Roberts, A.P., Cypriano, J., Abreu, F., Lins, U., 2018. Fingerprints of partial oxidation of biogenic magnetite from cultivated and natural marine magnetotactic bacteria using synchrotron radiation. Environ. Microbiol. Rep. 10, 337–343. https://doi.org/10.1111/1758-2229.12644.

Sarmento, H., Gasol, J.M., 2012. Use of phytoplankton-derived dissolved organic carbon by different types of bacterioplankton. Environ. Microbiol. 14 https://doi.org/10.1111/j.1462-2920.2012.02787.x.

Savian, J.F., Jovane, L., Frontalini, F., Trindade, R.I.F., Coccioni, R., Bohaty, S.M., Wilson, P.A., Florindo, F., Roberts, A.P., Catanzariti, R., Iacoviello, F., 2014. Enhanced primary productivity and magnetotactic bacterial production in response to middle Eocene warming in the Neo-Tethys Ocean. Palaeogeogr. Palaeoclimatol. Palaeoecol. 414 https://doi.org/10.1016/j.palaeo.2014.08.009.

Savian, J.F., Jovane, L., Giorgioni, M., Iacoviello, F., Rodelli, D., Roberts, A.P., Chang, L., Florindo, F., Sprovieri, M., 2016. Environmental magnetic implications of magnetofossil occurrence during the middle eocene climatic optimum (MECO) in pelagic sediments from the equatorial Indian Ocean. Palaeogeogr. Palaeoclimatol. Palaeoecol. 441, 212–222. https://doi.org/10.1016/j.palaeo.2015.06.029.

Schleifer, K.H., Schüler, D., Spring, S., Weizenegger, M., Amann, R., Ludwig, W., K¨ohler, M., 1991. The genus magnetospirillum gen. nov. description of magnetospirillum gryphiswaldense sp. nov. and transfer of aquaspirillum magnetotacticum to magnetospirillum magnetotacticum comb. Nov. Syst. Appl. Microbiol. 14 https://doi.org/10.1016/S0723-2020(11)80313-9.

Silva, K.T., Le˜ao, P.E., Abreu, F., L´opez, J.A., Gutarra, M.L., Farina, M., Bazylinski, D.A., Freire, D.M.G., Lins, U., 2013. Optimization of magnetosome production and growth by the magnetotactic vibrio Magnetovibrio blakemorei strain MV-1 through a statistics-based experimental design. Appl. Environ. Microbiol. 79 https://doi.org/10.1128/AEM.03740-12.

Snowball, I., Sandgren, P., Petterson, G., 1999. The mineral magnetic properties of an annually laminated Holocene lake-sediment sequence in northern Sweden. Holocene 9. https://doi.org/10.1191/095968399670520633.

Staniland, S., Ward, B., Harrison, A., Van Der Laan, G., Telling, N., 2007. Rapid magnetosome formation shown by real-time x-ray magnetic circular dichroism. Proc. Natl. Acad. Sci. U. S. A. 104 https://doi.org/10.1073/pnas.0704879104.

Tajika, E., 1998. Climate change during the last 150 million years: Reconstruction from a carbon cycle model. Earth Planet. Sci. Lett. 160 https://doi.org/10.1016/S0012821X(98)00121-6.

Usui, Y., Yamazaki, T., Saitoh, M., 2017. Changing Abundance of Magnetofossil Morphologies in Pelagic Red Clay Around Minamitorishima. Western North Pacific. Geochemistry, Geophys. Geosystems 18. https://doi.org/10.1002/2017GC007127.

Von Dobeneck, T., 1996. A systematic analysis of natural magnetic mineral assemblages based on modelling hysteresis loops with coercivity-related hyperbolic basis functions. Geophys. J. Int. 124 https://doi.org/10.1111/j.1365-246x.1996.tb05632.x.

Weiss, B.P., Sam Kim, S., Kirschvink, J.L., Kopp, R.E., Sankaran, M., Kobayashi, A., Komeili, A., 2004. Ferromagnetic resonance and low-temperature magnetic tests for biogenic magnetite. Earth Planet. Sci. Lett. 224, 73–89. https://doi.org/10.1016/J.EPSL.2004.04.024.

Williams, T.J., Zhang, C.L., Scott, J.H., Bazylinski, D.A., 2006. Evidence for autotrophy via the reverse tricarboxylic acid cycle in the marine magnetotactic coccus strain MC-1. Appl. Environ. Microbiol. 72, 1322–1329. https://doi.org/10.1128/AEM.72.2.1322-1329.2006.

Yamazaki, T., 2009. Environmental magnetism of Pleistocene sediments in the north pacific and ontong-java plateau: temporal variations of detrital and biogenic components. Geochem. Geophys. Geosyst. 10 https://doi.org/10.1029/2009GC002413.

Yamazaki, T., Kawahata, H., 1998. Organic carbon flux controls the morphology of magnetofossils in marine sediments. Geology 26. https://doi.org/10.1130/00917613(1998)026<1064:OCFCTM>2.3.CO;2.

Yamazaki, T., Suzuki, Y., Kouduka, M., Kawamura, N., 2019. Dependence of bacterial magnetosome morphology on chemical conditions in deep-sea sediments. Earth Planet. Sci. Lett. 513, 135–143. https://doi.org/10.1016/J.EPSL.2019.02.015.

Yan, L., Zhang, S., Chen, P., Liu, H., Yin, H., Li, H., 2012. Magnetotactic bacteria, magnetosomes and their application. Microbiol. Res. https://doi.org/10.1016/j.micres.2012.04.002.

Yuan, W., Zhou, H., Yang, Z., Hein, J.R., Yang, Q., 2020. Magnetite magnetofossils record biogeochemical remanent magnetization in hydrogenetic ferromanganese crusts. Geology 48. https://doi.org/10.1130/G46881.1.

5 A MAGNETIC AND GEOCHEMICAL APPROACH TO THE CHANGING SEDIMENTATION ACCUMULATION ON THE UPPER SLOPE OF THE GREAT BARRIER REEF, NORTHEASTERN AUSTRALIAN MARGIN (CHAPTER 4)

Manuscript Published in *Quaternary Science Reviews*

Muhammad Bin Hassan[1], Gabriel Tagliaro[1], Brandon Harper[2], André W. Droxler[2], Emilio Herrero-Bervera[3], Yusuke Yokoyama[4], Ángel Puga-Bernabéu[5], Jody M. Webster[6] and Luigi Jovane[1]

[1]Oceanographic Institute, University of São Paulo, São Paulo, Brazil

[2]Department of Earth, Environmental and Planetary Sciences, Rice University, Houston, USA

[3]Hawaii Institute of Geophysics and Planetology, The University of Hawaii at Manoa, USA

[4]Atmosphere and Ocean Research Institute, The University of Tokyo, Japan

[5]Departamento de Estratigrafía y Paleontología, Universidad de Granada, 18002 Granada, Spain

[6]Geocoastal Research Group, School of Geosciences, The University of Sydney, Sydney, Australia

Abstract

The Great Barrier Reef (GBR) located along the northeastern margin of Australia is the largest coral reef system in the world. Modern climatic alterations are quickly changing the GBR ecosystem. To understand the implications of these changes it is important to reconstruct the geological history of GBR. Here we use geochemical and magnetic proxies to evaluate past climatic fluctuations and their consequences on sediment deposition along the GBR margin. IODP Expedition 325 – Hole M0058A, drilled on the uppermost slope at ca. 170 m water depth, reveals the depositional history of the GBR margin during the interval of MIS 7 to 5 and MIS 1. Magnetic and geochemical variations along the core section reveal detailed information on sediment accumulation and on the variations in terrigenous input in relation to sea-level fluctuations and climate change. Sea-level variations influenced margin deposition between MIS 7 and 6 impacting shoreline progradation/retrogradation and siliciclastic redistribution, resulting in a mixture of finer to coarser magnetic assemblages with no significant changes in terrigenous input. At the end of MIS 6 a decline in the deposition of carbonate sediments concomitant with the deposition of fine-grained magnetite-rich terrigenous sediments suggests an intensification of the monsoon in response to global warming trends. Arid periods over NE Australia were established after the glacial/interglacial transition (the MIS 6-5e) and at the middle Holocene (after the MIS 2-1 transition at ca. 7 ka), which favored dust deposition over the region. Enhanced dust fertilization subsequently promoted primary productivity at these

intervals resulting in the presence of biogenic magnetite at Hole M0058A produced by magnetotactic bacteria.

5.1 Introduction

The Great Barrier Reef (GBR), located on the northeastern margin of Australia, is the world's largest feature made up of living organisms. Among the most biodiverse places on Earth, the GBR sustains thousands of marine species, and its existence protects the Australian NE coasts from storm erosion while also contributing to the local economy through fisheries and tourism (Stoeckl et al., 2011; Pendleton et al., 2019). The ecosystem of the GBR is currently facing enormous threats due to modern climate warming (Wolanski and De'ath, 2005; McWhorter et al. 2022). Ocean acidification pushes coral bleaching along the GBR, drastically hindering the reef's capacity to reproduce and grow (De'ath et al., 2009; Wei et al., 2009; Mongin et al., 2016). Fast sea-level rise will require enhanced carbonate build-up to keep up the ecosystem within the photic zone (Hallock and Schlager, 1986). Also important but less investigated, widespread climatic alterations over northeastern Australia (i.e., monsoon changes) will impact precipitation and vegetation patterns on the hinterland, affecting terrigenous sediment transport into the GBR, which may increase water turbidity and sedimentation to a point that it impacts reef photosynthetic processes and drives reef speciation towards more sediment-resistant species (Thomas et al., 2007; Bannister et al., 2012; Cai and Cowan, 2013; Ayliffe et al., 2013).

Therefore, given the importance of the GBR to modern ecosystems and its current threats, it is crucial to understand how the GBR and the northeastern margin of Australia in general, are affected during climatic fluctuations such as those of today. Geological records from past periods of climatic change allow us to reconstruct the environmental alterations that occurred during these periods. In particular, the study of paleoclimatic proxies in marine sediment cores drilled in the region provides an exceptional opportunity to investigate how the GBR environment was affected during past climate changes. Among the many geological intervals when Earth's climate altered significantly, the Quaternary is marked by orbitally driven glacial-interglacial intervals (i.e., Marine Isotope Stages; MIS) that are potential analogues to modern warming (Yin and Berger, 2015; Burke et al., 2018). In particular, the Penultimate Glacial to Interglacial transition (MIS 6-5e; ca. 194 - 115 ka; Clark et al., 2020) and the Glacial substage to mid-Holocene transition (MIS 5d-1; ca. 115 – 6 ka are potential analogues for the modern rise in global temperatures, as global average temperatures during those interglacial peaks reached 2°C warmer than today (Burckle, 1993; Yin and Berger, 2015).

The full transition from glacial to interglacial during these two intervals represented a total of ca. 10°C rise in Antarctic temperatures (Jouzel et al., 1987; Lambert et al., 2008; Felis et al., 2014; Brenner et al., 2020).

The study of the magnetic properties of marine sediments can reveal the environmental conditions at the time of deposition since different magnetic minerals and associated mineral assemblages are formed under distinct conditions (Thompson and Oldfield, 1986; Verosub and Roberts, 1995). Therefore, environmental and rock magnetism can be used in a wide range of environments such as lacustrine, fluvial, aeolian and marine settings (Frederichs et al., 1999; Evans and Heller, 2003; Liu et al., 2011). The variability of magnetic properties in marine sediments has also been successfully used to track paleoclimatic events (Jovane et al., 2007a, 2007b, 2019; Leone et al., 2023).

Several studies have explained the relationship between environmental magnetism and sedimentary patterns in response to paleoenvironmental changes, such as environmental magnetism applied to paleosols (Maher and Thompson, 1992); magnetic properties of sediments and their relation to erosion, monsoon, and glacial-interglacial periods (Geiss and Banerjee, 1997; Zheng et al., 2010; Warrier et al., 2014; Li et al., 2018); magnetic proxies related to sea-level and climate change (Yang et al., 2008; Li et al., 2018); and environmental magnetism applied to summer monsoon intensification and ice melt over Himalaya during the Late Quaternary (Prajith et al., 2018).

Here, we present an environmental magnetic and geochemical study of the mixed siliciclastic-carbonate sequence of Hole M0058A, recovered during the International Ocean Discovery Program (IODP) Expedition 325 in the GBR (Webster et al., 2011; Yokoyama et al., 2011, Expedition 325 Scientists, 2011). Sediment cores provide a stratigraphic record that covers the last ca. 220 ka, which includes the Penultimate Glacial to Last Interglacial (Termination II) and the Last Glacial Maximum to mid-Holocene. However, MIS 2, 3, 4 and a part of MIS 6 are missing due to a recovery gap. Using geochemical and magnetic proxies, we reconstructed the paleoenvironmental conditions in the GBR margin during those climate transitions, and in particular, we investigated how climate change in the continental regions impacted the delivery of terrigenous sediments over the margin and affected the evolution of the carbonate factories in the GBR.

5.1.1. Geological Setting

5.1.1.1. Northeast Australian Continental Margin (NACM)

The Northeast Australian continental margin (NACM) is a passive margin with a large depositional area, extending from the GBR's shallow-water shelf environment to the deeper slope and basin settings in the neighboring Queensland and Townsville Troughs, which are narrow structural depressions formed as a result of extensional tectonics during the Late Cretaceous and Tertiary (Maxwell and Swinchatt, 1970; Davies et al., 1988; Francis et al., 2007) (Fig. 1). The formation and evolution of seafloor morphology along the NACM were controlled by the interplay of tectonics, sea-level fluctuations, and biogenic sedimentation (Francis et al., 2007; Puga-Bernabéu et al., 2011; 2013). In the shallow-water shelf, where the coral reefs of the GBR are located, biogenic carbonates are the main component of seafloor sediments, although a large concentration of terrigenous siliciclastic sediments is also found in some inter-reef passages of the GBR (Francis et al., 2007). Siliciclastics and carbonates are cyclically interbedded and are generally linked to temporal variation in sedimentation patterns, resulting from sea-level changes and/or variations in sediment supply (Maxwell and Swinchatt, 1970). The NACM slope is excavated by different types of canyon systems that export shallow-water siliciclastic and carbonate sediments from the platform to deep-water settings (Puga-Bernabéu et al., 2011, 2013, 2014; Webster et al., 2012). The slope is also affected by abundant mass-slope failures whose deposits were mainly accumulated on the basin floor (Puga-Bernabéu et al., 2017, 2020, 2022).

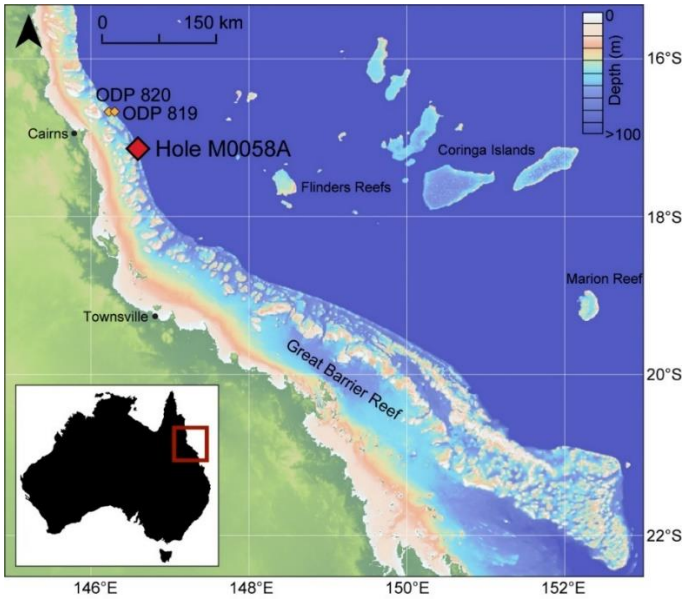

Fig.1. Bathymetric map (source: GEBCO) of the Great Barrier Reef (GBR) and the adjacent continental margin. Hole M0058A (red diamond) is located on the outer rim of the central region of the GBR at 172 m water depth. Other drilled sites in the area include Ocean Drilling Program (ODP) Leg 133 Sites 819 and 820 (yellow diamonds).

5.1.1.2. IODP Expedition 325 - Hole M0058A

IODP Expedition 325, “Great Barrier Reef Environmental Changes” drilled and cored four transects along the GBR (Yokoyama et al., 2011). The expedition's main goals included investigating the magnitude and nature of sea-level and climatic changes, as well as the response of coral reefs in the Great Barrier Reef since the Last Glacial Maximum. (Yokoyama et al., 2011; Yokoyama et al., 2018). Hole M0058A herein; 146° 35.357’ E and 17° 5.8356’S, located on the uppermost slope east of the Noggin Passage was the deepest hole drilled during IODP Expedition 325, at 172 m water depth (Fig. 1). The 41.4 m-long sedimentary sequence recovered in Hole M0058A achieved an 82% recovery in terms of depth and 68% in terms of time (Yokoyama et al., 2011; Herrero-Bervera and Jovane, 2013). Radiocarbon dating for the younger part of the core and Oxygen isotope measurements compared to LR04 $\delta^{18}O$ records confirmed the presence of MIS stages and the maximum age of ca. 220 ka for the core Hole M0058A (Harper et al., 2015). In the region near Hole M0058A, the shelf has a gently dipping surface, about 65 km wide, with the shelf break located at ca. 100 m depth (Abbey et al., 2011). The outer shelf at this location includes a variety of submerged features, such as barrier reefs, lagoons, pinnacles, and terraces (Beaman et al., 2008; Abbey et al., 2011; Hinestrosa et al., 2016). A slope-confined submarine canyon system partially erodes the slope in this region, which extends to the base of the slope at 900-1200 m, serving as a sediment bypass (Puga-Bernabéu et al., 2013; 2017).

Hole M0058A is mainly composed of three unconsolidated green fine carbonate units intercalated with two distinct sandy intervals (Harper et al., 2015). Carbonate content varies from 30% to 85%, with two distinct periods of less than 60% of concentration of fine carbonate sediments occurring between 32.5 and 28.8 and between 18.5 and 6 mbsf.

The fine carbonate-rich units have the highest reflectance values (or the lightest colors) and the lowest magnetic susceptibility values (Harper et al., 2015), and are rich in planktonic foraminifera. The upper sandy (grainstone) interval, at least 2 m thick, consists of fine to medium sand with large (up to cobble) rock fragments of well-cemented grainstone and visible fragments of molluscs, bryozoans, coralline algae, echinoids, benthic foraminifera, and serpulids. The lower sand interval is about 7 m thick and is characterized by fine to medium siliciclastic sand (Yokoyama et al., 2011). A cyclic pattern is observed within the lithological changes of Hole M0058A, illustrated in the color reflectance and the magnetic susceptibility data (Harper et al., 2015).

5.2 Materials and methods

5.2.1. Shipboard Data

Hole M0058A was subsampled using u-channels and 1-cc mini-cubes to study both their magnetic properties and the entire magnetostratigraphy of the carbonaceous sediments. Magnetic susceptibility and petrophysical properties were measured continuously in a GEOTEK multi-sensor core logger using a Bartington MS2 system, with a sampling interval of 1 cm (Expedition 325 Scientists, 2011; Fig. S1).

5.2.2. Geochemistry and Mineralogy

To understand the geochemical variations along the hole, X-ray fluorescence (XRF) measurements were performed for main elements (i.e., Si, Sr, Ca, Al, K, Fe, Mn and Ti) using a Dispersive X-ray Fluorescence Spectrometer (XRF) RIGAKU® Co (Tokyo, Japan), at the Centro Oceanográfico de Registro Estratigráfico (CORE) laboratory of the Oceanographic Institute of the University of São Paulo (IO-USP). 43 discrete samples weighing 2-gram at the average stratigraphic intervals of ~1 m were powdered and sieved through 150 μm. MESS-4 from the National Research Council Canada (NRC) was used as reference material. The data were plotted and compared with the high-resolution Si, Ca, and Sr results from Harper et al. (2015).

X-ray diffraction (XRD) analysis was also performed for the identification of the main mineralogical phases present at Hole M0058A, at every ~2 m. Dried bulk sediment samples were crushed and sieved at 150 μm. Samples were analyzed with an Olympus® BTX diffractometer at the CORE Lab, IO-USP (Pedrão et al., 2021). Mineral identification was performed using Xpowder software which uses identification criteria based on Moore and Reynolds (1989) and Hillier et al. (2003). The semi-quantitative data were later processed, compared, and plotted in percentage with the high-resolution data from Harper et al. (2015).

5.2.3. Magnetic measurements

Rock magnetic measurements [hysteresis cycles, First Order Reversal Curves (FORCs) and thermomagnetic curves] were performed at the CORE Lab of the IO-USP. A vibrating sample magnetometer (VSM) Micromag 3900 from Lake Shore was used to measure the Hysteresis cycles and FORCs. Hysteresis parameters such as magnetic saturation (M_s), remanence of magnetic saturation (M_{rs}) and magnetic coercivity (H_c) were obtained by applying a maximum field of 1 Tesla. Hysteresis results were processed (after applying paramagnetic correction) and plotted using the HystLab software provided by Paterson et al. (2018). H_{cr} was

obtained after measuring Direct Current Demagnetization (DCD) by applying a maximum field of 1T with 150 demagnetization steps. FORCs were produced by applying a maximum field of 1 T, with an average time of 150 ms on 297 curves in the space between B_c = 0–100 mT and B_u = 0 – 100 mT. The FORCs were processed using the FORCinel software provided by Harrison and Feinberg (2008). The smoothing factors of VARIFORC (8, 8, 3.5, 8 for Sc0, Sc1, Sb0, Sb1, 0.1 for lambda values and the output factor of 1) were applied to maximize the FORCs signals.

Thermomagnetic curves are used to understand the Curie (or Neel) temperature of the magnetic minerals where magnetic susceptibility is measured at regular intervals by consecutively heating the samples. Magnetic susceptibility *vs* temperature curves were obtained by progressive heating and cooling in the argon environment. Kappabridge MFK1 (AGICO) was used to perform the measurements. Bulk data were processed and plotted by the Cureval software provided by AGICO.

To study the variation of magnetic mineralogy along the section, continuous magnetic measurements were performed using a 2G superconducting squid magnetometer in u-channels. An artificial magnetic field of known characteristics was used to study the magnetic response of the samples under different conditions. The techniques involving such artificial fields were a) anhysteretic remanent magnetization (ARM), performed by imposing a 0.1 mT DC bias field while applying a 0.1 T demagnetizing alternating field. The ARM was then measured and progressively demagnetized via AF with fields of 5, 10, 15, 20, 25, 30, 40, 50, 60, 70, 80, 90, and 100 mT; Isothermal remanent magnetization (IRM) was imparted by applying firstly a 1 T direct field ($IRM@_{1.0}$) and subsequently a 0.1 ($IRM@_{-0.1}$) and 0.3 mT ($IRM@_{-0.3}$) direct field in the opposite direction (BIRM) (King and Channel, 1991; Verosub and Roberts, 1995; Liu et al., 2012; Jovane et al., 2013). Indirect parameters were calculated from these measurements as S-ratios ($S\text{-ratio}_{100}$ = $IRM@_{-0.1}/IRM@_{1.0}$; $S\text{-ratio}_{300}$ = $IRM@_{-0.3}/IRM@_{1.0}$); and HIRM (hard isothermal remanent magnetization) ($(IRM@_{-0.3}+IRM@_{1.0})/2$). S-ratios are a measure of the relative abundance of high-coercivity and low-coercivity minerals (Frank and Nowaczyk, 2008). The concentration of high-coercivity magnetic minerals is represented by HIRM (Stoner et al., 1996). The relative variation of the magnetic grain size along the section was calculated as (ARM/IRM).

5.3 Results

5.3.1. Rock Magnetism

In general, rock magnetic analyses (Hysteresis Cycles, Thermomagnetic curves, FORCs and Day plot) show single domain to pseudo-single domain magnetic grains of varying coercivities along the studied hole (Roberts et al., 2017; Zhao et al., 2017).

5.3.1.1. Hysteresis cycles

Analyses of hysteresis cycles combined with other rock magnetic data show single domain to pseudo-single domain grains of low coercivity magnetic minerals (Fig. 2). Hysteresis measurements show no typical features of the wasp-waisted cycles for most of the samples measured at 7.19 mbsf, at 17.84 mbsf, and at 27.14 mbsf on the upper part of the studied hole, suggesting that Hole M0058A is mainly characterized by low coercive magnetic minerals with the influence of magnetic minerals of varying coercivities (Fig. 2). Measurements performed at the lower part of the section show wasp wasp-waisted hysteresis cycles at 36.10 mbsf and at 38.64 mbsf, suggesting the presence of a mixture of magnetic minerals of varying coercivities at these intervals.

5.3.1.2. First Order Reversal Curves (FORCs)

FORCs were measured to understand the magnetostatic interaction, domain size and coercivity distribution of the magnetic grains (Fig. 2 and S4; Roberts et al., 2000; 2014). Samples show the presence of single domain to pseudo-single domain magnetic particles with the low coercivity distribution (Fig. 2 and S4). The magnetostatic interactions on the Bu axis vary between 10 - 60 mT and increase downcore (Fig. 2 and S4). FORCs of samples located at 7.19 mbsf, 17.84 mbsf and 27.14 mbsf (7 ka, 85 ka and 123 ka, respectively; Fig. 2 and S4) show similar coercivity ranges on the B_c-axis and negligible to few mT magnetostatic interaction on the Bu-axis indicating the presence of single domain magnetite. The FORCs for the samples located at 36.10 mbsf and 38.64 mbsf (ca. 180 ka and 200 ka, respectively; Fig. 2 and S4) show bulging contours from the central ridge on the Bu-axis, which is interpreted as the mixture of magnetic minerals (Fig. 2 and S4).

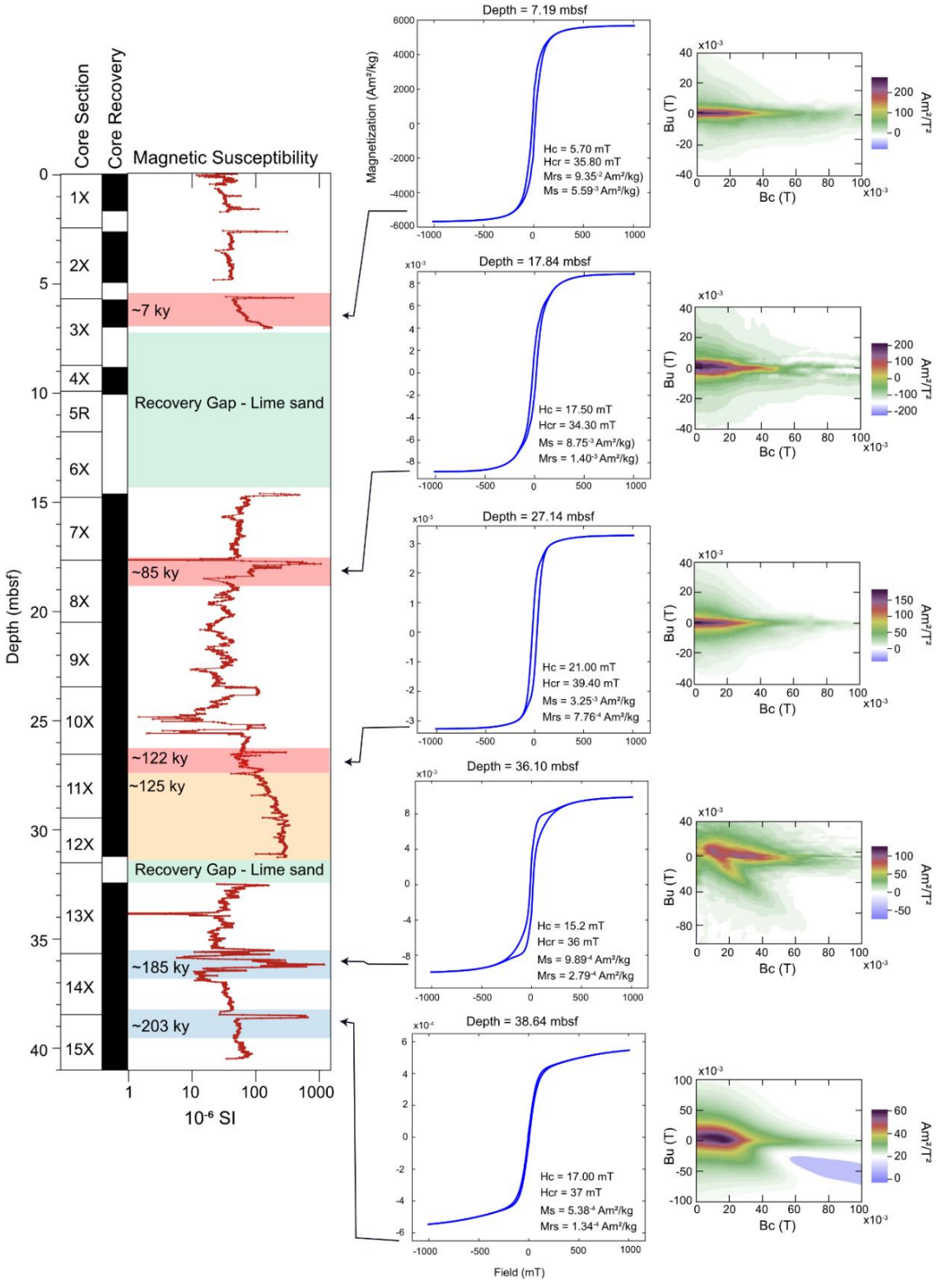

Fig. 2. Magnetic susceptibility vs. hysteresis cycles and First Order Reversal Curves (FORCs) at five different depths along the Hole M0058A section. The samples located on the lower parts of the section (38.64 mbsf and 36.10 mbsf) present distinct magnetic characteristics in comparison to the upper section samples (27.14 mbsf, 17.84 mbsf and 7.19 mbsf). The lower part (38.64 mbsf and 36.10 mbsf) is characterized by the mixture of high and low coercivity magnetic components (Pseudosingle domain to multi domain) whereas the upper part of the section (27.14 mbsf, 17.84 mbsf and 7.19 mbsf) is characterized by a single magnetic domain, low coercivity components.

5.3.1.3. Thermomagnetic Curves

The heating curves show an increase in magnetic susceptibility between 300 - 350°C because of the thermochemical alteration of clay minerals (Kostadinova-Avramova and Kovacheva, 2013; Jiang et al., 2015), after which the magnetization sharply reduces between 560 - 580°C indicating the presence of low-titanium magnetite (Fig. 3). At 36.14 mbsf, the Hopkinson peak can also be observed starting a gradual increase in susceptibility at 550°C. The cooling curves are irreversible for almost all samples. The cooling curve for the sample at 36.10 mbsf also shows an increase in magnetic susceptibility between 350-500°C (Fig. 3), indicating the formation of newly formed iron sulfide minerals.

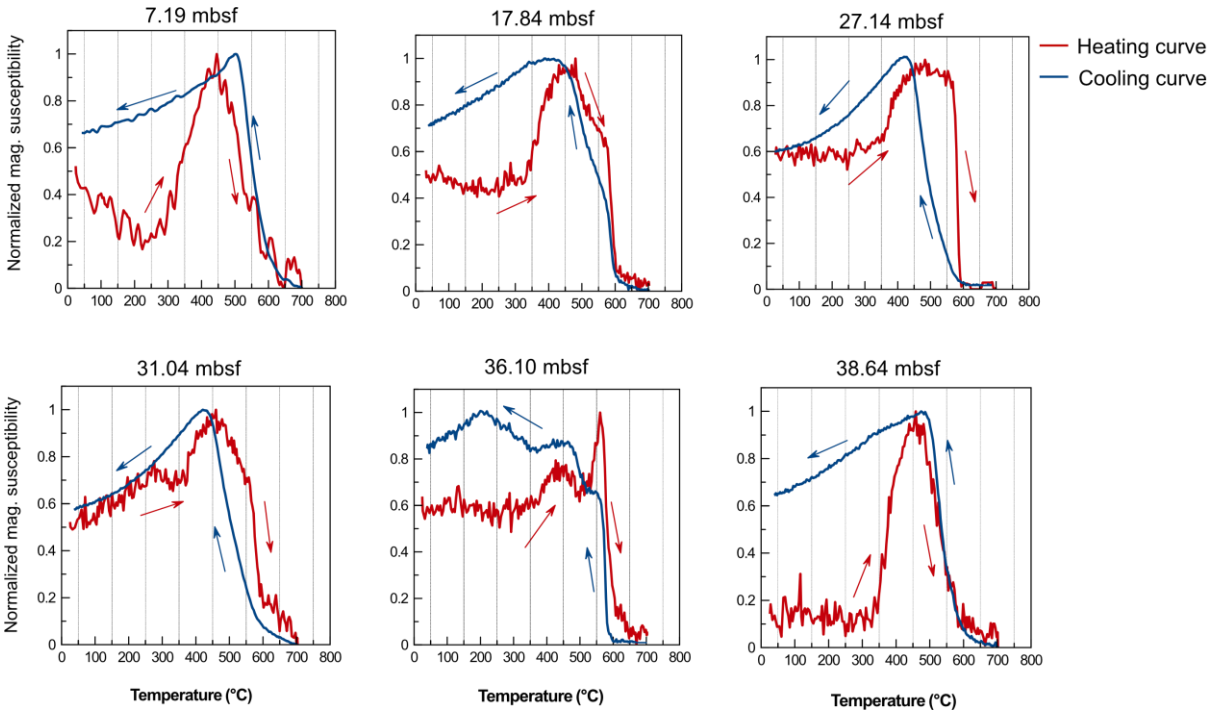

Fig. 3. Thermomagnetic curves at different depths along Hole M0058A. Red curves show increasing temperature vs. maximum normalized low field magnetic susceptibility while the blue curves show decreasing temperatures vs. maximum normalized magnetic susceptibility.

5.3.1.4. Day plot

Since magnetite is the dominant magnetic mineral, the domain states of the magnetic particles within the samples can be inferred with the use of Day plots (Day et al., 1977), in which parameters obtained by the hysteresis loop are investigated. Hysteresis ratios (M_{rs}/M_s and H_{cr}/H_c) of the majority of samples are grouped in the single-domain (SD) to Pseudo single domain-PSD region of the day plot (Fig. 4). Few samples fall in the superparamagnetic

region (Fig. 4; Dunlop, 2002), while others present mostly either pure single domain or pseudo-single domain behavior (Fig. 4).

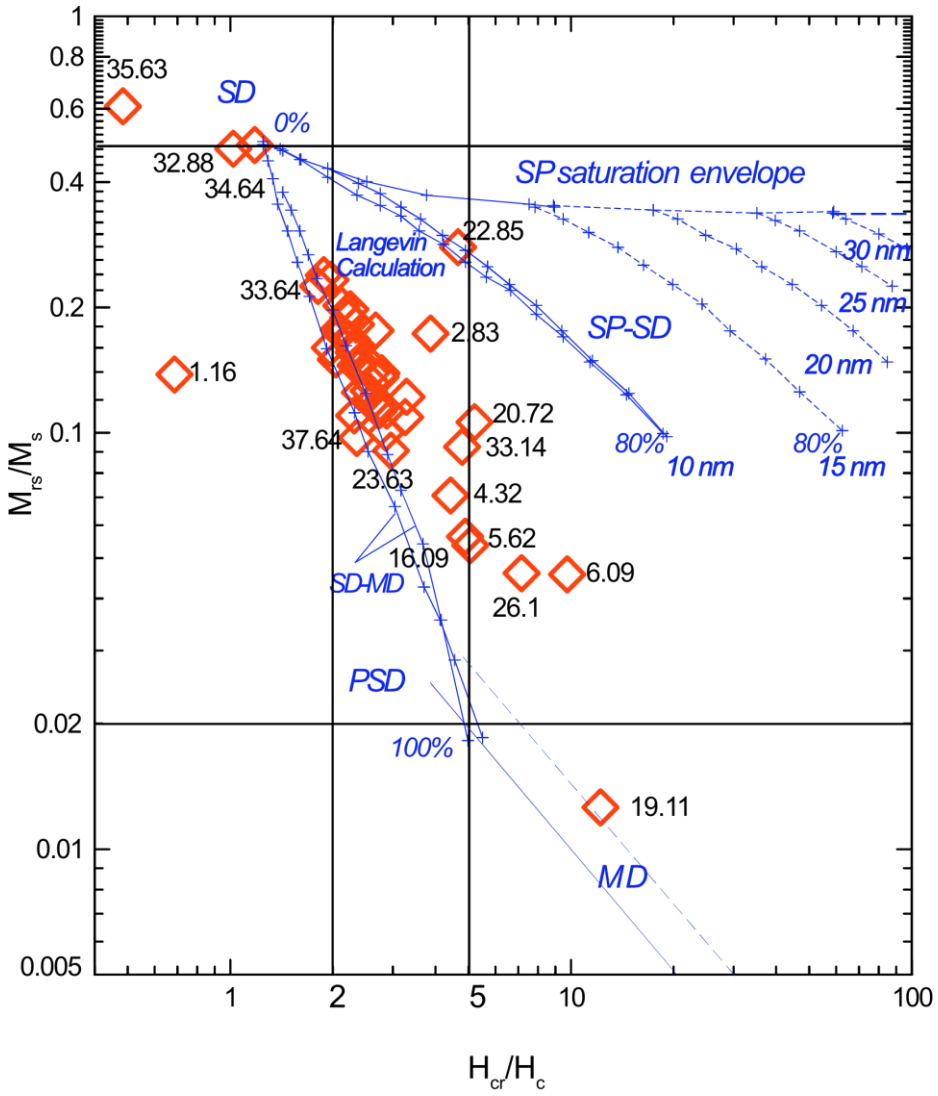

Fig. 4. Day plot obtained by extracting the hysteresis parameters such as M_{rs}/M_s and H_{cr}/H_c. Numbers beside each block show the depth of the discrete samples collected for magnetic measurements. The Day plot shows that almost all magnetite grains are pseudo-single domain to single domain, and very few samples are superparamagnetic. Blue data shows theoretical day plot curves for magnetite (Dunlop, 2002). SD – single domain; MD – multidomain; PSD – pseudo-single domain; SP – superparamagnetic.

5.3.2. Environmental Magnetism

Here we report environmental magnetic parameters, such as magnetic susceptibility, ARM, IRM, and calculated coercivity and magnetic grain size parameters (HIRM, S-ratio and ARM/IRM) along the core section, which allow a comparison between the different magnetic properties present at Hole M0058A (Fig. 5).

The high-resolution low-field magnetic susceptibility performed on u-channels is the result of all magnetic minerals in response to an applied magnetic field, which averages between $10x10^{-6}$ to 1000 $x10^{-6}$ SI (Fig. 5). However, from the base to the top of the Hole, it is possible to recognize an abrupt increase in magnetic susceptibility between 39 - 38 mbsf, which corresponds to the age of ca. 200 ka. A peak in magnetic susceptibility can also be observed between 35.5 - 36.5 mbsf, at ca. 180 ka. After that, an abrupt increase is observed at ca. 157 ka, followed by a steady reduction in susceptibility values until the top of the sand interval at 26.5 mbsf (ca. 123 ka). Peaks in magnetic susceptibility values are then observed at 6 mbsf, 15 mbsf, and 18 mbsf, which correspond to the ages of ca. 7 ka, ca. 82 ka and ca. 85 ka, respectively.

ARM oscillates between 0.01 to 10 x 10^{-6} A/m. Variations among the values of ARM clearly correspond to the above-mentioned variations in magnetic susceptibility. Moreover, increasing the applied magnetic field decreases the ARM intensity values (Fig. 5). IRM values vary between 0.0001 and 0.01 A/m corresponding to the same trend as the magnetic susceptibility and ARM. Magnetic data for IRM and HIRM curves at 25 mbsf, 36 mbsf and 39 mbsf have been affected by magnetic flux jump during the measurements, which is related to increased water content in u-channels (shown as dark arrows in Fig. 5).

The HIRM (Hard Isothermal Remanent Magnetization) values represent the relative magnetic composition (high coercivity vs low coercivity minerals) along the core section. Variations in HIRM correspond to the variations of IRM indicating that magnetic composition is overall constant except for a few intervals (at ~7 mbsf and between ~27 – 31 mbsf) where different magnetic minerals and magnetic grain sizes are observed (Fig. 5). Since the HIRMs are derived from IRM, the flux jumps mentioned previously (25 mbsf, 36 mbsf and 39 mbsf) can also be observed in the HIRM atypical values (Fig. 5).

S-ratio describes the proportion of high/low coercivity minerals (e.g., hematite/magnetite). The S-ratio shows that the dominant magnetic minerals in the core section are low-coercivity minerals (Fig. 5). However, the low values of S-ratio at ~7 mbsf and between ~27 - 31 mbsf indicate the presence of high coercivity minerals at these levels.

The ARM/IRM and ARM/k ratios are sensitive to changes in the grain size of the magnetic minerals, since the coarser the magnetic grain size is, the lower the ARM/IRM and ARM/k ratios are. ARM/IRM values vary between 0 - 1000 along the core while ARM/k values range

between 0 and 0.3 (Fig. 5). ARM/IRM and ARM/k show the highest values at intervals of ~7 mbsf and between ~27 - 31 mbsf, which indicates the presence of fine magnetic minerals at these intervals. Interestingly, the ARM/IRM and ARM/k values show a gradual increase between ~27 - 31 mbsf, which indicates a gradual enrichment of the fine fraction at this level (Fig. 5).

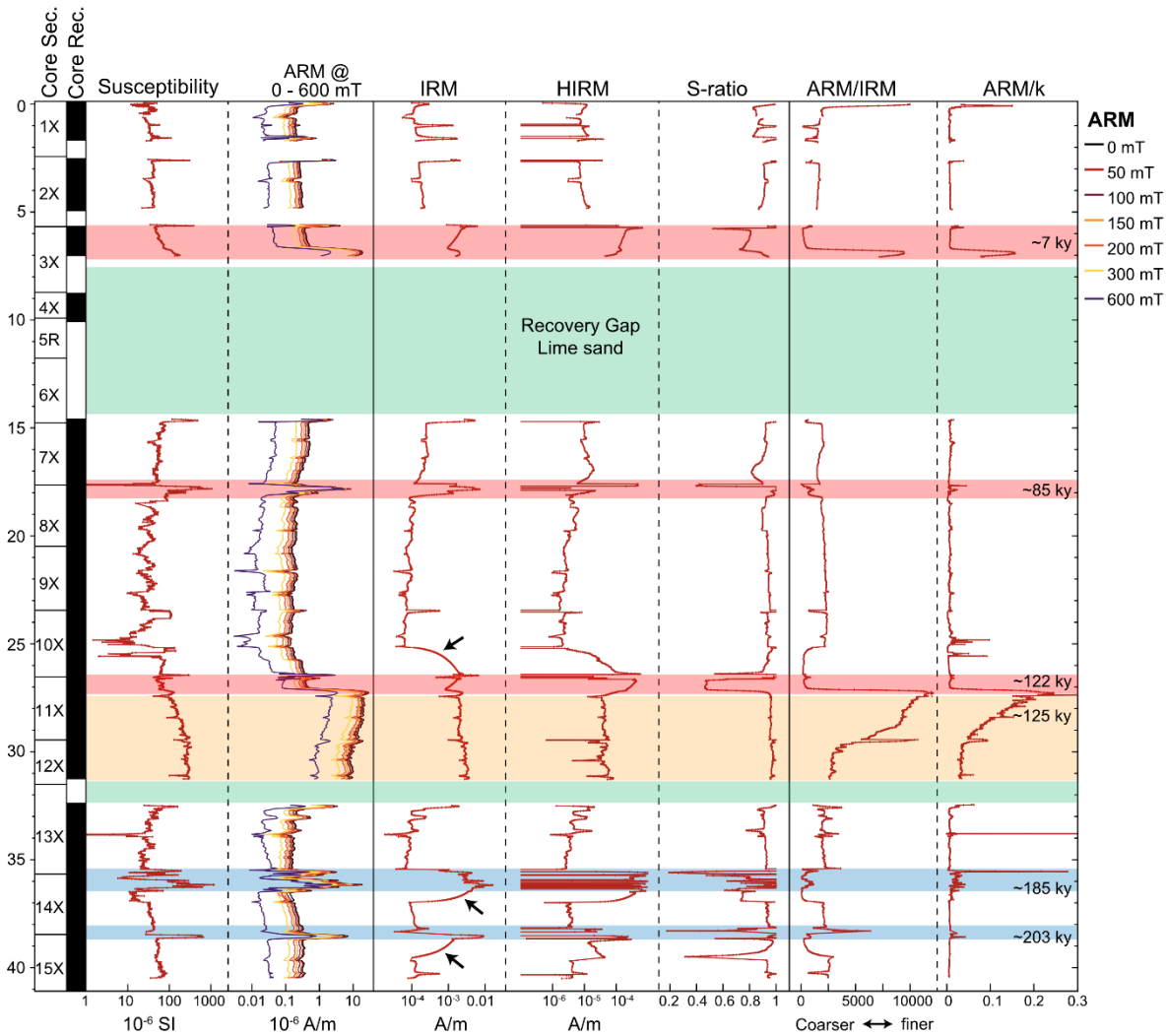

Fig. 5. Magnetic parameters along the Hole M0058A section: Left to right; Magnetic susceptibility, anhysteretic remanent magnetization (ARM) at 0 mT, ARM at 0-600 mT; isothermal remanent magnetization (IRM), Hard IRM (HIRM), and calculated parameters: S-ratio and magnetic grain size parameters (i.e., ARM/IRM and ARM/k). Black arrows indicate uninterpreted steady data caused by either flux jump during measurement or increased water content. Magnetic data show three distinct patterns: 1 - at ca. 203 ka and ca. 185 ka (blue bars), peak magnetic values are associated with coarse-grained mixture of low and high coercivity magnetic components (e.g., magnetite and hematite); 2 - at ca. 125 ka (yellow bar), peak magnetic data is associated with finer magnetite; 3 - at ca. 122 ka, 85 ka and 7 ka (red bars) peak magnetic data are associated with finer biogenic magnetite and occasional coarser hematite.

5.3.3. Geochemistry

5.3.3.1. X-Ray Fluorescence Geochemical Proxies

The elemental ratio Ca/Ti is a common proxy to assess the alternations between biogenic and lithogenic sedimentation since Calcium is present within the carbonates while Titanium is a continental-derived element enriched within the terrigenous fraction in marine environments (Piva et al., 2008; Rothwell, 2015). From the bottom to the top of Hole M0058A, short-lived intervals of Ca/Ti depletion (at ca. 215 and 195 ka) and enrichment (at ca. 205 and 185 ka) can be clearly observed. Ca/Ti values are constant from ca. 160 ka towards an abrupt change between ca. 134 – 120 ka, which also correlates with important changes in magnetic parameters (Fig. 5). High Ca/Ti values are observed from ca. 120 – 85 ka, with peak values between ca. 120 – 100 ka. The Ca/Ti ratio also increases between ca. 19 -15 ka. Concentration values for Si, Fe, Mn, Al and the Fe/K ratio (i.e., terrigenous proxy) show opposite trends in comparison to the Ca/Ti ratios, which further demonstrates the alternation pattern between biogenic and lithogenic sedimentation in the region (Fig. 6 and S2).

5.3.3.2. X-Ray Diffraction Bulk Mineralogy

The bulk mineralogy of Hole M0058A is dominated by quartz, calcite, aragonite, and magnesium calcite (Fig. S3). Throughout the core sections, bulk mineralogy follows the expected variations predicted from X-ray fluorescence measurements (Fig. 6 and S2). Quartz and calcite alternate with each other while the concentration of magnesium calcite correlates positively with changes in calcite concentrations. Aragonite and magnesium calcite present a similar trend along the core sections (Fig. S3).

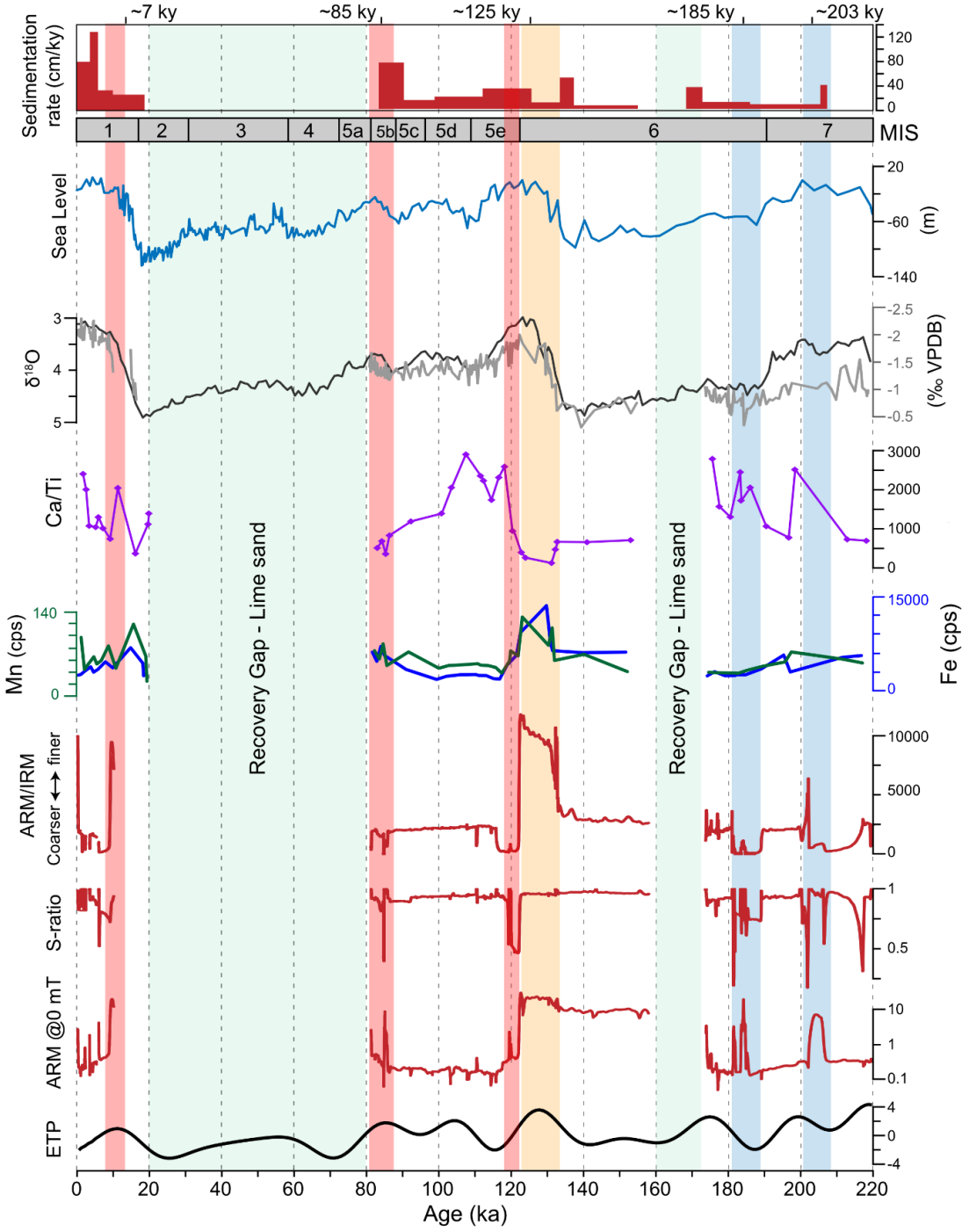

Fig. 6. Comparison of Hole M0058A sedimentation rates, magnetic and geochemical records with global sea-level (Miller et al., 2020), oxygen isotope (black - Lisiecki et al., 2005; gray - Harper et al., 2015) and the orbital composite curve (ETP - Eccentricity-Obliquity-Precession 1:1:1 relative weight; Laskar et al., 2011). Sedimentation rates and Ca/Ti proxy show that periods of carbonate deposition occurred during intervals of higher temperatures and sea levels of the Marine Isotope Stages (MIS) 5 and 1 (i.e., interglacials) while the MIS 6 and MIS 4-2 cooling intervals (i.e., glacials) were accompanied by reduced carbonate and the deposition of unconsolidated terrigenous sands (recovery gaps, green bars). Magnetic data show three distinct patterns: 1 - at ca. 203 ka and ca. 185 ka (blue bars), peak magnetic values are associated with coarse grained mixture of low and high coercivity magnetic components, cooling temperatures and sea-level fall; 2 - at ca. 125 ka (yellow bar), peak magnetic data is associated with finer magnetite, Iron and manganese enrichment, rising temperatures and sea-level; 3 - at ca. 122 ka, 85 ka and ca. 7 ka (red bars), peak magnetic values are associated with finer biogenic magnetite as a result of iron fertilization by the wind-blown dust.

5.4 Discussion

5.4.1. Magnetic Evidence for Terrigenous Influxes at Hole M0058A

A model for mixed siliciclastic-carbonate sedimentation at Hole M0058A has been previously proposed by Harper et al. (2015). Based on sedimentology, physical properties, and elemental and isotopic geochemistry, these authors described two dominant alternating sediment deposits: one formed by terrigenous siliciclastics and the second formed by neritic rich carbonates (Harper et al., 2015). Magnetic results shown here provide further details regarding the depositional patterns and the origin of sediments at Hole M0058A.

Based on our new rock magnetic data, we characterize biogenic magnetite as a primary magnetic mineral in the upper part of the sedimentary succession, as observed in samples at 7.19 mbsf, 17.84 mbsf and 27.14 mbsf (ca. 7, 85, 125 ka, respectively; Fig. 2 and 3). The presence of biogenic magnetite has also been reported by Barton et al. (1993a; 1993b) and Yokohama et al. (2011) for the same region. Furthermore, Abrajevitch and Kodama (2011) reported the presence of biogenic magnetite at ODP Site 820 at similar stratigraphic intervals (from the top to 32 mbsf). On the other hand, the lower part of the sedimentary succession contains a mixture of magnetic minerals, as seen at 36.10 mbsf and 38.64 mbsf (ca. 180 and 200 ka, respectively; Fig. 2 and 3), which are linked to more resistant high coercivity minerals (Abrajevitch and Kodama, 2011).

Multiple studies have related the variability in magnetic parameters such as magnetic susceptibility, ARM, IRM and their derivatives (HIRM, ARM/IRM and S-ratio) to paleoceanographic and paleoclimatic changes (Arai et al., 1997; Moreno et al., 2002; Oldfield et al., 2003; Larrasoaña et al., 2015). At Hole M0058A, these environmental magnetic parameters are related to the significant variations of sedimentary properties in the sedimentary succession (Fig. 5). Magnetic results indicate that a substantial correlation exists between magnetic curves related to magnetic concentration (magnetic susceptibility and ARM), magnetic composition (IRM, HIRM and S-ratio), and magnetic grain size (ARM/IRM and ARM/k). This implies that the sediments have uniform magnetic properties through the record exhibiting cyclic fluctuations in response to paleoceanographic and paleoenvironmental changes (Fig. 5).

Changes in the magnetic and geochemical properties at Hole M0058A show three different associations of sedimentary compositions (Fig. 2, 5 and 6): 1) higher magnetic concentration (magnetic susceptibility and ARM), higher neritic carbonate sedimentation (higher Ca/Ti) and sea-level rise leading to sea-level fall (blue bars in fig. 5 and 6); 2) high magnetic concentration

(magnetic susceptibility and ARM), higher terrigenous input (low Ca/Ti and high Fe and Mn) and sea-level highstand (yellow bar in fig. 5 and 6); 3) mixed magnetic composition (IRM, HIRM and S-ratio) with the presence of biogenic magnetite, finer magnetic grain sizes and the presence of wind-blown high coercivity magnetic components (low S-ratios) under higher temperatures (red bars in fig. 5 and 6).

From the bottom of the section at ca. 220 ka to ca. 175 ka, all magnetic parameters exhibit a correlation between magnetic and geochemical variations (blue bars in fig. 5 and 6). The increase in magnetic concentration (magnetic susceptibility and ARM) is accompanied by an alternation between high and low coercivity minerals (S-ratio and HIRM) and changes in grain size (ARM/IRM). These events of enhanced magnetic concentration also occurred during periods of orbital insolation lows (Fig. 6). While carbonate sedimentation increased during these periods, Fe and Mn contents remained relatively stable, indicating constant terrigenous input. However, magnetic properties' highs and lows amplified at this interval, which could be explained by enhanced remobilization and mixing of fine and coarse grained high coercivity magnetic minerals during the glacial period at the end of MIS 7 and early MIS 6 (210 - 180 ka; Fig. 5 and 6; Bloemendal et al., 1988; Just et al., 2012).

Around ca. 130 ka (yellow bars: Fig. 5 and 6), at the end of the glacial period of MIS 6 after the onset of deglaciation (Termination II) an increase in finer magnetic grains (ARM/IRM) and terrigenous elements (Fe, Mn, Ti, Al and Si) is observed, but magnetic composition (S-ratio) was initially not affected. This suggests that terrigenous input increased at this level, particularly finer terrigenous fractions (Fig. 5 and 6). Carbonate content also declined significantly at this level, potentially affected by sediment dilution under the enhanced terrigenous deposition (lower Ca/Ti; Fig. 6). This event coincides with rapid warming and sea-level rise (Fig. 6). This reciprocal sedimentation model is consistent with the ones proposed by Dunbar and Dickens (2003) and Harper et al. (2015). After that event, a drastic shift in S-ratio and a sudden decrease in ARM/IRM ratios then occurred at ca. 125 ka, which represents a change towards coarse-grained high coercivity magnetic minerals, probably hematite (Fig. 5 and 6). We interpret that this short-term and abrupt shift in S-ratio reflects a change in the sourcing of terrigenous sediments during the interglacial highstand after Termination II, with the presence of wind-blown high coercivity dust particles (e.g., hematite). We suggest that such mineralogical changes are associated with the climatic changes from glacial to the interglacial conditions of Termination II, which increased continental aridity and wind intensity which subsequently triggered a vegetation crisis in the hinterland (Schmidt, 2001). Such changes in the magnetic properties of the sediments during Termination I and II have also been observed

in southwest Greenland, while the deglaciation of Termination II was rapid, the deglaciation of Termination I lasted over 2 stages (Stoner et al., 1995). Carbonate content then drastically recovered at ca. 120 ka after the warming peak of Termination II (Fig. 6).

Between ca. 115 - 88 ka (27 - 18 mbsf), magnetic parameters show more stable conditions, which are interpreted as a dilution effect of the magnetic influx through the increase in carbonate deposition, which is consistent with previous studies (Barton et al., 1993b; McNeill, 1993; 1993b), however, this phenomenon only occurred between MIS 5d and 5a, when carbonate deposition peaked (Fig. 5 and 6).

Between ca. 88 - 80 ka, and then again at ca. 7 ka, two brief intervals marked by the presence of biogenic magnetite (Fig. 2) and high coercivity magnetic components occurred (red bars in Fig. 5). In addition, these two intervals occurred during relative short-term sea-level rises and warming trends (Fig. 6). An increase in ARM and IRM, with a change towards finer magnetic grain size (ARM/IRM) and a shift towards lower values for magnetic composition (S-ratio), are also observed (Fig. 5 and 6). This association indicates the increasing presence of finer low-coercivity magnetic components signifying a constant decrease of the terrigenous input and/or intensification of the arid conditions during the glacial period. The Last glacial period culminates with the presence of wind-blown dust particles characterized by high-coercivity magnetic minerals (e.g., hematite) (Fig. 5 and 6; Molodkov et al., 2006; Kees et al., 2016; Humphries et al., 2017; Lewis et al., 2021). The presence of biogenic magnetite produced by magnetotactic bacteria (Jovane et al., 2012; Savian et al., 2014) combined with a higher dust component may indicate enhanced primary productivity through dust fertilization during this period (Fig. 5 and 6). Similar links between the presence of wind-blown dust particles and the occurrence of biogenic magnetite have been previously recognized in the Paleocene and Eocene pelagic sediments from the Southern Ocean (Roberts et al., 2011; Larrasoaña et al., 2012), in the Paleocene-Eocene sediments from the Indian Ocean (Roberts et al., 2013; Savian et al., 2016), in the Quaternary sediments from the Southwest Iberian Margin (Channell et al., 2013), in the Quaternary sediments from the Mediterranean sea (Dinarès-Turell et al., 2003) and in Quaternary aeolian sediments (Maher, 2011).

5.4.2. Pleistocene-Holocene Sea level and Monsoonal impacts on the GBR

The last 220 ka interval covered in this study is marked by the onset and the end of two glaciation cycles (Fig. 6), the MIS 6 between ca. 190 - 129 ka (Penultimate Glacial Maximum) and the middle to late Holocene (MIS 4-2 between ca. 74 - 12 ka, Last Glacial Maximum). These glaciation events occurred adjacent to the warmer interglacials of the MIS 7 and MIS 5

of the Pleistocene, and the MIS 1 of the Holocene (Fig. 6). Paced at the long eccentricity astronomical frequencies (ca. 100 ka), variations in ice volume at these glacial-interglacial cycles regulated the Quaternary variations in sea-level (Fig. 6; Shackleton, 2000; Lisiecki, 2010; Imbrie et al., 2011; Spratt and Lisiecki, 2015) and the latitudinal displacements of the Intertropical Convergence Zone (ITCZ), which controls precipitation patterns along the equatorial regions (i.e., the monsoons; Rutherford and D'Hondt, 2000; Ao et al., 2012; Peng et al., 2020).

Global sea-level fluctuations during the late Quaternary varied by more than 100 m across glacial-interglacial transitions (Waelbroek et al., 2002; Rohling et al., 2009; Miller et al., 2020). In the GBR region, Yokoyama et al., (2018) reported a ca. 80 m sea-level change between the LGM and the late Holocene transgression. Sea-level at ca. 20 ka was ca. -120 m relative to modern levels (Yokoyama et al., 2018). Those sea-level lowstands exposed the shelf areas, including the carbonate factories of the GBR (Page et al., 2003; Webster et al., 2018). It has also been documented that NE Australia experienced shoreline progradation, channel incision and an influx of terrigenous material during MIS glacial events, which established the presence of deltaic environments within the GBR (Johnson et al., 1982; Johnson and Searle, 1984; Page and Dickens, 2005; Daniell et al., 2020). On the other hand, Quaternary deglaciations and the subsequent sea-level rise resulted in an enriched carbonate accumulation on the shelf via reef build-up, a landward displacement trend of reefs to shallower regions, and a transition of reef assemblages towards more high-energy resistant, shallow coralgal assemblages (Page et al., 2003; Webster et al., 2018; Humblet et al., 2019). However, the mixed depositional nature of the continental margin around the GBR (i.e., siliciclastic and carbonate system) adds complexity to this generic model of increased terrigenous input during glaciation and sea-level fall. For example, several studies show that the Holocene sea-level rise was accompanied by an increase of terrigenous material transported to the slope (Dunbar et al., 2000; Dunbar and Dickens 2003). Page et al. (2003) suggested that an enrichment of terrigenous input to the GBR slope during sea-level rise occurred because the previous sea-level fall had trapped siliciclastic material within the inner platform/coastal lagoon system, such that the Holocene transgression enabled vast remobilization of siliciclastic material pre-deposited via tides, wave, and storm activity resulting in a model of reciprocal sedimentation (Page et al., 2003).

Moreover, modern Northern Australia is under the influence of the seasonal monsoon via the southward displacement of the ITCZ during the summer (Magee et al., 2004), which results in a dual climate-vegetation pattern with moist summers and dry winters. Proxy records from marine sediment cores indicate that a paleo analogue to the modern monsoon was

already active since the late Miocene in Asia, Arabia and Australia (ca. 12.9 Ma; Qiang et al., 2001; Moss et al., 2005; Betzler et al., 2016; Tripathi et al., 2017; Karatsolis et al., 2019), but such dual climate patterns were amplified during the glacial-interglacial cycles of the Quaternary (Nanson et al., 1992; Ayliffe et al., 1998; Kershaw et al., 2003; Hesse et al., 2004). This resulted in heightened aridification during glaciations (i.e., enhanced dust input) whilst precipitation and surface runoff increased during interglacials (Nanson et al., 1993; Wyrwoll and Miller, 2001; Hallenberger et al., 2019; Petrick et al., 2019; Courtillat et al., 2020).

Our results highlight the changes in sediment delivery to the GBR over the last 220 ka and its relationship with sea-level trends and regional climate patterns. The lowest sea level and coldest intervals of the last 220 ka occurred at ca. 140 ka in the MIS 6 and ca. 20 ka in the MIS 2 (ca. -80 m and ca. -120 m relative to the present, respectively; Yokoyama et al., 2018; Miller et al., 2020). Orbital insolation was at its lowest points of the last 200 ka at those intervals, at the short eccentricity minima of ca. 50 ka and 150 ka (Fig. 6; Laskar et al., 2011). At Hole M0058A, these two intervals are marked by the presence of two long recovery gaps that occurred due to the presence of unconsolidated quartzose sands (i.e., terrigenous input; Fig. S1 and 6; Webster et al., 2011; Harper et al., 2015). This correlation between sea-level cycles and sedimentological changes at Hole M0058A is further seen at the geochemical proxy Ca/Ti, which represents carbonate/siliciclastic compositional changes. Ca/Ti values are generally higher during the relatively higher sea-level intervals between ca. 220 - 175 ka (MIS 7 to early 6), ca. 120 - 100 ka (MIS 5e-d) and ca. 7 ka (MIS 1), while lower (i.e., more terrigenous sediments) between ca. 150 - 120 ka (MIS 6). The XRF results are consistent with the geochemical results of Harper et al., (2015), which suggested that Quaternary sea-level lowstands resulted in deltaic progradation over the carbonate platforms (at least between the exposed reefs) of GBR, which thus triggered carbonate platform shutdown and the dominance of siliciclastic sand deposition. On the contrary, late Quaternary interglacials and their sea-level rises resulted in shoreline retrogradation, lowered terrigenous deposition, and the growth of carbonate reefs. These results highlight a dominant control of sea level on the type of sedimentation across the GBR margin.

Magnetic parameters confirm and extend the geochemical interpretations regarding the late Quaternary evolution of the GBR margin. More importantly, the magnetic parameters can reveal potential changes in the provenance and grain size of the terrigenous components. In general, variations in magnetic parameters at Hole M0058A occurred during intervals of important changes in monsoonal state and sea-levels. Mixed magnetic compositions and varying grain sizes (blue bars in Fig. 5) occurred because of mixing and remobilization of

sediments, while finer magnetite indicated terrigenous input during warming conditions, rising sea-level and orbital maxima. Such correlation between magnetic properties and warming/cooling trends in the GBR margin was also observed at Site ODP 820A (Barton et al., 1993a and b; Glenn et al., 1993). Biogenic magnetite is the result of primary productivity triggered by the continental dust input. Furthermore, a negative correlation existed between magnetic susceptibility and ARM with orbital eccentricity between 220 - 180 ka, with increased susceptibility and ARM occurring during cooling (low) orbital eccentricity intervals (blue bars in Fig. 5 and 6). However, this antiphase correlation changed to a positive/phase correlation from 180 ka onwards, with rising susceptibility and ARM concomitant to global warming intervals (yellow and red bars of Fig. 5 and 6).

We interpret that the correlation between magnetic parameters and global monsoon/sea levels represents the formation and demise of three distinct depositional environments over the GBR across the late Quaternary glacial-interglacials:

1. *Sea-level changes controlled margin deposition between MIS 7 and MIS 6 (blue bars)*
   In the relative colder interval between MIS 7 and MIS 6 (ca. -1 to -8 °C relative to present between 220 - 140 ka), the margin was mainly affected by the changing sea level and its effect on shoreline progradation/retrogradation and siliciclastic redistribution. Orbital eccentricity lows and relative sea-level fall exposed the shelf, which resulted in the remobilization of finer to coarser magnetic components of varying coercivities, and proximal siliciclastic grains to the slope. Terrigenous provenance did not change significantly between MIS 7 and MIS 6 which suggests a limited effect of the summer monsoon over the GBR during this interval.
2. *Monsoon Intensification in the GBR glacial/interglacial transition (MIS 6-5e) (yellow bar)*
   At the end of MIS 6 (+5 °C relative to present at ca. 125 ka), a large increase in the deposition of terrigenous sediments (both the total fraction but in particular the finer fraction) occurred concomitantly with a rapid rise in sea-level and global temperatures. We interpret that such a depositional pattern likely represents the increased impact of the summer monsoon over the GBR at the end of MIS 6 when the ITCZ was potentially at its southernmost position. Enhanced continental precipitation strengthened surface runoff towards the margin where shoreline retrogradation further promoted the deposition of the finer fraction.
3. *Aridification of NE Australia during MIS 5 and MIS 1 (red bars)*

At ca. 122 ka, during the onset of interglacial MIS 5e, the magnetic parameter S-ratio indicated a provenance change in the terrigenous composition towards high coercivity magnetic component (e.g., hematite), which is usually associated with aeolian transport. This pattern further occurred during the orbital maxima of ca. 85 ka and at the middle Holocene at ca. 7 ka, concomitant with warming trends and sea-level rise. We interpret that NE Australia was more arid during the last Interglacial (MIS 5) and middle Holocene (in comparison to the previous Interglacials), which promoted dust input (e.g, hematite-rich) over surface runoff (magnetite-rich) in the GBR. Enhanced dust fertilization in the oceans subsequently promoted primary productivity in the region, with the appearance of magnetotactic bacteria on the ocean floor. The more arid conditions observed since ca. 122 ka may be associated with an ITCZ displaced further north during these intervals, such that NE Australia remained under the influence of stronger than usual trade winds (De Deckker et al., 1991). That interpretation is consistent with other records that show an increase in the aridification of northern Australia during the late Pleistocene (Hesse and McTainsh, 2003; Pei et al., 2021), potentially driven by the gradual expansion of Antarctic ice sheets throughout the late Cenozoic cooling (Petit et al., 1999; Lambert et al., 2008).

5.5. Conclusions

Geochemical and magnetic study of the Late Quaternary sediments from the Hole M0058A (IODP Expedition 325) represents an opportunity to reveal the environmental processes that shaped the Great Barrier Reef during the Pleistocene and Holocene. Magnetic and geochemical changes throughout the sedimentary succession indicate different associations of sediment accumulation patterns for the past 220 ka.

Between MIS 7 and MIS 6, we identified an increase in the mixture of magnetic minerals and neritic carbonate sediments. This interval is a response to the orbital eccentricity lows and relative sea-level fall, which exposed the shelf and triggered the remobilization of magnetic components of varying coercivities and distinct magnetic grain sizes. Terrigenous provenance did not change significantly during this period which suggests a limited effect of the Australian monsoon over the GBR at the time. Hence, sedimentary processes in the GBR during the MIS 7 and 6 were mostly controlled by sea-level fluctuations that triggered shoreline progradation/retrogradation trends and a subsequent redistribution of siliciclastic sediments across the shelf.

At the end of MIS 6 (rising sea-level and warming trends), we identified a gradual increase in magnetic properties concomitant with an increase in terrigenous input. This phenomenon represents the onset of the Australian monsoon influence over the sediment accumulation at the GBR. The ITCZ was at its southernmost position, which strengthened surface runoff and the transport of siliciclastic sediments to the margin. Shoreline retrogradation further promoted the deposition of the finer fractions of magnetite.

After the glacial-interglacial transition of MIS 6-5e (ca. 122 ka) and at the peak warm phases of ca. 85 ka and ca. 7 ka we identified high coercivity magnetic components (i.e., hematite) and biogenic magnetite. These events occurred due to a change in the provenance of the terrigenous fraction, with the presence of finer hematite likely associated with an increased deposition of aeolian sediments. Enhanced dust fertilization then increased primary productivity in the area which resulted in the appearance of magnetotactic bacteria in the sea floor sediments. Therefore, more arid conditions were in place over NE Australia at these intervals, which indicates a diminished influence of the Australian Monsoon over the GBR during peak warm phases of the late Pleistocene and Holocene (i.e., ITCZ displaced further north).

References

Abbey, E., Webster, J. M., & Beaman, R. J. (2011). Geomorphology of submerged reefs on the shelf edge of the Great Barrier Reef: the influence of oscillating Pleistocene sea-levels. *Marine Geology*, *288*(1-4), 61-78. https://doi.org/10.1016/j.margeo.2011.08.006

Abrajevitch, A., & Kodama, K. (2011). Diagenetic sensitivity of paleoenvironmental proxies: A rock magnetic study of Australian continental margin sediments. *Geochemistry, geophysics, geosystems*, *12*(5). https://doi.org/10.1029/2010GC003481

Ao, H., Dekkers, M. J., Xiao, G., Yang, X., Qin, L., Liu, X., Qiang, X., Chang, H., & Zhao, H. (2012). Different orbital rhythms in the Asian summer monsoon records from North and South China during the Pleistocene. *Global and Planetary Change*, *80*, 51-60. https://doi.org/10.1016/j.gloplacha.2011.09.012

Arai, K., Sakai, H., & Konishi, K. (1997). High-resolution rock-magnetic variability in shallow marine sediment: a sensitive paleoclimatic metronome. *Sedimentary Geology, 110*(1-2), 7-23. https://doi.org/10.1016/S0037-0738(96)00082-6

Ayliffe, L. K., Gagan, M. K., Zhao, J. X., Drysdale, R. N., Hellstrom, J. C., Hantoro, W. S., Griffiths, M. L., Scott-Gagan, H., Pierre, E. S., Cowley, J. A., & Suwargadi, B. W. (2013). Rapid interhemispheric climate links via the Australasian monsoon during the last deglaciation. *Nature communications*, *4*(1), 1-6. https://doi.org/10.1038/ncomms3908

Ayliffe, L. K., Marianelli, P. C., Moriarty, K. C., Wells, R. T., McCulloch, M. T., Mortimer, G. E., & Hellstrom, J. C. (1998). 500 ka precipitation record from southeastern Australia: evidence for interglacial relative aridity. *Geology*, *26*(2), 147-150. https://doi.org/10.1016/j.yqres.2008.02.013

Bannister, R. J., Battershill, C. N., & De Nys, R. (2012). Suspended sediment grain size and mineralogy across the continental shelf of the Great Barrier Reef: Impacts on the physiology of a coral reef sponge. *Continental Shelf Research*, *32*, 86-95. https://doi.org/10.1016/j.csr.2011.10.018

Barton, C. E. (1993b). Paleomagnetic and mineral magnetic record of sediments from the Queensland Trough: Results for Leg 133, Hole 823A, edited by JA McKenzie et al. In *Proc. Ocean Drill. Program Sci. Results* (Vol. 133, pp. 563-571). https://doi.org/10.2973/odp.proc.sr.133.262.1993

Barton, C. E., Lackie, M., & Peerdeman, F. M. (1993a). Environmental control of magnetic properties of upper-slope sediments near the Great Barrier Reef: results from Leg 133, Site 820. In *Proceedings of the Ocean Drilling Program, Scientific Results* (pp. 543-562). ODP, Texas A&M University, College Station. https://doi.org/10.2973/odp.proc.sr.133.261.1993

Beaman, R. J., Webster, J. M., & Wust, R. A. (2008). New evidence for drowned shelf edge reefs in the Great Barrier Reef, Australia. *Marine Geology*, *247*(1-2), 17-34. https://doi.org/10.1016/j.margeo.2007.08.001

Betzler, C., Eberli, G. P., Kroon, D., Wright, J. D., Swart, P. K., Nath, B. N., Alvarez-Zarikian, C. A., Alonso-Garciá, M., Bialik, O. M., Blättler, C. L., Guo, J. A., Haffen, S., Horozal, S., Inoue, M., Jovane, L., Lanci, L., Laya, J. C., Mee, A. L. H., Lüdmann, T., … Young, J. R. (2016). The abrupt onset of the modern South Asian Monsoon winds. *Scientific reports*, *6*(1), 1-10. https://doi.org/10.1038/srep29838

Bloemendal, J., Lamb, B., & King, J. (1988). Paleoenvironmental implications of rock-magnetic properties of Late Quaternary sediment cores from the eastern equatorial Atlantic. *Paleoceanography*, *3*(1), 61-87. https://doi.org/10.1029/PA003i001p00061

Brenner, L. D., Linsley, B. K., Webster, J. M., Potts, D., Felis, T., Gagan, M. K., ... & Yokoyama, Y. (2020). Coral record of Younger Dryas chronozone warmth on the Great Barrier Reef. *Paleoceanography and Paleoclimatology*, *35*(12), e2020PA003962. https://doi.org/10.1029/2020PA003962

Burckle, L. H. (1993). Late Quaternary interglacial stages warmer than present. *Quaternary Science Reviews*, *12*(10), 825-831. https://doi.org/10.1016/0277-3791(93)90021-D

Burke, K. D., Williams, J. W., Chandler, M. A., Haywood, A. M., Lunt, D. J., & Otto-Bliesner, B. L. (2018). Pliocene and Eocene provide best analogs for near-future climates. *Proceedings of the National Academy of Sciences*, *115*(52), 13288-13293. https://doi.org/10.1073/pnas.1809600115

Cai, W., & Cowan, T. (2013). Southeast Australia autumn rainfall reduction: A climate-change-induced poleward shift of ocean–atmosphere circulation. *Journal of Climate*, *26*(1), 189-205. https://doi.org/10.1175/JCLI-D-12-00035.1

Channell, J. E. T., Hodell, D. A., Margari, V., Skinner, L. C., Tzedakis, P. C., & Kesler, M. S. (2013). Biogenic magnetite, detrital hematite, and relative paleointensity in Quaternary sediments from the Southwest Iberian Margin. *Earth and Planetary Science Letters*, *376*, 99–109. https://doi.org/ 10.1016/J.EPSL.2013.06.026

Clark, P. U., He, F., Golledge, N. R., Mitrovica, J. X., Dutton, A., Hoffman, J. S., & Dendy, S. (2020). Oceanic forcing of penultimate deglacial and last interglacial sea-level rise. *Nature*, *577*(7792), 660-664. https://doi.org/10.1038/s41586-020-1931-7

Courtillat, M., Hallenberger, M., Bassetti, M. A., Aubert, D., Jeandel, C., Reuning, L., Korpanty, C., Moissette, P., Mounic, S., & Saavedra-Pellitero, M. (2020). New Record of Dust Input and Provenance During Glacial Periods in Western Australia Shelf (IODP Expedition 356, Site U1461) from the Middle to Late Pleistocene. *Atmosphere*, *11*(11), 1251. https://doi.org/10.3390/atmos11111251

Daniell, J., Manoy, T., Beaman, R. J., Webster, J. M., & Puga-Bernabéu, Á. (2020). Shelf-edge delta and reef development on a mixed siliciclastic–carbonate margin, central Great Barrier Reef. *Journal of Sedimentary Research*, *90*(10), 1286–1304. https://doi.org/10.2110/JSR.2020.61

Davies, P. J., Symonds, P. A., & Feary, D. A. (1988). Facies models in exploration—the carbonate platforms of north-east Australia. *The APPEA Journal*, *28*(1), 123-143. https://doi.org/10.1071/AJ87012

Day, R., Fuller, M., & Schmidt, V. A. (1977). Hysteresis properties of titanomagnetites: grain-size and compositional dependence. *Physics of the Earth and planetary interiors*, *13*(4), 260-267. https://doi.org/10.1016/0031-9201(77)90108-X

Dinarès-Turell, J., Hoogakker, B. A. A., Roberts, A. P., Rohling, E. J., & Sagnotti, L. (2003). Quaternary climatic control of biogenic magnetite production and eolian dust input in cores from the Mediterranean Sea. *Palaeogeography, Palaeoclimatology, Palaeoecology*, *190*, 195–209. https://doi.org/10.1016/S0031-0182(02)00605-3

De'ath, G., Lough, J. M., & Fabricius, K. E. (2009). Declining coral calcification on the Great Barrier Reef. *Science*, *323*(5910), 116-119. https//doi.org/10.1126/science.1165283

De Deckker, P., Corrège, T., & Head, J. (1991). Late Pleistocene record of cyclic eolian activity from tropical Australia suggesting the Younger Dryas is not an unusual climatic event. Geology, 19(6), 602-605.

https://doi.org/10.1130/0091 7613(1991)019<0602:LPROCE>2.3.CO;2

Dunbar, G. B., Dickens, G. R., & Carter, R. M. (2000). Sediment flux across the Great Barrier Reef Shelf to the Queensland Trough over the last 300 ky. *Sedimentary Geology*, *133*(1-2), 49-92. https://doi.org/10.1016/S0037-0738(00)00027-0

Dunbar, G. B., & Dickens, G. R. (2003). Late Quaternary shedding of shallow-marine carbonate along a tropical mixed siliciclastic–carbonate shelf: Great Barrier Reef, Australia. *Sedimentology*, *50*(6), 1061-1077. https://doi.org/10.1046/j.1365-3091.2003.00593.x

Dunlop, D. J. (2002). Theory and application of the Day plot (Mrs/Ms versus Hcr/Hc) 1. Theoretical curves and tests using titanomagnetite data. *Journal of Geophysical Research: Solid Earth*, *107*(B3), EPM-4. https://doi.org/10.1029/2001JB000486

Evans, M. E., & Heller, F. (2003). *Environmental magnetism: principles and applications of enviromagnetics*. Elsevier.

Felis, T., McGregor, H. V., Linsley, B. K., Tudhope, A. W., Gagan, M. K., Suzuki, A., ... & Webster, J. M. (2014). Intensification of the meridional temperature gradient in the Great Barrier Reef following the Last Glacial Maximum. *Nature Communications*, *5*(1), 1-8. https://doi.org/10.1038/ncomms5102

Francis, J. M., Dunbar, G. B., Dickens, G. R., Sutherland, I. A., & Droxler, A. W. (2007). Siliciclastic sediment across the North Queensland margin (Australia): a Holocene perspective on reciprocal versus coeval deposition in tropical mixed siliciclastic–carbonate systems. *Journal of sedimentary Research*, *77*(7), 572-586. https://doi.org/10.2110/jsr.2007.057

Frank, U., & Nowaczyk, N. R. (2008). Mineral magnetic properties of artificial samples systematically mixed from haematite and magnetite. *Geophysical Journal International*, *175*(2), 449-461. https://doi.org/10.1111/j.1365-246X.2008.03821.x

Frederichs, T., Bleil, U., Däumler, K., Dobeneck, T. V., & Schmidt, A. M. (1999). The magnetic view on the marine paleoenvironment: parameters, techniques and potentials of rock magnetic

studies as a key to paleoclimatic and paleoceanographic changes. In *Use of proxies in paleoceanography* (pp. 575-599). Springer, Berlin, Heidelberg.

Geiss, C. E., & Banerjee, S. K. (1997). A multi-parameter rock magnetic record of the last glacial-interglacial paleoclimate from south-central Illinois, USA. Earth and Planetary Science Letters, 152(1–4), 203–216. https://doi.org/10.1016/S0012-821X(97)00133-7

Glenn, C. R., Kroon, D., & Wei, W. 15. Sedimentary rhythms and climatic forcing of Pleistocene–Holocene mixed carbonates/siliciclastic sediments off the Great Barrier Reef. *In* McKenzie, J.A., Davies, P.J., Palmer-Julson, A., et al., *Proc. ODP, Sci. Results,* 133: College Station, TX (Ocean Drilling Program), 189–202. http://dx.doi.org/10.2973/odp.proc.sr.133.240.1993

Hallenberger, M., Reuning, L., Gallagher, S. J., Back, S., Ishiwa, T., Christensen, B. A., & Bogus, K. (2019). Increased fluvial runoff terminated inorganic aragonite precipitation on the Northwest Shelf of Australia during the early Holocene. *Scientific reports*, *9*(1), 1-9. https://doi.org/10.1038/s41598-019-54981-7

Hallock, P., & Schlager, W. (1986). Nutrient Excess and the Demise of Coral Reefs and Carbonate Platforms. *PALAIOS*, *1*(4), 389–398. https://doi.org/10.2307/3514476

Harper, B. B., Puga-Bernabéu, Á., Droxler, A. W., Webster, J. M., Gischler, E., Tiwari, M., Lado-Insua, T., Thomas, A. L., Morgan, S., Jovane, L., & Röhl, U. (2015). Mixed carbonate–siliciclastic sedimentation along the great barrier reef upper slope: a challenge to the reciprocal sedimentation model. *Journal of Sedimentary Research*, *85*(9), 1019-1036. https://doi.org/10.2110/jsr.2015.58.1

Harrison, R. J., & Feinberg, J. M. (2008). FORCinel: An improved algorithm for calculating first-order reversal curve distributions using locally weighted regression smoothing. *Geochemistry, Geophysics, Geosystems*, *9*(5). https://doi.org/10.1029/2008GC001987

Herrero-Bervera, E., & Jovane, L. (2013). On the palaeomagnetic and rock magnetic constraints regarding the age of IODP 325 Hole M0058A. *Geological Society, London, Special Publications*, *373*(1), 279-291. https://doi.org/10.1144/SP373.19

Hesse, P. P., Magee, J. W., & van der Kaars, S. (2004). Late Quaternary climates of the Australian arid zone: a review. *Quaternary International*, *118-119*, 87-102. https://doi.org/10.1016/S1040-6182(03)00132-0

Hillier, S., Roe, M. J., Geelhoed, J. S., Fraser, A. R., Farmer, J. G., & Paterson, E. (2003). Role of quantitative mineralogical analysis in the investigation of sites contaminated by chromite ore processing residue. *Science of the Total Environment*, *308*(1-3), 195-210. https://doi.org/10.1016/S0048-9697(02)00680-0

Hinestrosa, G., Webster, J. M., & Beaman, R. J. (2016). Postglacial sediment deposition along a mixed carbonate-siliciclastic margin: New constraints from the drowned shelf-edge reefs of the Great Barrier Reef, Australia. *Palaeogeography, Palaeoclimatology, Palaeoecology*, *446*, 168-185. https://doi.org/10.1016/j.palaeo.2016.01.023

Humblet, M., Potts, D. C., Webster, J. M., Braga, J. C., Iryu, Y., Yokoyama, Y., Bourillot, R., Séard, C., Droxler, A., Fujita, K., Gischler, E., & Kan, H. (2019). Late glacial to deglacial variation of coralgal assemblages in the Great Barrier Reef, Australia. *Global and Planetary Change*, *174*, 70-91. https://doi.org/10.1016/j.gloplacha.2018.12.014

Humphries, M. S., Benitez-Nelson, C. R., Bizimis, M., & Finch, J. M. (2017). An aeolian sediment reconstruction of regional wind intensity and links to larger scale climate variability since the last deglaciation from the east coast of southern Africa. *Global and Planetary Change*, *156*, 59–67. https://doi.org/10.1016/J.GLOPLACHA.2017.08.002

Imbrie, J. Z., Imbrie-Moore, A., & Lisiecki, L. E. (2011). A phase-space model for Pleistocene ice volume. *Earth and Planetary Science Letters*, *307*(1-2), 94-102. https://doi.org/10.1016/j.epsl.2011.04.018

Johnson, D. P., & Searle, D. E. (1984). Post-glacial seismic stratigraphy, central Great Barrier Reef, Australia. *Sedimentology*, *31*(3), 335-352. https://doi.org/10.1111/j.1365-3091.1984.tb00863.x

Johnson, D. P., Searle, D. E., & Hopley, D. (1982). Positive relief over buried post-glacial channels, Great Barrier Reef Province, Australia. *Marine Geology*, *46*(1-2), 149-159. https://doi.org/10.1016/0025-3227(82)90156-6

Jiang, Z., Liu, Q., Zhao, X., Jin, C., Liu, C., & Li, S. (2015). Thermal magnetic behaviour of Al-substituted haematite mixed with clay minerals and its geological significance. *Geophysical Journal International*, *200*(1), 130-143. https://doi.org/10.1093/gji/ggu377

Jouzel, J., Lorius, C., Petit, J. R., Genthon, C., Barkov, N. I., Kotlyakov, V. M., & Petrov, V. M. (1987). Vostok ice core: a continuous isotope temperature record over the last climatic cycle (160,000 years). *nature*, *329*(6138), 403-408. https://doi.org/10.1038/329403a0

Jovane, L., Florindo, F., Coccioni, R., Dinarès-Turell, J., Marsili, A., Monechi, S., ... & Sprovieri, M. (2007). The middle Eocene climatic optimum event in the Contessa Highway section, Umbrian Apennines, Italy. *Geological Society of America Bulletin*, *119*(3-4), 413-427. https://doi.org/10.1130/B25917.1

Jovane, L., Sprovieri, M., Florindo, F., Acton, G., Coccioni, R., Dall'Antonia, B., & Dinarès-Turell, J. (2007). Eocene-Oligocene paleoceanographic changes in the stratotype section, Massignano, Italy: Clues from rock magnetism and stable isotopes. *Journal of Geophysical Research: Solid Earth*, *112*(B11). https://doi.org/10.1029/2007JB004963

Jovane, L., Florindo, F., Bazylinski, D. A., & Lins, U. (2012). Prismatic magnetite magnetosomes from cultivated M agnetovibrio blakemorei strain MV-1: a magnetic fingerprint in marine sediments?. *Environmental Microbiology Reports*, *4*(6), 664-668. https://doi.org/10.1111/1758-2229.12000

Jovane, L., Hinnov, L., Housen, B. A., & Herrero-Barvera, E. (2013). Magnetic methods and the timing of geological processes. *Geological Society, London, Special Publications*, *373*(1), 1-12. https://doi.org/10.1144/SP373.17

Jovane, L., Florindo, F., Acton, G., Ohneiser, C., Sagnotti, L., Strada, E., ... & Passchier, S. (2019). Miocene glacial dynamics recorded by variations in magnetic properties in the

ANDRILL-2A drill core. *Journal of Geophysical Research: Solid Earth*, *124*(3), 2297-2312. https://doi.org/10.1029/2018JB016865

Just, J., Dekkers, M. J., von Dobeneck, T., Van Hoesel, A., & Bickert, T. (2012). Signatures and significance of aeolian, fluvial, bacterial and diagenetic magnetic mineral fractions in Late Quaternary marine sediments off Gambia, NW Africa. *Geochemistry, Geophysics, Geosystems*, *13*(9). https://doi.org/10.1029/2012GC004148

Karatsolis, B. T., De Vleeschouwer, D., Groeneveld, J., Christensen, B., & Henderiks, J. (2019, January). Deciphering climate forcing, basin evolution and biotic events on the NW Australian shelf: The Pliocene" Humid Interval" case study. In *Geophysical Research Abstracts* (Vol. 21).

Kershaw, A. P., van der Kaars, S., & Moss, P. T. (2003). Late Quaternary Milankovitch-scale climatic change and variability and its impact on monsoonal Australasia. *Marine Geology*, *201*(1-3), 81-95. https://doi.org/10.1016/S0025-3227(03)00210-X

Kees, C. (, & Kasse,). (2016). Sandy aeolian deposits and environments and their relation to climate during the Last Glacial Maximum and Lateglacial in northwest and central Europe., *26*(4), 507–532. https://doi.org/10.1191/0309133302PP350RA

King, J. W., & Channell, J. E. (1991). Sedimentary magnetism, environmental magnetism, and magnetostratigraphy. *Reviews of Geophysics*, *29*(S1), 358-370. https://doi.org/10.1002/ROG.1991.29.S1.358

Kostadinova-Avramova, M., & Kovacheva, M. (2013). The magnetic properties of baked clays and their implications for past geomagnetic field intensity determinations. *Geophysical Journal International*, *195*(3), 1534-1550. https://doi.org/10.1093/gji/ggt329

Lambert, F., Delmonte, B., Petit, J. R., Bigler, M., Kaufmann, P. R., Hutterli, M. A., Stocker, T. F., Ruth, U., Steffensen, J. P., & Maggi, V. (2008). Dust-climate couplings over the past 800,000 years from the EPICA Dome C ice core. *Nature*, *452*(7187), 616-619. https://doi.org/10.1038/nature06763

Larrasoana, J. C., Roberts, A. P., Chang, L., Schellenberg, S. A., Gerald, J. D. F., Norris, R. D., & Zachos, J. C. (2012). Magnetotactic bacterial response to Antarctic dust supply during the Palaeocene–Eocene thermal maximum. *Earth and Planetary Science Letters*, *333*, 122-133. https://doi.org/10.1016/j.epsl.2012.04.003

Larrasoaña, J. C., Roberts, A. P., Liu, Q., Lyons, R., Oldfield, F., Rohling, E. J., & Heslop, D. (2015). Source-to-sink magnetic properties of NE Saharan dust in Eastern Mediterranean marine sediments: review and paleoenvironmental implications. *Frontiers in Earth Science*, *3*, 19. https://doi.org/10.3389/feart.2015.00019

Leone, S., Palcu, D. V., Srivastava, P., Hassan, M. B., Muraszko, J. R., & Jovane, L. (2023). Changing sediment supply during glacial-interglacial intervals in the North Atlantic revealed by particle size characterization and environmental magnetism. *Global and Planetary Change*, *220*, 104022. https://doi.org/10.1016/j.gloplacha.2022.104022

Laskar, J., Fienga, A., Gastineau, M., & Manche, H. (2011). La2010: a new orbital solution for the long-term motion of the Earth. å 532. *A89*. https://doi.org/10.1051/0004-6361/201116836

Lewis, R. J., Tibby, J., Arnold, L. J., Gadd, P., Jacobsen, G., Barr, C., Negus, P. M., Mariani, M., Penny, D., Chittleborough, D., & Moss, E. (2021). Patterns of aeolian deposition in subtropical Australia through the last glacial and deglacial periods. *Quaternary Research*, *102*, 68–90. https://doi.org/10.1017/QUA.2020.117

Li, M., Ouyang, T., Roberts, A. P., Heslop, D., Zhu, Z., Zhao, X., Tian, C., Peng, S., Zhong, H., Peng, X., & Qiu, Y. (2018). Influence of Sea Level Change and Centennial East Asian Monsoon Variations on Northern South China Sea Sediments Over the Past 36 kyr. *Geochemistry, Geophysics, Geosystems*, *19*(5), 1674–1689. https://doi.org/10.1029/2017GC007321

Lisiecki, L. E. (2010). Links between eccentricity forcing and the 100,000-year glacial cycle. *Nature geoscience*, *3*(5), 349-352. https://doi.org/10.1038/ngeo828

Lisiecki, L. E., & Raymo, M. E. (2005). A Pliocene-Pleistocene stack of 57 globally distributed benthic δ18O records. *Paleoceanography*, *20*(1). https://doi.org/10.1029/2004PA001071

Liu, J. B., Chen, F. H., Chen, J. H., Xia, D. S., Xu, Q. H., Wang, Z. L., & Li, Y. C. (2011). Humid medieval warm period recorded by magnetic characteristics of sediments from Gonghai Lake, Shanxi, North China. *Chinese Science Bulletin 2011 56:23*, *56*(23), 2464–2474. https://doi.org/10.1007/S11434-011-4592-Y

Liu, Q., Roberts, A. P., Larrasoaña, J. C., Banerjee, S. K., Guyodo, Y., Tauxe, L., & Oldfield, F. (2012). Environmental magnetism: principles and applications. *Reviews of Geophysics*, *50*(4). https://doi.org/10.1029/2012RG000393

Magee, J. W., Miller, G. H., Spooner, N. A., & Questiaux, D. (2004). Continuous 150 ky monsoon record from Lake Eyre, Australia: insolation-forcing implications and unexpected Holocene failure. *Geology*, *32*(10), 885-888. https://doi.org/10.1130/G20672.1

Maher, B. A. (2011). The magnetic properties of Quaternary aeolian dusts and sediments, and their palaeoclimatic significance. *Aeolian Research*, *3*(2), 87–144. https://doi.org/10.1016/J.AEOLIA.2011.01.005

Maher, B. A., & Thompson, R. (1992). Paleoclimatic Significance of the Mineral Magnetic Record of the Chinese Loess and Paleosols. *Quaternary Research*, *37*(2), 155–170. https://doi.org/10.1016/0033-5894(92)90079-X

Maxwell, W. H., & Swinchatt, J. P. (1970). Great Barrier Reef: regional variation in a terrigenous-carbonate province. *Geological Society of America Bulletin*, *81*(3), 691-724. https://doi.org/10.1130/0016-7606(1970)81[691:GBRRVI]2.0.CO;2

McNeill, D. F. (1993a). A review and comparison of carbonate rock magnetization: Leg 133, Queensland Plateau, Australia. In *Proc. Ocean Drilling Program, Scientific Results* (Vol. 133, pp. 749-753). https://doi.org/10.2973/odp.proc.sr.133.284.1993

McNeill, D. F., Guyomard, T. S., & Hawthorne, T. B. (1993b). Magnetostratigraphy and the nature of magnetic remanence in platform/periplatform carbonates, Queensland Plateau, Australia. In *Proc. Ocean Drilling Program, Scientific Results* (Vol. 133, pp. 573-587). https://doi.org/10.2973/odp.proc.sr.133.263.1993

McWhorter, J. K., Halloran, P. R., Roff, G., Skirving, W. J., Perry, C. T., & Mumby, P. J. (2022). The importance of 1.5° C warming for the Great Barrier Reef. *Global Change Biology*, *28*(4), 1332-1341. https://doi.org/10.1111/gcb.15994

Miller, C., Hahn, A., Liebrand, D., Zabel, M., & Schefuß, E. (2020). Mid-and low latitude effects on eastern South African rainfall over the Holocene. *Quaternary Science Reviews*, *229*, 106088. https://doi.org/10.1016/j.quascirev.2019.106088

Molodkov, A., Bitinas, A., Molodkov, B., & Bitinas, A. &. (2006). Sedimentary record and luminescence chronology of the Lateglacial and Holocene aeolian sediments in Lithuania. *Boreas*, *35*(2), 244–254. https://doi.org/10.1111/J.1502-3885.2006.TB01154.X

Mongin, M., Baird, M. E., Tilbrook, B., Matear, R. J., Lenton, A., Herzfeld, M., Wild-Allen, K., Skerratt, J., Margvelashvili, N., Robson, B. J., Duarte, C. M., Gustafsson, M. S. M., Ralph, P. J., & Steven, A. D. L. (2016). The exposure of the Great Barrier Reef to ocean acidification. *Nature communications*, *7*(1), 1-8. https://doi.org/10.1038/ncomms10732

Moore, D. M., & Reynolds Jr, R. C. (1989). *X-ray Diffraction and the Identification and Analysis of Clay Minerals*. Oxford University Press (OUP).

Moreno, E., Thouveny, N., Delanghe, D., McCave, I. N., & Shackleton, N. J. (2002). Climatic and oceanographic changes in the Northeast Atlantic reflected by magnetic properties of sediments deposited on the Portuguese Margin during the last 340 ka. *Earth and Planetary Science Letters*, *202*(2), 465-480. https://doi.org/10.1016/S0012-821X(02)00787-2

Moss, P. T., Kershaw, A. P., & Grindrod, J. (2005). Pollen transport and deposition in riverine and marine environments within the humid tropics of northeastern Australia. *Review of Palaeobotany and Palynology*, *134*(1-2), 55-69. https://doi.org/10.1016/j.revpalbo.2004.11.003

Nanson, G. C., East, T. J., & Roberts, R. G. (1993). Quaternary stratigraphy, geochronology and evolution of the Magela Creek catchment in the monsoon tropics of northern Australia. *Sedimentary Geology*, *83*(3-4), 277-302. https://doi.org/10.1016/0037-0738(93)90017-Y

Nanson, G. C., Price, D. M., & Short, S. A. (1992). Wetting and drying of Australia over the past 300 ka. *Geology*, *20*(9), 791-794. https://doi.org/10.1130/0091-7613(1992)020<0791:WADOAO>2.3.CO;2

Neil, D. T., Orpin, A. R., Ridd, P. V., & Yu, B. (2002). Sediment yield and impacts from river catchments to the Great Barrier Reef lagoon: a review. *Marine and Freshwater Research*, *53*(4), 733-752. https://doi.org/10.1071/MF00151

Oldfield, F., Asioli, A., Accorsi, C. A., Mercuri, A. M., Juggins, S., Langone, L., Rolph, T., Trincardi, F., Wolff, G., Gibbs, Z., Vigliotti, L., Frignani, M., Van Der Post, K., & Branch, N. (2003). A high resolution late Holocene palaeo environmental record from the central Adriatic Sea. *Quaternary Science Reviews*, *22*(2-4), 319-342. https://doi.org/10.1016/S0277-3791(02)00088-4

Page, M. C., & Dickens, G. R. (2005). Sediment fluxes to Marion Plateau (southern Great Barrier Reef province) over the last 130 ky: new constraints on 'transgressive-shedding'off northeastern Australia. *Marine Geology*, *219*(1), 27-45. https://doi.org/10.1016/j.margeo.2005.05.002

Page, M. C., Dickens, G. R., & Dunbar, G. B. (2003). Tropical view of Quaternary sequence stratigraphy: siliciclastic accumulation on slopes east of the Great Barrier Reef since the Last Glacial Maximum. *Geology*, *31*(11), 1013-1016. https://doi.org/10.1130/G19622.1

Paterson, G. A., Zhao, X., Jackson, M., & Heslop, D. (2018). Measuring, processing, and analyzing hysteresis data. *Geochemistry, Geophysics, Geosystems*, *19*(7), 1925-1945. https://doi.org/10.1029/2018GC007620

Pedrão, G. A., Costa, K. B., Toledo, F. A., Tomazella, M. O., & Jovane, L. (2021). Semi-Quantitative Analysis of Major Elements and Minerals: Clues from a Late Pleistocene Core from Campos Basin. *Applied Sciences*, *11*(13), 6206. https://doi.org/10.3390/app11136206

Pei, R., Kuhnt, W., Holbourn, A., Hingst, J., Koppe, M., Schultz, J., Kopetz, P., Zhang, P., & Andersen, N. (2021). Monitoring Australian Monsoon variability over the past four glacial

cycles. *Palaeogeography, Palaeoclimatology, Palaeoecology*, *568*, 110280. https://doi.org/10.1016/j.palaeo.2021.110280

Pendleton, L., Hoegh-Guldberg, O., Albright, R., Kaup, A., Marshall, P., Marshall, N., Fletcher, S., Haraldsson, G., & Hansson, L. (2019). The Great Barrier Reef: Vulnerabilities and solutions in the face of ocean acidification. *Regional Studies in Marine Science*, *31*, 100729. https://doi.org/10.1016/j.rsma.2019.100729

Peng, X., Ao, H., Xiao, G., Qiang, X., & Sun, Q. (2020). The early-middle Pleistocene transition of Asian summer monsoon. *Palaeogeography, Palaeoclimatology, Palaeoecology*, *545*, 109636. https://doi.org/10.1016/j.palaeo.2020.109636

Petrick, B., Martínez-García, A., Auer, G., Reuning, L., Auderset, A., Deik, H., Takayanagi, H., De Vleeschouwer, D., Iryu, Y., & Haug, G. H. (2019). Glacial indonesian throughflow weakening across the mid-pleistocene climatic transition. *Scientific reports*, *9*(1), 1-13. https://doi.org/10.1038/s41598-019-53382-0

Piva, A., Asioli, A., Schneider, R. R., Trincardi, F., Andersen, N., Colmenero-Hidalgo, E., Dennielou, B., Flores, J. A., & Vigliotti, L. (2008). Climatic cycles as expressed in sediments of the PROMESS1 borehole PRAD1-2, central Adriatic, for the last 370 ky: 1. Integrated stratigraphy. *Geochemistry, Geophysics, Geosystems*, *9*(1). https://doi.org/10.1029/2007GC001713

Prajith, A., Tyagi, A., & John Kurian, P. (2018). Changing sediment sources in the Bay of Bengal: Evidence of summer monsoon intensification and ice-melt over Himalaya during the Late Quaternary. *Palaeogeography, Palaeoclimatology, Palaeoecology*, *511*, 309–318. https://doi.org/10.1016/J.PALAEO.2018.08.016

Puga-Bernabéu, Á., Webster, J. M., Beaman, R. J., & Guilbaud, V. (2011). Morphology and controls on the evolution of a mixed carbonate–siliciclastic submarine canyon system, Great Barrier Reef margin, north-eastern Australia. *Marine Geology*, *289*(1–4), 100–116. https://doi.org/10.1016/J.MARGEO.2011.09.013

Puga-Bernabéu, Á., Webster, J. M., & Beaman, R. J. (2013a). Potential collapse of the upper slope and tsunami generation on the Great Barrier Reef margin, north-eastern Australia. *Natural Hazards*, *66*(2), 557–575. https://doi.org/10.1007/S11069-012-0502-0/FIGURES/7

Puga-Bernabéu, Á., Webster, J. M., Beaman, R. J., & Guilbaud, V. (2013b). Variation in canyon morphology on the Great Barrier Reef margin, north-eastern Australia: The influence of slope and barrier reefs. *Geomorphology*, *191*, 35-50. https://doi.org/10.1016/j.geomorph.2013.03.001

Puga-Bernabéu, Á., Webster, J. M., Beaman, R. J., Reimer, P. J., & Renema, W. (2014). Filling the gap: A 60 ky record of mixed carbonate-siliciclastic turbidite deposition from the Great Barrier Reef. *Marine and Petroleum Geology*, *50*, 40–50. https://doi.org/10.1016/J.MARPETGEO.2013.11.009

Puga-Bernabéu, Á., Beaman, R. J., Webster, J. M., Thomas, A. L., & Jacobsen, G. (2017). Gloria Knolls Slide: A prominent submarine landslide complex on the Great Barrier Reef margin of north-eastern Australia. *Marine Geology*, *385*, 68-83. https://doi.org/10.1016/j.margeo.2016.12.008

Puga-Bernabéu, Á., López-Cabrera, J., Webster, J.M., Beaman, R.J. (2022). Submarine landslide morphometrics and slope failure dynamics along a mixed carbonate-siliciclastic margin, north-eastern Australia. Geomorphology, 403, 108179. https://doi.org/10.1016/j.geomorph.2022.108179

Qiang, X. K., Li, Z. X., Powell, C. M., & Zheng, H. B. (2001). Magnetostratigraphic record of the Late Miocene onset of the East Asian monsoon, and Pliocene uplift of northern Tibet. *Earth and Planetary Science Letters*, *187*(1-2), 83-93. https://doi.org/10.1016/S0012-821X(01)00281-3

Roberts, A. P., Almeida, T. P., Church, N. S., Harrison, R. J., Heslop, D., Li, Y., Li, J., Muxworthy, A. R., Williams, W., & Zhao, X. (2017). Resolving the origin of pseudo-single domain magnetic behavior. *Journal of Geophysical Research: Solid Earth*, *122*(12), 9534-9558. https://doi.org/10.1002/2017JB014860

Roberts, A. P., Florindo, F., Chang, L., Heslop, D., Jovane, L., & Larrasoaña, J. C. (2013). Magnetic properties of pelagic marine carbonates. *Earth-science reviews*, *127*, 111-139. https://doi.org/10.1016/j.earscirev.2013.09.009

Roberts, A. P., Florindo, F., Villa, G., Chang, L., Jovane, L., Bohaty, S. M., Larrasoaña, J. C., Heslop, D., & Fitz Gerald, J. D. (2011). Magnetotactic bacterial abundance in pelagic marine environments is limited by organic carbon flux and availability of dissolved iron. *Earth and Planetary Science Letters*, *310*(3-4), 441-452. https://doi.org/10.1016/j.epsl.2011.08.011

Roberts, A. P., Heslop, D., Zhao, X., & Pike, C. R. (2014). Understanding fine magnetic particle systems through use of first-order reversal curve diagrams. *Reviews of Geophysics*, *52*(4), 557-602. https://doi.org/10.1002/2014RG000462

Roberts, A. P., Pike, C. R., & Verosub, K. L. (2000). First-order reversal curve diagrams: A new tool for characterizing the magnetic properties of natural samples. *Journal of Geophysical Research: Solid Earth*, *105*(B12), 28461-28475. https://doi.org/10.1029/2000JB900326

Rohling, E. J., Grant, K., Bolshaw, M., Roberts, A. P., Siddall, M., Hemleben, C., & Kucera, M. (2009). Antarctic temperature and global sea level closely coupled over the past five glacial cycles. *Nature Geoscience*, *2*(7), 500-504. https://doi.org/10.1038/ngeo557

Rothwell, R. G. (2015). Twenty years of XRF core scanning marine sediments: What do geochemical proxies tell us?. In *Micro-XRF studies of sediment cores* (pp. 25-102). Springer, Dordrecht. https://doi.org/10.1007/978-94-017-9849-5_1

Rutherford, S., & D'Hondt, S. (2000). Early onset and tropical forcing of 100,000-year Pleistocene glacial cycles. *Nature*, *408*(6808), 72-75. https://doi.org/10.1038/35040533

Savian, J. F., Jovane, L., Frontalini, F., Trindade, R. I. F., Coccioni, R., Bohaty, S. M., Wilson, P. A., Florindo, F., Roberts, A. P., Catanzariti, R., & Iacoviello, F. (2014). Enhanced primary productivity and magnetotactic bacterial production in response to middle Eocene warming in the Neo-Tethys Ocean. *Palaeogeography, Palaeoclimatology, Palaeoecology*, *414*, 32-45. https://doi.org/10.1016/j.palaeo.2014.08.009

Savian, J. F., Jovane, L., Giorgioni, M., Iacoviello, F., Rodelli, D., Roberts, A. P., Chang, L., Florindo, F., & Sprovieri, M. (2016). Environmental magnetic implications of magnetofossil occurrence during the Middle Eocene Climatic Optimum (MECO) in pelagic sediments from the equatorial Indian Ocean. *Palaeogeography, Palaeoclimatology, Palaeoecology*, *441*, 212-222. https://doi.org/10.1016/j.palaeo.2015.06.029

Schmidt, A. M. (2001). Monitoring Termination II by environmental magnetic records from subtropical South Atlantic sediments. *Paleoceanography*, *16*(6), 644–657. https://doi.org/10.1029/2000PA000531

Shackleton, N. J. (2000). The 100,000-year ice-age cycle identified and found to lag temperature, carbon dioxide, and orbital eccentricity. *Science*, *289*(5486), 1897-1902. https://doi.org/10.1126/science.289.5486.1897

Spratt, R. M., & Lisiecki, L. E. (2015). A Late Pleistocene sea level stack. *Climate of the Past Discussions*, *11*(4), 3699-3728. https://doi.org/10.5194/cp-12-1079-2016, 2016

Stoeckl, N., Hicks, C. C., Mills, M., Fabricius, K., Esparon, M., Kroon, F., Kaur, K., & Costanza, R. (2011). The economic value of ecosystem services in the Great Barrier Reef: our state of knowledge. *Annals of the New York Academy of Sciences*, *1219*(1), 113-133. https://doi.org/10.1111/j.1749-6632.2010.05892.x

Stoner, J. S., Channell, J. E., & Hillaire-Marcel, C. (1995). Magnetic properties of deep-sea sediments off southwest Greenland: Evidence for major differences between the last two deglaciations. *Geology*, *23*(3), 241-244. https://doi.org/10.1130/00917613(1995)023<0241:MPODSS>2.3.CO;2

Stoner, J. S., Channell, J. E. T., & Hillaire-Marcel, C. (1995). Late Pleistocene relative geomagnetic paleointensity from the deep Labrador Sea: Regional and global correlations. *Earth and Planetary Science Letters*, *134*(3-4), 237-252. https://doi.org/10.1016/0012-821X(95)00134-X

Thomas, M. F., Nott, J., Murray, A. S., & Price, D. M. (2007). Fluvial response to late Quaternary climate change in NE Queensland, Australia. *Palaeogeography, Palaeoclimatology, Palaeoecology*, *251*(1), 119-136. https://doi.org/10.1016/j.palaeo.2007.02.021

Thompson, R., & Oldfield, F. (1986). Magnetic properties of natural materials. *Environmental Magnetism*, 21–38. https://doi.org/10.1007/978-94-011-8036-8_4

Thompson, R., Bloemendal, J., Dearing, J. A., Oldfield, F., Rummery, T. A., Stober, J. C., & Turner, G. M. (1980). Environmental applications of magnetic measurements. *Science (New York, N.Y.)*, *207*(4430), 481–486. https://doi.org/10.1126/SCIENCE.207.4430.481

Tripathi, S., Tiwari, M., Lee, J., & Khim, B. K. (2017). First evidence of denitrification vis-à-vis monsoon in the Arabian Sea since Late Miocene. *Scientific reports*, *7*(1), 1-7. https://doi.org/10.1038/srep43056

Verosub, K. L., & Roberts, A. P. (1995). Environmental magnetism: Past, present, and future. *Journal of Geophysical Research: Solid Earth*, *100*(B2), 2175-2192. https://doi.org/10.1029/94JB02713

Waelbroeck, C., Labeyrie, L., Michel, E., Duplessy, J. C., McManus, J. F., Lambeck, K., Balbon, E., & Labracherie, M. (2002). Sea-level and deep water temperature changes derived from benthic foraminifera isotopic records. *Quaternary science reviews*, *21*(1-3), 295-305. https://doi.org/10.1016/S0277-3791(01)00101-9

Warrier, A. K., Mahesh, B. S., Mohan, R., Shankar, R., Asthana, R., & Ravindra, R. (2014). Glacial–interglacial climatic variations at the Schirmacher Oasis, East Antarctica: The first report from environmental magnetism. *Palaeogeography, Palaeoclimatology, Palaeoecology*, *412*, 249–260. https://doi.org/10.1016/J.PALAEO.2014.08.007

Webster, J. M., Beaman, R. J., Puga-Bernabéu, Á., Ludman, D., Renema, W., Wust, R. A. J., George, N. P. J., Reimer, P. J., Jacobsen, G. E., & Moss, P. (2012). Late Pleistocene history of turbidite sedimentation in a submarine canyon off the northern Great Barrier Reef, Australia. *Palaeogeography, Palaeoclimatology, Palaeoecology*, *331*, 75-89. https://doi.org/10.1016/j.palaeo.2012.02.034

Webster, J.M., Yokoyama, Y., Cotterill, C., and the Expedition 325 Scientists (2011). Proc. IODP, 325: Tokyo (Integrated Ocean Drilling Program Management International, Inc.). https://doi.org/10.2204/iodp.proc.325.2011

Webster, J. M., Braga, J. C., Humblet, M., Potts, D. C., Iryu, Y., Yokoyama, Y., ... & Lougheed, B. C. (2018). Response of the Great Barrier Reef to sea-level and environmental changes over the past 30,000 years. *Nature Geoscience*, *11*(6), 426-432. https://doi.org/ 10.1038/s41561-018-0127-3

Wei, G., McCulloch, M. T., Mortimer, G., Deng, W., & Xie, L. (2009). Evidence for ocean acidification in the Great Barrier Reef of Australia. *Geochimica et Cosmochimica Acta*, *73*(8), 2332-2346. https://doi.org/10.1016/j.gca.2009.02.009

Wolanski, E., & De'ath, G. (2005). Predicting the impact of present and future human land-use on the Great Barrier Reef. *Estuarine, Coastal and Shelf Science*, *64*(2-3), 504-508. https://doi.org/10.1016/j.ecss.2005.03.017

Wyrwoll, K. H., & Miller, G. H. (2001). Initiation of the Australian summer monsoon 14,000 years ago. *Quaternary International*, *83*, 119-128. https://doi.org/10.1016/S1040-6182(01)00034-9

Yang, X. Q., Grapes, R., Zhou, H. Y., & Yang, J. (2008). Magnetic properties of sediments from the Pearl River Delta, South China: Paleoenvironmental implications. *Science in China Series D: Earth Sciences 2008 51:1, 51*(1), 56–66. https://doi.org/10.1007/S11430-007-0151-4

Yin, Q., & Berger, A. (2015). Interglacial analogues of the Holocene and its natural near future. *Quaternary Science Reviews, 120*, 28-46. https://doi.org/10.1016/j.quascirev.2015.04.008

Yokoyama, Y., Esat, T. M., Thompson, W. G., Thomas, A. L., Webster, J. M., Miyairi, Y., Sawada, C., Aze, T., Matsuzaki, H., Okuno, J., Fallon, S., Braga, J. C., Humblet, M., Iryu, Y., Potts, D. C., Fujita, K., Suzuki, A., & Kan, H. (2018). Rapid glaciation and a two-step sea level

plunge into the Last Glacial Maximum. *Nature*, *559*(7715), 603-607. https://doi.org/10.1038/s41586-018-0335-4

Yokoyam, Y., Webster, J. M., Cotterill, C., Braga, J. C., Jovane, L., Mills, H., Morgan, S., & Suzuki, A. (2011). IODP Expedition 325: Great Barrier Reefs reveals past sea-level, climate and environmental changes since the last ice age. *Scientific Drilling*, *12*, 32-45. https://doi.org/10.2204/iodp.sd.12.04.2011

Zhao, X., Roberts, A. P., Heslop, D., Paterson, G. A., Li, Y., & Li, J. (2017). Magnetic domain state diagnosis using hysteresis reversal curves. *Journal of Geophysical Research: Solid Earth*, *122*(7), 4767-4789. https://doi.org/10.1002/2016JB013683

Zheng, Y., Kissel, C., Zheng, H. B., Laj, C., & Wang, K. (2010). Sedimentation on the inner shelf of the East China Sea: Magnetic properties, diagenesis and paleoclimate implications. *Marine Geology*, *268*(1–4), 34–42. https://doi.org/10.1016/J.MARGEO.2009.10.009

Supplementary material

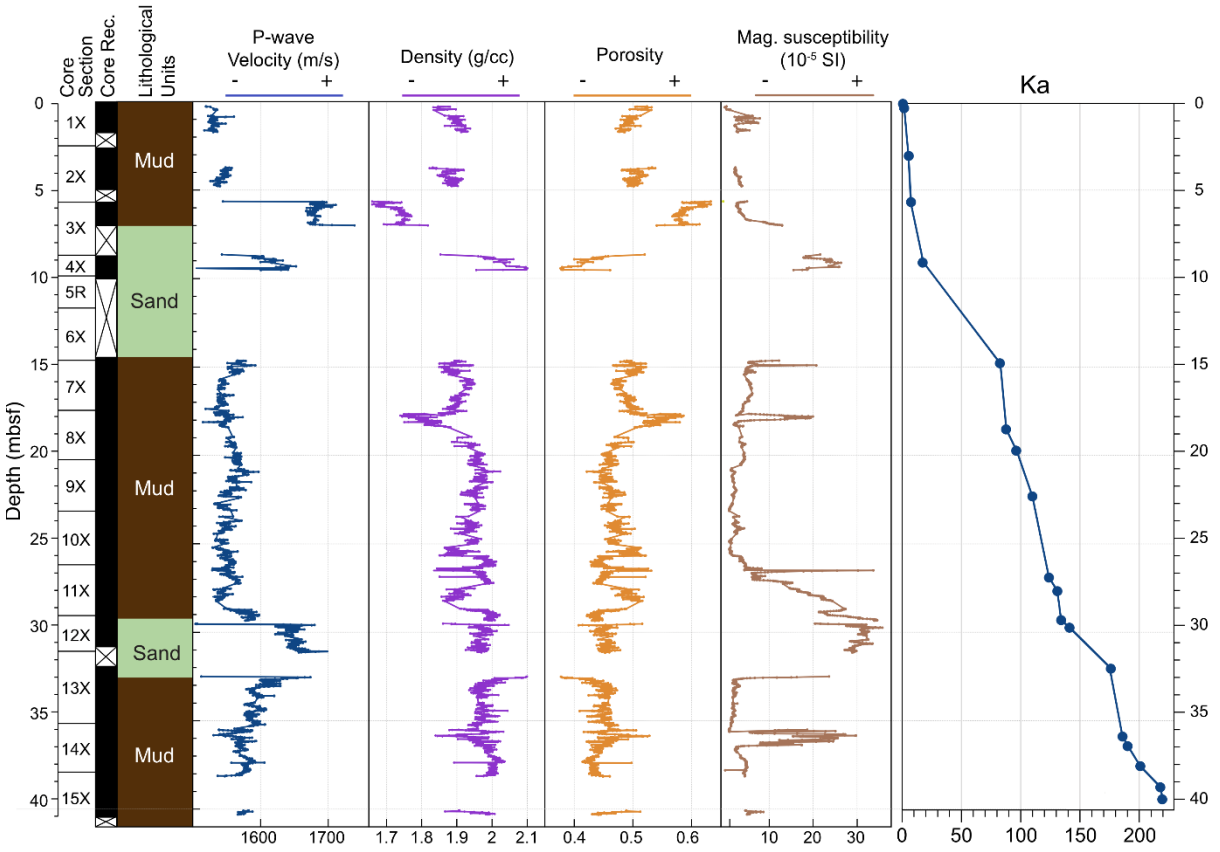

Figure S1. Summary of Hole M0058A Holocene and Upper Pleistocene record (Webster et al., 2011; IODP post-cruise data report). Lithology is dominated by unconsolidated mud and two sand/grainstone packages. Drilling recovery of the sand facies was incomplete due to its unconsolidated nature, with two intervals of the record missing, at 33-32 m and 15-10 m. The muddy sediments are characterized by low P-wave velocities, porosity and magnetic susceptibility values, while the sand/grainstone sediments show higher p-wave velocities and magnetic susceptibility results. The composite age model (at the extreme right) used was established by Harper et al. (2015).

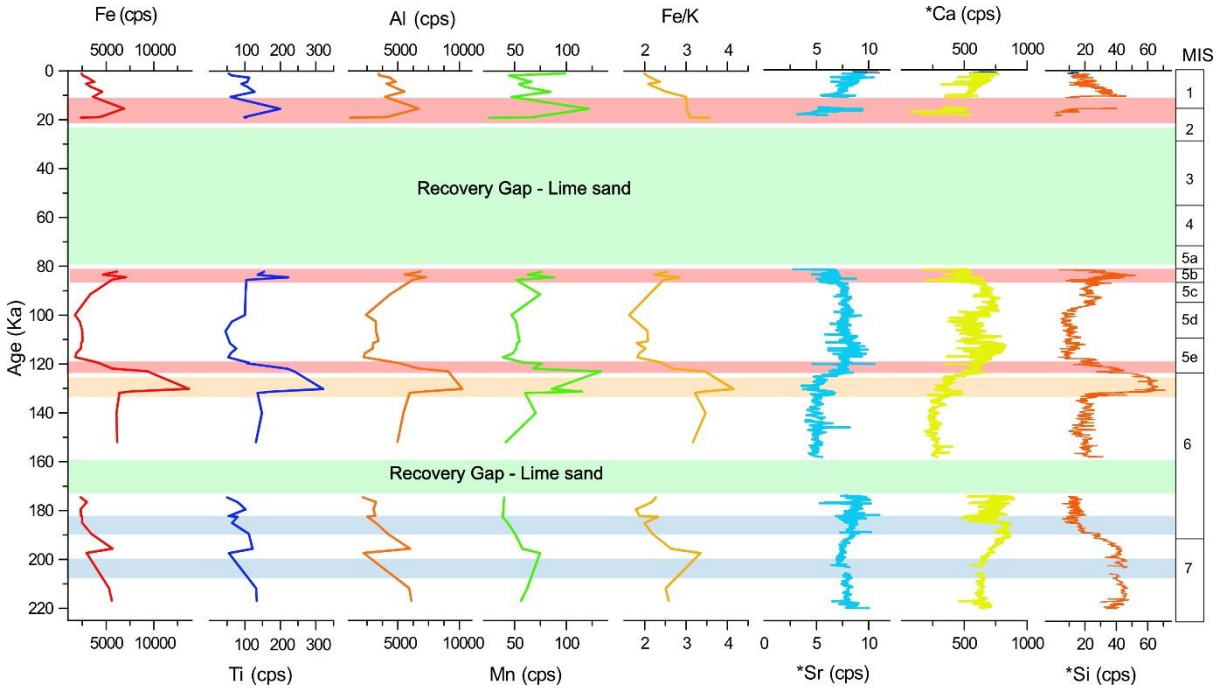

Fig. S2. X-Ray Fluorescence (XRF) elemental concentration along the core sections of Hole M0058A. Left to right; Fe, Ti, Al, Mn and Fe/K ratio (From this study) compared to the high-resolution results for Sr, Ca and Si from Harper et al. (2015) marked by *. As shown in the main text in Figures 5 and 6, blue bars show a mixture of terrigenous and marine sediments; yellow bar shows Iron Manganese and Silica enrichment, rising temperatures and sea-level representing the terrigenous input; red bars compared with the magnetic data represent dust input resulting in the presence of biogenic magnetite and high primary productivity.

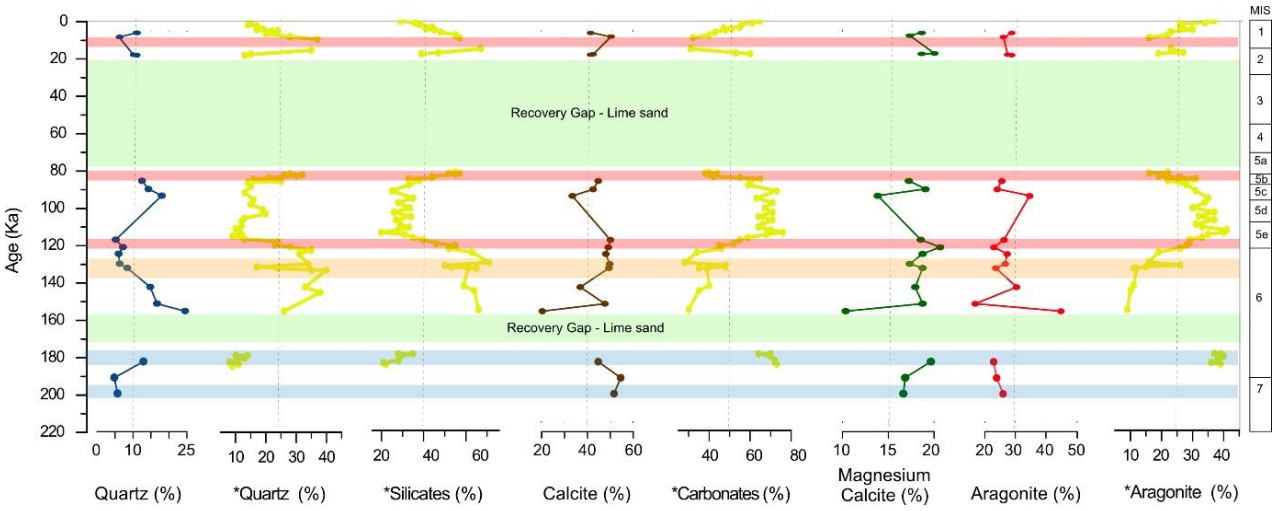

Fig. S3. X-Ray Diffraction (XRD) mineralogy results from Hole M0058A. The section displays Quartz (blue curve), Calcite (brown curve), Magnesium Calcite (green curve), and Aragonite (red curve) from this study compared to high-resolution results for Quartz, Silicates, Carbonates and Aragonite from Harper et al (2015) (marked by * and represented by yellow curves). Down core mineralogical changes marked by red, yellow, green, and blue bars are consistent with the geochemical changes shown in Fig. 6 and Fig. S2 suggesting a mixed siliciclastic carbonate sedimentation in response to glacio-eustatic changes.

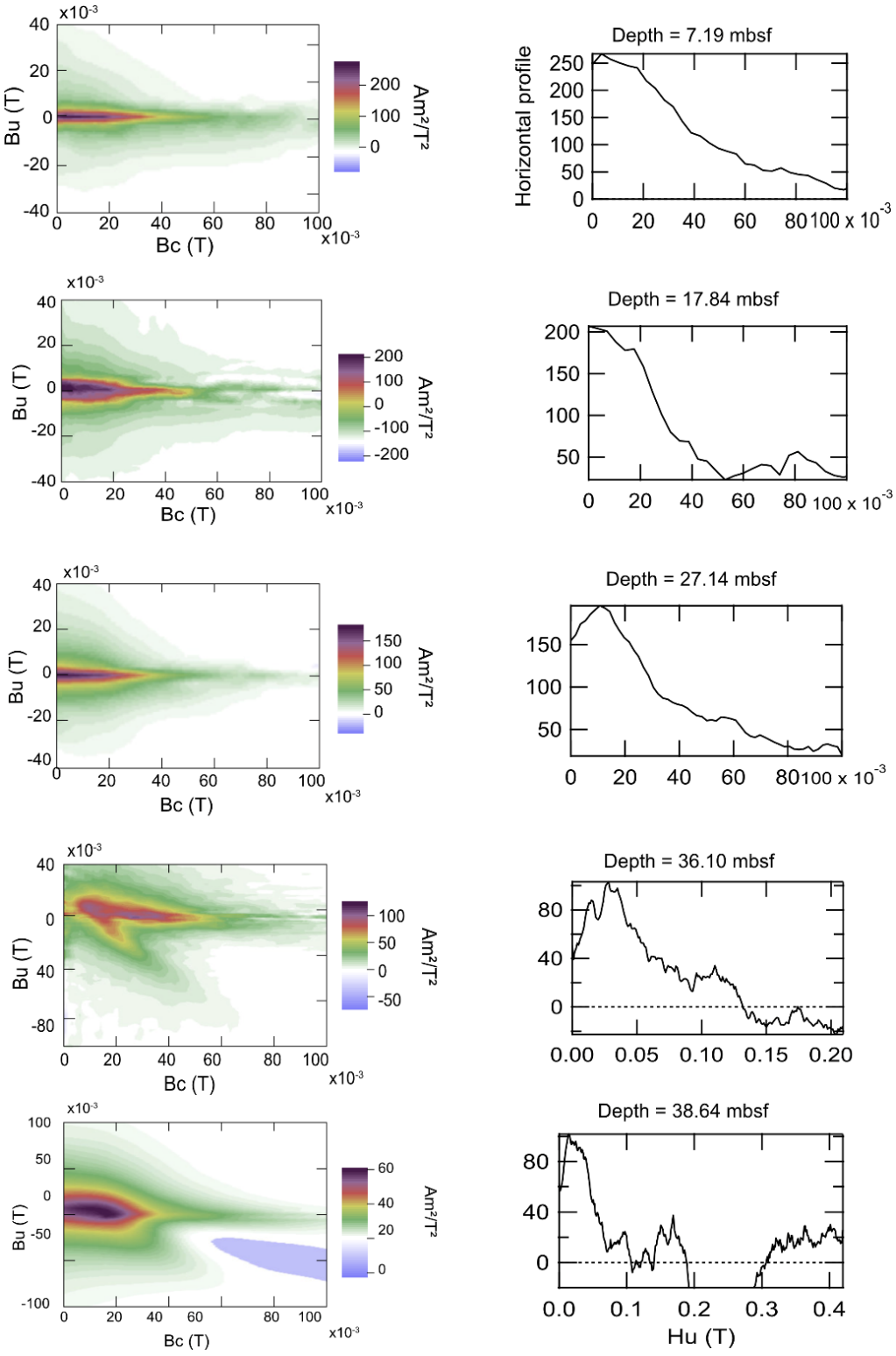

Fig. S4. First Order Reversal Curves (FORCs) and corresponding horizontal profiles at five different depths along the Hole M0058A section. The samples located on the lower parts of the section (38.64 m and 36.10 m) present distinct magnetic characteristics in comparison to the upper section samples (27.14 m, 17.84 m and 7.19 m). The lower part (38.64 m and 36.10 m) is characterized by the mixture of high and low coercivity magnetic components (Pseudosingle domain to multi domain) whereas the upper part of the section (27.14 m, 17.84 m and 7.19 m) is characterized by a single magnetic domain, low coercivity components.

6 THESIS CONCLUSION

This study showed the presence of magnetofossils in a FeMn nodule sample from CCZ. The increased magnetic properties in the diagenetic Mn-rich layers correspond to favourable conditions for magnetite biomineralization in the OSTZ. Magnetofossils have the potential to be used in future paleomagnetic, paleooxygenation, and paleoenvironmental studies of the deep ocean system.

FeMn crusts from RGR and TS typically grow hydrogenetically under oxic conditions, preventing crystallization of primary remanent magnetization and potentially causing oxidation of already existing magnetic minerals. These characteristics of the studied crust samples make them ineffective for magnetostratigraphic dating. Non-phosphatized layers contain paramagnetic/superparamagnetic amorphous, poorly crystalline Fe oxyhydroxides that are unreliable carriers of primary remanent magnetization. Primary geochemical, mineralogical, and magnetic signals have been altered by different phosphatization stages that occurred under suboxic conditions throughout the history of FeMn crusts, thus variations in magnetic data do not correspond to primary magnetization. The presence of magnetic minerals as primary remanent magnetization carriers elsewhere in the Pacific Ocean and China Sea are related to the local environmental conditions for magnetic mineral preservation, whereas the absence of the Fe (II) phase in FeMn crusts is common in FeMn crusts from different regions of the world oceans.

FeMn nodules and crusts from the Pacific Ocean contain biogenic magnetite produced by magnetotactic bacteria as a primary remanence carrier. The efficiency of magnetic methods in relation to the concentration of magnetic particles was investigated. Magnetic methods used for the detection of magnetofossils or biogenic magnetite depend on the concentration of magnetic particles rather than magnetite producing MTB strains, the cultured *Magnetovibrio blakemorei* strain MV-1^{T} and *Magnetofaba australis* strain IT-1. IT-1 cells containing larger-sized, elongated octahedral magnetic crystals have higher amounts of carbon content than MV-1 cells containing hexoctahedral crystals. This study presented pioneering work about carbon-cycling processes by MTB which are potentially related to the ancient and modern sedimentary systems. The deposition of Fe and Mn, and the presence of biogenic magnetite in shallow marine environments revealed a different paleoenvironmental scenario. Geochemical and magnetic study of the Late Quaternary sediments from Hole M0058A (IODP Expedition 325) provided an opportunity to reveal the environmental processes that shaped the Great Barrier Reef during the Pleistocene and Holocene. Between MIS 7 and MIS 6, an increase in the mixture of magnetic minerals and neritic carbonate sediments was identified, which is the result of

shoreline progradation and retrogradation. At the end of MIS 6, a gradual increase in magnetic properties concomitant with an increase in terrigenous input represented by Fe and Mn commenced the influence of the Australian monsoon in the region. After the glacial-interglacial transition of MIS 6-5e (ca. 122 ka) and at the peak warm phases of ca. 85 ka and ca. 7 ka, high coercivity magnetic components (i.e., hematite) and consequent low coercivity SD biogenic magnetite exhibited a change in the provenance of the terrigenous fraction, with the presence of finer hematite likely associated with increased deposition of aeolian sediments. Dust fertilization increased primary productivity in the area, resulting in the appearance of magnetotactic bacteria in the sea floor sediments. This indicates a diminished influence of the Australian Monsoon over the GBR during the peak warm phases of the late Pleistocene and Holocene.

Hence, the deposition of Fe and Mn in different marine environments has distinct magnetic implications. The presence of biogenic magnetite in FeMn nodules and crusts is linked to the oxygenation conditions in the marine environment while the biogenic magnetite in the studied mixed siliciclastic carbonate sediments from the GBR region in northeastern Australia is the consequence of the primary productivity enhanced by arid climatic conditions.